

**T Cells in the Spotlight: A Multi-Omics Examination of
Erosional & Ruptured Acute Coronary Syndromes**

Inaugural Dissertation

zur

Erlangung des Doktorgrades

Dr. nat. med.

der Medizinischen Fakultät

und

der Mathematisch-Naturwissenschaftlichen Fakultät

der Universität zu Köln

vorgelegt von

Lauren Madison De Vore

aus Portland Oregon, USA

Copy – Star Printing and Advertising GmbH

2026

**T Cells in the Spotlight: A Multi-Omics Examination of
Erosional & Ruptured Acute Coronary Syndromes**

Inaugural Dissertation

zur

Erlangung des Doktorgrades

Dr. nat. med.

der Medizinischen Fakultät

und

der Mathematisch-Naturwissenschaftlichen Fakultät

der Universität zu Köln

vorgelegt von

Lauren Madison De Vore

aus Portland Oregon, USA

Copy – Star Printing and Advertising GmbH

2026

Betreuer/in Prof. Dr. Holger Winkels

Referent/in Prof. Dr. Achim Tresch
Prof. Dr. Andreas Beyer

Datum der mündlichen Prüfung: 19.12.2023

ACKNOWLEDGEMENTS

Many large thanks to Dr. Monika Schlosser and Prof. Dr. Rosenkranz for creating a community of interdisciplinary medical scientists here in Cologne. Without the support of this community, there is a large chance this thesis would not have survived such hurdles as the COVID-19 pandemic. I would like to thank Prof. Dr. Holger Winkels for being my PI for this thesis. I would also like to thank Dr. med Teresa Gerhardt for her mentorship and our collaboration together.

I would like to thank my mentors Prof. Dr. Achim Tresch, Prof. Dr. Andreas Beyer, and Prof. Dr. med Esther Lutgens for their continued support and constructive feedback throughout the time of my studies.

I would also like to thank all the members of our lab for our discussions during my study as well as my the TRR 259 for funding and support. A special thanks to Dr. Felix Picard, PhD candidate Tim Dorweiler, and PhD candidate Khrystyna Totska for making this time together especially special. Thanks to Prof. Dr. David Leistner and all members of the OPTICO-ACS trial for allowing me to work together on the team and for the kind welcoming during my time in Berlin. I would like to also thank Dr. Joachim Linssen who mentored me on the importance of higher academic studies and who gave me industry skills that were instrumental in curating my thesis. I would also like to find thanks to my American background, especially Prof. Dr. Megan Bestwick and Prof. Dr. Brian Gilbert. Their culture in scientific rigor and investigation deeply aided my scientific discovery and held my research on a straight path while so far away from home.

Finally, I would like to thank my mother and father, Diana, and Jon. While my passion for investigation yields from my father, my interest in science and utter determination stems from my mother. This thesis become so much more personal in the prospect of nearly losing my mother to a medical emergency related to my area of research.

Therefore, I am thankful that her determination in everything in life continues in me through the completion of my dissertation. I would like to give the writing of my dissertation in honor of everything she has given to me, such that I might give a small fraction of that back to her.

ABSTRACT

Acute coronary syndromes (ACS) are a significant cause of global mortality ¹. ACS is characterized by the sudden interruption of blood flow to the heart muscle. Plaque rupture and plaque erosion are two mechanisms involved in ACS, leading to thrombus formation and myocardial ischemia. The global burden of ACS carries significant implications for public health, quality of life, and socioeconomic costs. In 2017, ACS accounted for an estimated 9.5 million global deaths, comprising 16% of all yearly fatalities ¹³. The total economic burden of ACS is \$150 billion in the United States annually, with a direct medical cost estimated at \$75 billion ¹⁴. Yet, an epidemiological transition for low- and middle-income countries as they continue to grow economically and undergo lifestyle changes warrants concern, especially for populations not typically associated with coronary artery disease, such as younger adults and women.

While the main mechanisms of plaque rupture are understood, the underlying mechanisms of both plaque erosion and ruptured plaque remain unclear. This study aims to investigate the molecular mechanisms of erosional and ruptured plaque using a unique multi-omic approach of cellular indexing of transcriptomes and epitopes combined with single-cell T-cell receptor sequencing. This investigation unearthed a notable enrichment of T_{H17} cells in erosional ACS when compared to rupture and chronic coronary syndrome. This discovery, coupled with the observed enrichment of ruptured CD4⁺ T_{TE} cells relative to erosion, hints at the multifaceted roles that T-cells play in both rupture and erosion mechanisms. Further findings on the upregulation of Integrin α 6 and gene ontology results of cell adhesion dynamics for T_{H17} cell's function depict a critical role of T_{H17} on laminin-rich structures such as blood vessels.

Furthermore, via the integration of t-cell receptor repertoire information and the investigation of erosional and ruptured plaque public clonotypes, a narrative of common antigen exposure in erosional plaque depicted itself.

ZUSAMMENFASSUNG

Akute Koronarsyndrome (ACS) sind eine bedeutende Ursache für die weltweite Sterblichkeit, die durch eine plötzliche Unterbrechung des Blutflusses zum Herzmuskel gekennzeichnet ist. Plaqueruptur und Plaquerosion sind zwei Mechanismen, die bei ACS eine Rolle spielen und zur Thrombusbildung und Myokardischämie führen. Die globale Belastung durch ACS hat erhebliche Auswirkungen auf die öffentliche Gesundheit, die Lebensqualität und die sozioökonomischen Kosten. Im Jahr 2017 waren ACS für schätzungsweise 9,5 Millionen Todesfälle weltweit verantwortlich, was 16 % aller jährlichen Todesfälle ausmacht¹³. Die wirtschaftliche Gesamtbelastung durch ACS beläuft sich in den Vereinigten Staaten auf jährlich 150 Milliarden US-Dollar, wobei die direkten medizinischen Kosten auf 75 Milliarden US-Dollar geschätzt werden¹⁴. Die epidemiologische Entwicklung in Ländern mit niedrigem und mittlerem Einkommen, die wirtschaftlich weiter wachsen und ihren Lebensstil ändern, ist jedoch besorgniserregend, insbesondere für Bevölkerungsgruppen, die normalerweise nicht mit koronarer Herzkrankheit in Verbindung gebracht werden, wie z. B. jüngere Erwachsene und Frauen.

Während die wichtigsten Mechanismen der Plaqueruptur bekannt sind, bleiben die zugrundeliegenden Mechanismen sowohl der Plaquerosion als auch der rupturierten Plaque unklar. In dieser Studie sollen die molekularen Mechanismen erosiver und rupturierter Plaque mit Hilfe eines einzigartigen Multi-Omik-Ansatzes untersucht werden, der die zelluläre Indexierung von Transkriptomen und Epitopen mit der Sequenzierung von Einzelzell-T-Zell-Rezeptoren kombiniert. Bei dieser Untersuchung wurde eine bemerkenswerte Anreicherung von T_{H17}-Zellen bei erosivem ACS im Vergleich zu Rupturen und chronischem Koronarsyndrom festgestellt. Diese Entdeckung und die beobachtete Anreicherung von CD4⁺ T_{TE}-Zellen bei rupturierter ACS im Vergleich zu erosivem ACS weisen auf die vielfältigen Rollen hin, die T-Zellen sowohl bei Ruptur- als auch bei Erosionsmechanismen spielen. Weitere Erkenntnisse über die Hochregulierung von Integrin $\alpha 6$ und Gen-Ontologie-Ergebnisse der Zelladhäsionsdynamik für die Funktion von T_{H17}-Zellen zeigen eine kritische Rolle von T_{H17} auf Laminin-reichen Strukturen wie Blutgefäßen.

Durch die Integration von Informationen über das T-Zell-Rezeptor-Repertoire und die Untersuchung der öffentlichen Klonotypen von erosionsbedingten und rupturierten Plaques konnte eine gemeinsame Antigenexposition in erosionsbedingten Plaques aufgezeigt werden.

Table of Contents

Acknowledgements.....	4
Abstract.....	5
List of Figures	9
List of Tables	11
List of Abbreviations	12
Introduction.....	14
Chapter 1: Acute Coronary Syndromes	14
1.1 Diagnostic Measures & Classification	14
1.2 Epidemiology & Risk Factors.....	16
1.3 Pathophysiology.....	18
1.4 Clinical Presentation	19
1.5 Diagnostic Evaluation.....	20
1.6 Management & Treatment.....	20
Chapter 2: The Role of Immune Cells in ACS	21
2.1 A Shifted Perspective on Atherosclerosis	21
2.2 T-Cell Maturation & Activation	21
2.3 T-Cell Differentiation.....	23
2.4 T-Cell Receptors	25
2.5 T-Cell Mechanisms: Rupture vs. Erosion.....	26
2.6 Beyond T-Cells: The Multifaceted Immune Involvement	27
Chapter 3: Next Generation Sequencing	28
3.1 Single-Cell RNA Sequencing with Droplet Microfluidics	28
3.2 Multiplexing & Demultiplexing Samples.....	29
3.3 Data transformation Files: FASTA to FASTQ	30
3.4 Uniform Manifold Approximation & Projection	30
3.5 CITE-seq: Cellular Indexing of Transcriptomes & Epitopes.....	31
3.6 Isotypes & Isotype Controls	32
3.7 TCR Sequencing Technologies	33
3.8 Weighted Nearest Neighbor Analysis	33
3.9 Cell Annotation Via Anchoring	33
Aims & Objectives	35
Chapter 4. Investigation Aim	35
4.1 Recent Findings: Unravelling Discrepancies between Erosional and Ruptured ACS	35
4.2 Investigation Aim & Objectives	35
Materials & Methods	37
Chapter 5. OPTICO-ACS Study: Patient Selection	37
5.1 The OPTICO-ACS Study.....	37
5.2 Patient Cohort Considerations for Multi-omics.....	37
Chapter 6. Patient Sample Processing to Sequencing.....	39
6.1 Whole Blood Processing	39
6.2 Isolation & Storage.....	39
6.3 Cell Surface Staining & Cell Hashing	40
6.4 Library Preparation & Sequencing.....	45
Chapter 7. Bioinformatic Methodology	46
7.1 Cell Ranger Multi.....	46

7.2 Gaussian-Mixture-Model-based Demultiplexing.....	46
7.3 Denoised & Scaled Antibody Expressions.....	48
7.4 Creation of a Multimodal Seurat File.....	49
7.5 Merging Seurat Objects, Pre-Processing, and Weight nearest neighbor analysis	51
7.6 The App for Reference-Based Single-Cell Analysis: Azimuth.....	51
7.7 Re-clustering T-cell Specific Subset & Annotations	52
Results	54
Chapter 8. Constructing an Integrated Multimodal Atlas	54
8.1 Patient Characteristics	54
8.2 Wet Lab Organizational Output	55
8.3 Demultiplexing Results	56
8.4 DSB Normalized Antibody Panel.....	57
8.5 Creating a WNN UMAP	59
8.6 Constructing an Integrated Multimodal Atlas	59
Chapter 9. T-Cell Sub-Clustering Analysis	66
9.1 T-Cell Sub-clustering: Nearest Neighbor Groupings	66
9.2 T-Cell Sub-Clustering Frequencies	67
9.3 UMAP Separation by Patient Subsets & Individual Patients	68
9.4 Group-wise Differential Expression Analysis	69
9.5 Functional Enrichment Analysis of Erosional TH17 Cells.....	72
Chapter 10. Looking Closer at the TCR Repertoire of ACS Patients	73
10.1 A Trimodal UMAP: Erosion vs. Rupture	73
10.2 Rarefaction Diversity Analysis.....	78
10.3 Public Clonotype Analysis	78
10.4 Clustering Based on Repertoire Overlap	81
Discussion	85
Chapter 11. Discussing Mechanisms of Plaque Rupture & Plaque Erosion.....	85
11.1 T-cell Enrichment	85
11.2 Cell Adhesion in Erosional Plaque.....	87
11.3 TCR Signal Amplification	88
11.3 Shared Global Clones and Diversity	89
11.3 Therapeutic & Genetic Testing Implications.....	89
Summary	90
Limitations.....	90
Outlooks.....	91
References	92
Curriculum Vitae	100
Declarations	102

List of Figures

Figure 1: Comparison of ECG Segments & Intervals to STEMI & NSTEMI Outcomes.....	16
Figure 2: Plaque Erosion vs. Plaque Rupture Using OCT	17
Figure 3: A Shift to Higher Noninfectious Disease Prevalence in the United States	18
Figure 4: Lesion Types of Atherosclerosis & Theorized Sequence of Development	19
Figure 5: Atherosclerotic Plaque Development: Rupture vs. Erosion	20
Figure 6: ACS Diagnostic Decision Tree Using OCT	21
Figure 7: T-Cell Maturation & Notch Signaling	23
Figure 8: T-Cell Activation via MHC & Co-Stimulatory Pathways	24
Figure 9: Main T-Cell Differentiation	25
Figure 10: TCR Gene Rearrangement	26
Figure 11: Comparison of Immune Cell Interactions: Rupture vs. Erosion	28
Figure 12: GEM Formation via 10x Protocol.....	30
Figure 13: Example of an Oligonucleotide-Tagged Antibody by Biolegend	30
Figure 14: Multiplexing & Demultiplexing Process Overview	31
Figure 15: Simplices: The Core Building Blocks to Topological Spaces.....	32
Figure 16: Cellular Indexing of Transcriptomes & Epitopes	33
Figure 17: Cell Annotation via Reference-Query Anchoring.....	35
Figure 18: Results from OPTICO-ACS Study in 2020	36
Figure 19: Patient Recruitment from the OPTICO-ACS Study	38
Figure 20: Experimental Setup from Aspiration to Library Creation	41
Figure 21: Cell Viability Gating Strategy for Sorting on BD FACS Aria	42
Figure 22: Methodological Outline from Sequencing to a Demultiplexed Multi-Modal UMAP	46
Figure 23: Experimental Design for Cell Ranger Multi Analysis by Pooled Patients	47
Figure 24: Quality Control Demultiplexing Histogram Example.....	48
Figure 25: Technical Limitations for Multiple Oligonucleotide-Tagged Libraries.....	49
Figure 26: GMM-Demux Manual Patient Demultiplexing from Pool	49
Figure 27: Final Isotype Control Distributions After Quality Control	50
Figure 28: Multimodal Integration of RNA and Protein Expression Data by Patient	51
Figure 29: Clonotype Binning as Recommended by ScRepertoire	52
Figure 30: Quality Control of Gene Expression Distributions.....	52
Figure 31: DSB Normalization Effects of TotalSeq-C Antibody Body Panel on Integrated Object	59
Figure 32: Constructing Weighted Nearest Neighbor UMAP	60
Figure 33: Constructing an Integrated Multimodal Object with Anchored Annotations.....	61
Figure 34: Patient Separated UMAPs of Integrated Multimodal Atlas	62
Figure 35: Mean Frequency of Immune Cell Types: Erosion vs. Rupture.....	63
Figure 36: DE Genes of Atlas Against Immune Cell Subtypes.....	64
Figure 37: DE TotalSeq-C Antibodies of Atlas Against Immune Cell Subtypes	65
Figure 38: DE Antibodies Based on Patient Subtype & Subsequent Analyses	67
Figure 39: WNN T-Cell Sub-clustering.....	68
Figure 40: Mean Frequency of T-cell Subsets in Each Patient Subtype.....	69
Figure 41: Separation of UMAP by Patient Subtype.....	69
Figure 42: T-Cell Numbers Derived from Each Patient.....	70
Figure 43: Separation of UMAP by Individual Patients.....	70
Figure 44: T-Cell DE Group-Wise Analysis from RNA Expression Against Immune Cell Subtypes	71
Figure 45: T-Cell DE Analysis from TotalSeq-C Antibody Panel Against Immune Cell Subtypes	72

Figure 46: Erosional T _{H17} GO Enrichment	73
Figure 47: T-Cell Subset Locations at Different Clonotype Expansion Levels.....	74
Figure 48: Binning Quantities of Clonal Expansion Among Patient Subtyping.....	75
Figure 49: T _{H17} Clonotype Size: Rupture vs Erosion	76
Figure 50: T-Cell Clonotype by Expansion Level: Rupture vs. Erosion.....	77
Figure 51: T-Cell DE Analysis from RNA Expression with Clonal Expansion Information	78
Figure 52: Rarefaction Analysis.....	79
Figure 53: Overlapping Public Clonotypes via Mosaic.....	80
Figure 54: Overlapping Public Clonotypes via Hierarchical Heatmap	81
Figure 55: Natural Clustering TCR Repertoires Using TSNE.....	82
Figure 56: Hierarchical Clustering of Patients Based on TCR Repertoire Affinities.....	83
Figure 57: ZAP-70 Phosphorylation	88

List of Tables

Table 1: Study Inclusion/Exclusion Criteria.....	38
Table 2: Custom Whitelist for Demultiplexing via TotalSeq Hashtags	41
Table 3: Whitelist for TotalSeq-C Human Universal Cocktail	42
Table 4: PBMC Reference Dataset Annotation Details for Celltype.l2	52
Table 5: Individual Patient Characteristics	54
Table 6: Baseline Characteristics	54
Table 7: Sampling Pooling, Cell Viability Measurements, and RNA Sequencing Yield	56
Table 8: Manual Demultiplexing Singlets Sorted Per Patient.....	57
Table 9: CDR3 Sequences of Global Clonotypes Shared by More than Two Patients.....	84

List of Abbreviations

ACS	Acute Coronary Syndromes
CHD	Coronary Heart Disease
MI	Myocardial Infarction
ECG	Electrocardiography
STEMI	ST-Segment Elevation Myocardial Infarction
NSTEMI	Non-ST-Segment Elevation Myocardial Infarction
PCI	Percutaneous Coronary Intervention
CAD	Coronary Artery Disease
OCT	Optical Coherence Tomograph
NETs	Neutrophil extracellular traps
QoL	Quality of Life
AHA	American Heart Association
LMICs	Low- and middle-income countries
JACC	Journal of American College of Cardiology
EROSION	Effective Anti-Thrombotic Therapy Without Stenting: Intravascular Optical Coherence Tomography-Based Management in Plaque Erosion
MACE	Major adverse cardiovascular events
WBCs	White blood cells
ETPs	Early Thymic Progenitor cells
DN cells	Double negative cells
TCR	T cell receptor
VDJ	Variable-Diversity-Junctional
MHC	Major Histocompatibility Complexes
APCs	Antigen-presenting cells
DCs	Dendritic cells
T _H	Helper T cell
T _{FH}	T follicular helper cell
Treg	Regulatory T cell
CTLs	Cytotoxic T lymphocytes
IL	Interleukin
TNF- α	Tumor Necrosis Factor Alpha
CD	Cluster of Differentiation
SMCs	Smooth muscle cells
T _{EM}	Effector Memory T cells
T _{CM}	Central Memory T cells
iNKT	Invariant Natural Killer T cell
MAIT	Mucosal-associated Invariant T cell
MR1	Myofibrillogenesis Regulator 1
$\gamma\delta$ T	Gamma Delta T cells
ICIs	Immune Checkpoint Inhibitors
T _{TE}	Terminal Effector T cells
TCRs	T Cell Receptors
IFN- γ	Interferon-gamma
MMPs	Metalloproteinases
PMN	Polymorphonuclear Neutrophils

ROS	Reactive Oxygen Species
GEMs	Gel Bead-In-Emulsions
Poly(A) tail	Polyadenylic acid tail
TSO	Template Switch Oligo
Poly(dT) tail	Poly-deoxythymidine tail
scRNA-seq	Single-cell RNA Sequencing
RNA	Ribonucleic Acid
DNA	Deoxyribonucleic Acid
FASTA	FAST-ALL
FASTQ	FAST-QUALITY
UMAP	Uniform Manifold Approximation and Projection
KNN	K-Nearest Neighbor
CITE	Cellular Indexing of Transcriptomes and Epitopes
ADT	Antibody Derived Tags
PCR	Polymerase Chain Reaction
scTCRsequencing	Single-cell TCR sequencing
WNN	Weighted Nearest Neighbor
CCA	Conical Correlation Analysis
OPTICO-ACS	OPTical-Coherence Tomography in Acute Coronary Syndrome
FU	Follow-up
BVS	Biovascular Scaffold
TIMI	Thrombolysis in Myocardial Infarction Score
CK	Creatine Kinase
DMSO	Dimethylsulfoxide
EDTA	Ethylenediamine tetraacetic acid
PBMCs	Peripheral Blood Mononuclear Cells
PBS	Phosphate buffered saline
Fc Receptor Block	Fragment Crystallizable Receptor Block
7-AAD	7-Aminoactinomycin D
BSA	Bovine serum albumin
CCG	Cologne Center for Genomics
GEX	Gene Expression technology
VDJ_T	T cell V(D)J
BCL Files	Binary Base Call Files
GMM-Demux	Gaussian-Mixture-Model-Based
VLOOKUP	Vertical Lookup
RT	Reverse Transcription
HTO	Hashtag oligo
DSB	Denoised and Scaled by Background
CLR	Centered log ratio transformation
MT	Mitochondrial
SLM	Smart Local Moving
HuBMAP	Human BioMolecular Atlas Program
SCE	SingleCellExperiment
DE	Differentially Expressed
Log2FC	Binary Logarithm Fold Change
NK	Natural Killer Cells

HLA-DR	Human Leukocyte Antigen-DR
PTPRC	Protein Tyrosine Phosphatase Receptor Type C
ECM	Extracellular Matrix
GO	Gene Ontology
TSNE	T-Distributed Stochastic Neighbor Embedding
PTPRC	Protein Tyrosine Phosphate Receptor Type C

INTRODUCTION

Chapter 1. Acute Coronary Syndromes

1.1 Diagnostic Measures & Classification

Acute coronary syndromes (ACS) remain the most devastating clinical manifestation of cardiovascular disease, whereby cardiovascular diseases remain the most common cause of global mortality¹. ACS is a manifestation of coronary heart disease (CHD) and is often caused by a disruption of plaque within the coronary arteries, otherwise known as atherosclerosis². ACS refers to a sudden and acute, interruption of blood flow to the heart muscle, as opposed to one that is chronic and stable. ACS typically arises due to buildup of fatty deposits or plaques along the walls of coronary arteries². This interruption to the coronary arteries in delivering oxygen and nutrients to heart muscles, often clinically termed *angina*, can result in the death of heart muscles.

These cells' death results in muscle tissue damage and is termed a heart attack or myocardial infarction (MI). In contrast, Chronic Coronary Syndrome (CCS) is a term used to describe a cluster of cardiovascular conditions characterized by long-term or persistent issues affecting the coronary arteries—the blood vessels responsible for supplying blood to the heart muscle. Another synonymous term is "Chronic Ischemic Heart Disease," which reflects the chronic and stable aspects of reduced blood flow to the heart muscle due to coronary artery disease. CCS primarily concerns chronic and predictable symptoms in contrast to ACS, which involves sudden and potentially life-threatening events like unstable angina and myocardial infarctions².

The first historical description of *angina pectoris* meaning "chest tightness", was accounted for by English physician Dr. William Heberden in 1768³. However, it was not until the use of electrocardiography (ECG) in the early 1900s that significant progress in understanding and treating ACS was made. The ECG allowed ACS to be identified based on the electrical charge interval between ventricular depolarization and repolarization. In a normal ECG, the ST-segment is flat, as seen in **Figure 1**⁴. ST-segment elevation myocardial infarction (STEMI) and non-ST-segment elevation myocardial infarction (NSTEMI) are two subcategorizations of ACS that differentiate based on an abnormal elevation or depression of the ST segment as well as if the level of cardiac troponin in the blood is high enough to conclude heart muscle damage⁵.

A STEMI is defined as a complete blockage or occlusion of a coronary artery whereby at least two contiguous leads of an ECG present an ST-segment elevation⁴. This elevation above baseline for the ST segment indicates a loss of blood flow to the heart muscle in the affected area. Conversely, an NSTEMI is characterized by a partial occlusion, which causes a smaller area of the heart muscle to become damaged or die. An NSTEMI may present itself on an ECG with ST-segment depression, T-wave inversion, or no significant changes at all. Therefore, diagnosing an NSTEMI is more challenging compared to a STEMI. One more caveat to the difficulty of successful diagnosis of infarction is the indication of heart damage. Although the troponin test mentioned previously is fantastic for detecting muscle damage, the test itself is not specific to the heart alone, as cutoff values for NSTEMI and STEMI differ⁶. Therefore, potential confounding to other conditions, such as kidney disease, can result in raised troponin levels and yet no occlusion.

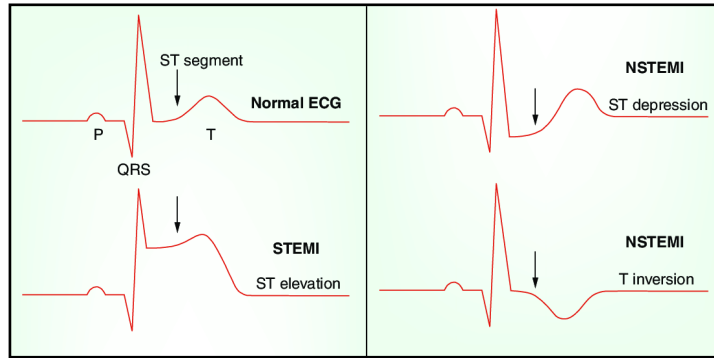


Figure 1: Comparison of ECG Segments & Intervals to STEMI & NSTEMI Outcomes ⁷

Thrombolytic therapy began in the 1950s, whereby pharmaceuticals were implemented to dissolve blood clots and therefore introduced as a treatment for STEMI ⁸. This was followed by the percutaneous coronary intervention (PCI) that was developed in the 1970s, whereby a catheter is used to open blocked or narrowed coronary arteries ⁹.

In 1996, Farb et al. observed, while studying coronary artery disease (CAD), that a significant proportion of patients with ACS had a distinct morphology not represented by the traditional models known at the time ¹⁰. This subset of ACS patients exhibited a unique type of plaque characterized by a thin fibrous cap and a large lipid core. In this new subset, termed plaque erosion, the endothelial lining was irregular and lost, leading to platelet aggregation and thrombus formation, and coronary artery obstruction. This groundbreaking work revealed that this mechanism accounted for up to a third of all cases of ACS, particularly in younger patients, women, and those without traditional risk factors for CAD ¹⁰.

Optical coherence tomography (OCT), a high-resolution imaging technique providing an "optical biopsy" of the plaque, is essential for distinguishing between plaque rupture and plaque erosion ¹¹. Using OCT images as seen in **Figure 2**, it is possible to differentiate between plaque rupture and plaque erosion in vivo based on several key parameters:

1. Fibrous cap thickness & integrity: The intactness of the fibrous cap, while also appearing thicker, is a hallmark sign of plaque erosion in contrast to plaque rupture, where the fibrous cap is usually thin and ruptured ¹¹.
2. Surface features: The plaque surface is typically smooth and intact in plaque erosion, while in plaque rupture, the surface is often irregular, with jagged edges and ulcerations ¹¹.
3. Thrombus features: The thrombus or blood clot is the aggregation of fibrin, red blood cells, platelets, leukocytes, and neutrophil extracellular traps (NETs). In plaque rupture, the thrombus often has a well-defined border and is large and adherent. In contrast, the thrombus of plaque erosion is often smaller and less adherent with more irregular borders. Interestingly, the difference in aggregation types between the two subsets is an area of much focus ¹².

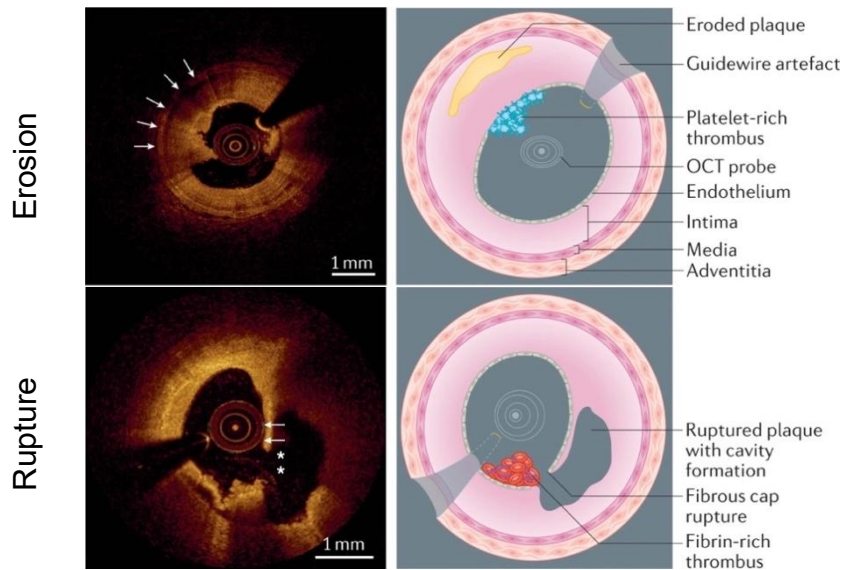


Figure 2: Plaque Erosion vs. Plaque Rupture Using OCT ¹²

1.2 Epidemiology & Risk Factors

The global burden of ACS carries significant implications for public health, patient quality of life (QoL), and socioeconomic costs. In 2017, ACS accounted for an estimated 9.5 million global deaths, comprising 16% of all yearly fatalities ¹³. The American Heart Association (AHA) estimates that the total economic burden of ACS is \$150 billion in the United States annually with a direct medical cost estimated at \$75 billion ¹⁴.

While the burden of ACS is pronounced worldwide, the incidence varies significantly among regions and countries. Low- and middle-income countries (LMICs) shoulder a higher ACS burden, with elevated incidence and mortality rates ¹⁵. LMICs prevalence of ACS is rising and accounts for approximately 80% of the total burden and 85% of the total disability from ACS worldwide ¹⁶. This burden imposes substantial stress on healthcare systems, as indicated by the economic impact of ACS-related costs ¹⁵.

In high-income countries, there is a greater prevalence of traditional risk factors like smoking, dyslipidemia, and hypertension ¹⁴. Access to advanced diagnostics, therapies, and robust healthcare systems contributes to the high overall ACS burden in these countries by the rate of reporting ^{17,18}. Conversely, low- and middle-income countries exhibit a distinct ACS burden. This could stem from a unique risk factor profile involving metabolic risks, inflammation, and infectious diseases. Limited healthcare access, lower awareness of cardiovascular health, and inadequate infrastructure might lead to underdiagnosis and undertreatment of ACS cases, intensifying the QoL burden for undetected cases ^{19,20}. Given the substantial ACS burden in these regions, predicting epidemiological transitions due to economic growth and lifestyle changes, as shown in **Figure 3**, is essential to anticipate and address the evolving needs ¹⁹.

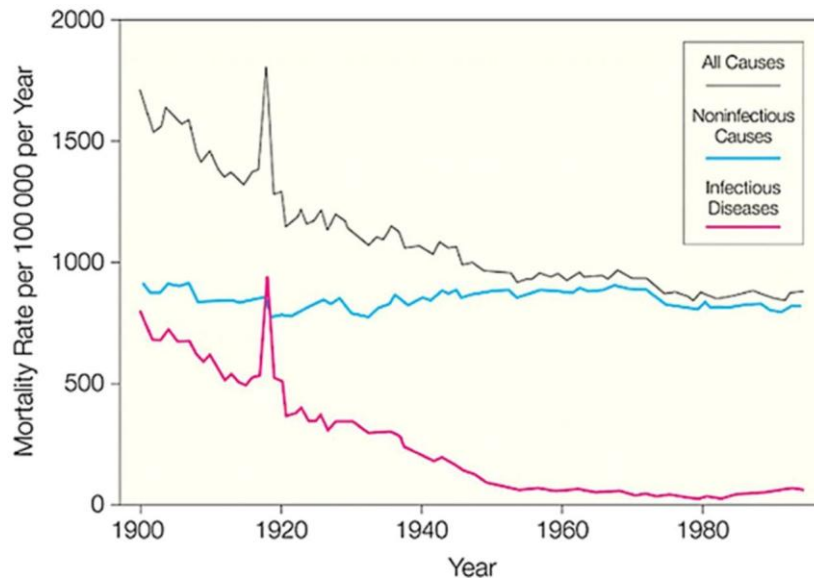


Figure 3: A Shift to Higher Noninfectious Disease Prevalence in the United States ¹⁹

The risk factor profiles associated with rupture and erosion subtypes may vary between high-income and low- and middle-income countries; however, more research in this area is required. While traditional risk factors play a role in both settings, non-traditional factors like infectious diseases and socioeconomic disparities could exert a more significant influence in low- and middle-income countries. Recognizing these distinctions is pivotal for crafting tailored preventive strategies and optimizing resource allocation.

Moreover, studies indicate that women might exhibit a higher prevalence of erosional ACS than men ²¹. Despite the typical association of ACS with older men, it remains a substantial cause of morbidity and mortality in women and younger adults. Notably, women with ACS often fare worse than their male counterparts, with delayed diagnosis and suboptimal treatment partly due to underutilization of interventions like PCI and recommended medications ^{21,22}. Addressing these gender disparities is essential to improve symptom recognition, ensure timely diagnosis, and enhance access to evidence-based care, thereby alleviating the burden of ACS.

1.3 Pathophysiology

The progression of atherosclerosis from its initial stages to the development of ACS offers a complex insight into its pathophysiology. **Figure 4** presents the traditional lesion types of atherosclerosis along with their proposed sequence of development.

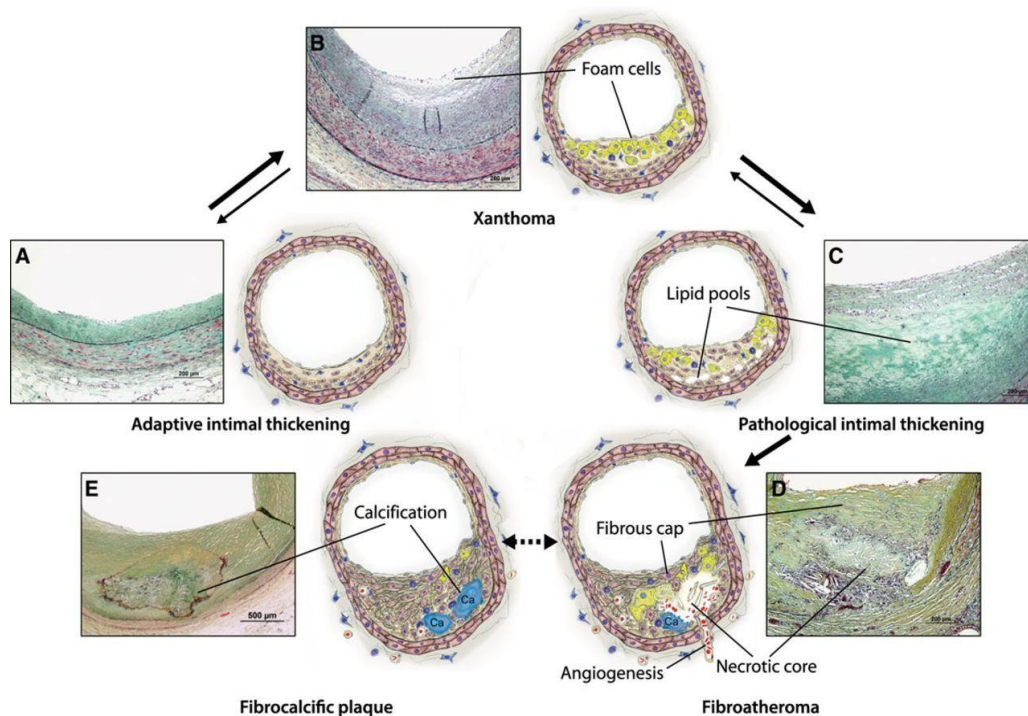


Figure 4: Lesion Types of Atherosclerosis & Theorized Sequence of Development ²³

As seen above, the adaptive intimal thickening (A) emerges as a crucial stage. This phase is characterized by the accumulation of smooth muscle cells within the intima, the innermost layer of the arterial wall, including the endothelial surface ²³. As the process advances, foam cell macrophages gather in the intima (B), forming a xanthoma or cholesterol-rich material buildup. This transforms into lipid pools with subtle necrotic regions (C) and eventually evolves into a fibroatheroma (D) or fibrous cap atheroma, the initial advanced lesion according to the AHA classification scheme ²⁴. This fibroatheroma exhibits a characteristic lipid-rich necrotic core enveloped by collagen-rich fibrous tissue. Further along, atheroma progression may culminate in calcification (E), rendering arteries rigid and less capable of expansion and contraction, thereby limiting the blood flow to heart muscles ²³.

What may also occur is that of an ACS whereby, after the development of a fibroatheroma, the artery becomes blocked. As previously mentioned, plaque rupture involves the rupture of a vulnerable atherosclerotic plaque, resulting in thrombus formation and subsequent myocardial ischemia. This intricate process is underscored by multiple factors, with inflammation taking a prominent role. In contrast, Plaque erosion introduces an alternative mechanism for ACS, marked by the disruption of the endothelial surface without rupturing the fibrous cap.

The critical role of endothelial disruption in plaque erosion's pathogenesis, illustrated in **Figure 5**, is a product of clinical observations, intravascular imaging insights, histopathological investigations, and experimental models ²⁵⁻²⁷. Clinical observations of ACS events that lack conspicuous fibrous cap rupture led to explorations of alternative mechanisms, ultimately unveiling plaque erosion as a distinctive phenomenon ²⁷. Histopathological analyses of thrombosed coronary arteries in ACS patients revealed instances where the fibrous cap remained intact, but the endothelium was absent, providing direct evidence of endothelial disruption ²⁶. High-resolution intravascular imaging techniques, particularly OCT, facilitated meticulous visualization of coronary plaques, uncovering

features linked to erosion ²⁵. Complementary animal models and biomarker studies further affirmed endothelial dysfunction's role in driving plaque erosion ²⁸.

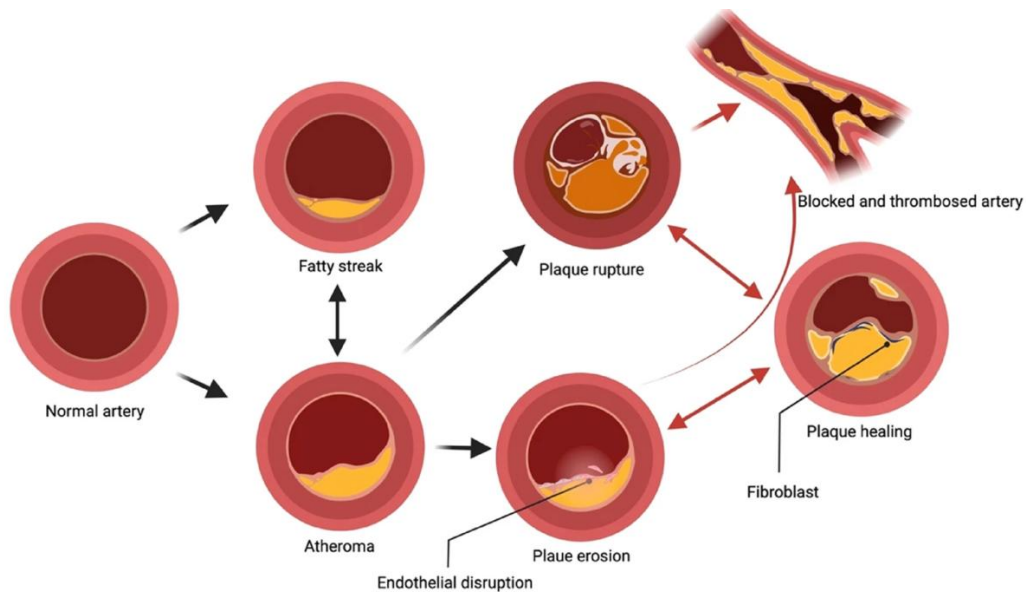


Figure 5: Atherosclerotic Plaque Development: Rupture vs. Erosion²⁹

However, the exact molecular and cellular events triggering endothelial disruption and subsequent erosion remain subjects of ongoing research. While both plaque erosion and plaque rupture can contribute to STEMI or NSTEMI ACS, approximately 75% of STEMI cases are linked to plaque rupture, whereas plaque erosion accounts for 30-40% of NSTEMI cases ³⁰⁻³². Plaque erosion in STEMI scenarios triggers substantial thrombus formation, contrasting with lesser thrombus formation observed in NSTEMI patients with plaque erosion. Nonetheless, the precise underlying reasons for these differences remain elusive ^{31,32}.

Recent comparative studies have illuminated clinical, morphological, and molecular disparities between these two entities contributing to ACS. Collectively, these studies suggest that erosion-ACS constitutes a distinct disease entity ^{31,33}. Yet, the complete picture remains incomplete, and the precise pathomechanism of plaque erosion continues to challenge our understanding.

1.4 Clinical Presentation

The clinical manifestation of ACS heavily diverges depending on the underlying mechanism. While certain features may overlap, a clear grasp of distinct characteristics is pivotal for accurate diagnosis and effective management. Chest Pain is a primary presenting symptom in both erosional and ruptured ACS cases. Yet, this pain's nature, intensity, and duration often differ significantly. In ruptured ACS, the pain is typically intense and prolonged, often characterized as a pressure-like or squeezing sensation. Conversely, erosional ACS manifests with milder and more transient angina episodes, which might be less intense or associated with exertion ³⁴. ECG readings offer critical diagnostic insights to differentiate between erosional and ruptured ACS. Ruptured ACS often exhibits ST-segment elevation in the ECG as they are commonly STEMI and therefore indicate complete coronary artery occlusion. Conversely, ECG findings in erosional ACS might display subtle or absent ST-segment elevation, possibly accompanied by dynamic alterations or T-wave inversions as seen in **Figure 1** ³⁵.

Measuring cardiac biomarkers, particularly troponins, plays a central role in diagnosing ACS. In ruptured ACS, troponin levels frequently surge due to myocardial necrosis from complete coronary artery occlusion. In contrast, erosional ACS may initially yield harmful or minimally elevated troponin levels. However, considering serial measurements and dynamic changes over time is essential, as troponin elevation may become apparent later ³⁵.

As the assessment of clinical manifestation weighs heavily on assuming a full occlusion is likely a rupture ACS, atypical symptoms are more likely to characterize erosional ACS; particularly in specific populations such as women and individuals with diabetes. These symptoms can encompass indigestion, fatigue, dyspnea, or discomfort beyond the chest region ³⁵. Atypical symptoms can complicate the diagnostic process, emphasizing the importance of maintaining a high level of suspicion to prevent misdiagnosis. Recognizing the variability in the clinical presentation of ACS among individuals is crucial and therefore requires a deeper understanding of an underlying mechanism.

1.5 Diagnostic Evaluation

Accurate and timely diagnosis is a cornerstone in managing ACS, as it guides effective interventions. The diagnostic process encompasses a comprehensive array of tools, including clinical assessment, ECG, cardiac biomarker analysis, and various imaging studies. A recent focus seminar at The Journal of the American College of Cardiology (JACC) with top stakeholders proposed a movement to diagnostic evaluations classifying between plaque rupture and erosion to make way for future therapeutic implications ³⁶. OCT's unparalleled resolution allows clinicians to distinguish between plaque characteristics by visualizing distinct features as a classification algorithm as showcased in Figure 6.

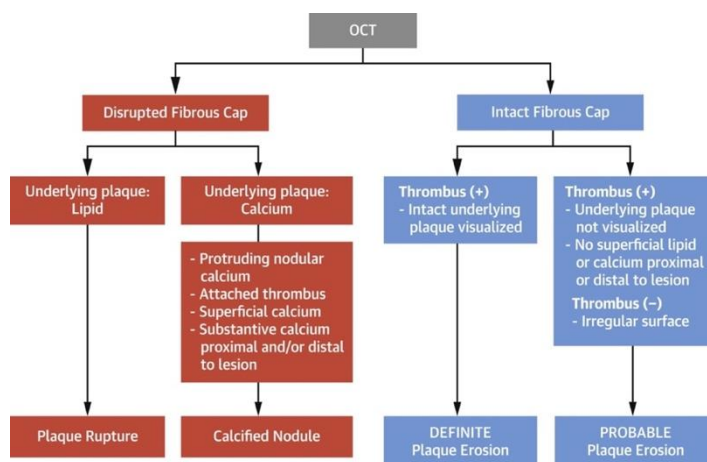


Figure 6: ACS Diagnostic Decision Tree using OCT ³⁶

1.6 Management & Treatment Outcomes

The realm of research investigating differential outcomes between patients with plaque rupture and plaque erosion-associated ACS is continuously evolving, mirroring the intricate nature of individual cases, healthcare system nuances, and the ongoing evolution of medical science. While plaque rupture typically necessitates immediate revascularization procedures like PCI to restore blood flow and rescue myocardial tissue, determining the most effective approach for treating plaque erosion remains an ongoing inquiry.

Clinicians have traditionally gravitated towards PCI for patients with plaque rupture due to the well-established benefits of revascularization. Swift intervention reduces ischemic duration and limits

heart muscle damage. For STEMI patients in general, rapid intervention with shortened door-to-balloon times is associated with enhanced outcomes, reduced mortality rates, and improved myocardial recovery ³⁷. The strides made in PCI techniques, stent innovations, antithrombotic medications, and supplementary therapies have markedly elevated patient outcomes ³⁸. However, the intricate pathophysiological underpinnings of plaque erosion necessitate a distinct treatment approach.

For plaque erosion, the optimal therapeutic strategy remains to be definitively established. Management approaches for erosion-associated ACS prioritize antithrombotic therapies, comprehensive medical care, and addressing underlying factors such as inflammation and endothelial dysfunction. An intriguing revelation from the EROSION study (Effective Anti-Thrombotic Therapy Without Stenting: Intravascular Optical Coherence Tomography- Based Management in Plaque Erosion) found that patients treated with cilostazol, an antiplatelet, anti-inflammatory, and vasodilator medication, displayed significantly reduced incidences of erosion-related ACS events compared to the control group ³⁹. This implies that tailoring treatment strategies to the precise pathophysiological mechanisms of plaque erosion may be pivotal in achieving more favorable outcomes. Additionally, a separate study by Arbustini et al. reported a significantly lower prevalence of major adverse cardiovascular events (MACE) at one year in patients with erosion-ACS compared to those with rupture-ACS ³¹.

Chapter 2. The Role of Immune Cells in ACS

2.1 A Shifted Perspective on Atherosclerosis

The intricate interplay between the immune system and atherosclerotic plaque formation has garnered significant attention in the field of ACS research. Historical landmarks and paradigm shifts have marked the journey to comprehending the immunological intricacies of ACS. Atherosclerosis, once viewed predominantly as a lipid deposition disorder, is now recognized as a complex inflammatory disease involving immune cells interacting with vascular components and influencing plaque vulnerability ⁴⁰. This shift in perspective underscores the significance of immune cells in the mechanisms underlying ACS, including plaque rupture and erosion.

The discovery that inflammation and atherosclerosis were connected traces back to observations made over a century ago. Rudolf Virchow's pioneering work in the 19th century noted leukocyte infiltration within atherosclerotic lesions, hinting at an inflammatory component ⁴¹. Although, it was not until the late 20th century that inflammation was more deeply connected to atherosclerosis as an important driving force. The landmark discovery of immune cells within atherosclerotic plaques heralded a new era of research. The initial focus on macrophages and monocytes soon expanded to encompass other immune cell types, including T-cells ⁴². Studies in animal models and human specimens illuminated the dynamic interactions between immune cells, endothelial cells, and smooth muscle cells, orchestrating a localized inflammatory response within the plaque microenvironment ^{43,44}.

The exploration of T-cell involvement in atherosclerosis has been remarkably insightful. The role of T-cells in orchestrating the immune response by playing a dual role within atherosclerotic plaques, acting as both potential modulators of inflammation and contributors to plaque vulnerability. Therefore, a better understanding of T-cell mechanisms of maturation, activation, and differentiation in ACS is quintessential to improved patient outcomes.

2.2 T-Cell Maturation and Activation

T-cells, as part of the body's white blood cells (WBCs) or lymphocytes, undergo maturation in the thymus ⁴⁵. In the thymus, precursor cells undergo an education process, where they learn to distinguish between self and non-self-antigens as seen in **Figure 7**. Originating in the bone marrow or fetal liver, early thymic progenitor cells (ETPs) or CD4⁻ CD8⁻ double negative (DN) cells enter the thymus, where they progress through four DN stages (DN1-4) T-cells. If cells bind too strongly to self-antigens, they undergo apoptosis and negative selection; ensuring the survival of T-cells the body positively selected as appropriately educated. The elimination of T-cells that exhibit a strong affinity for self-antigens is a critical safeguard for the prevention of autoimmunity and therefore pro-inflammatory responses. This education also involves the complex process of T-cell receptor (TCR) gene rearrangement. This creates a vast array of TCRs, with unique antigen recognition potential. The diversity of TCRs allows T-cells to recognize a wide range of antigens. During T-cell development in the thymus, TCR genes undergo somatic recombination to generate a diverse repertoire of TCRs. This process, called Variable-Diversity-Junctional (V(D)J) recombination, combines gene segments to create unique TCR variable regions. As a result, each T-cell clone expresses a distinct TCR with a specific antigen recognition capability. TCR genes are located on different chromosomes, with the αβ TCR genes located on chromosome 14 in humans and the γδ TCR genes on chromosome 7 ⁴⁵.

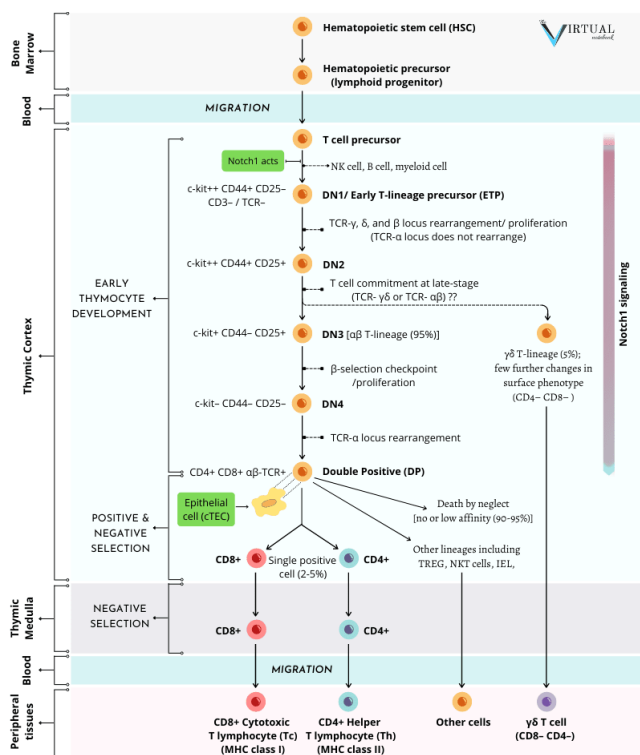


Figure 7: T-cell Maturation & Notch signaling ⁴⁶

As T-cells undergo the complex process of TCR gene rearrangement, a critical player emerges—Notch signaling as seen in **Figure 7**. Notch signaling is a key regulatory mechanism that guides T-cell fate decisions during thymic development. Activation of Notch receptors by ligands on thymic stromal cells directs T cells toward specific developmental pathways, ensuring proper maturation and function ⁴⁷.

Notch signaling also has implications in autoimmune diseases and inflammatory conditions. The dysregulation of Notch signaling can greatly influence immune cell differentiation and function. In multiple sclerosis and rheumatoid arthritis, for example, a disturbed Notch signaling pathway can contribute to the continuation of inflammation and the overall dysfunction of the immune system ⁴⁶.

T-cells exit the thymus upon maturation and enter the bloodstream through specialized blood vessels, allowing for migration to lymphoid organs such as lymph nodules and spleen. In both bloodstream and lymphoid, the mature T-cells are predisposed to recognize specific antigens

presented on major histocompatibility complexes (MHC) by antigen-presenting cells (APCs), such as by dendritic cells (DCs), as shown in **Figure 8**. This recognition sparks a cascade of immune responses, including activation, clonal expansion, and effector function execution ⁴⁵.

Antigen presentation by APCs activates T-cells by interacting with the TCR and the antigenic peptide-MHC molecule. This interaction triggers intracellular signaling pathways that promote T-cell activation and proliferation. Co-stimulatory signals, such as CD28-B7 interaction, aid in regulating T-cell clonal expansion as seen in **Figure 8** ⁴⁸. Engaging co-stimulatory molecules provides the secondary signals required for amplifying T cell activation and expansion. In the absence of co-stimulation, a T-cell may fail to undergo robust clonal expansion or undergo anergy. *Anergy* is a tolerance mechanism in which the lymphocytes are intrinsically inactivated functionally following an antigen encounter but remain alive for an extended period in a hyporesponsive state.

T-cell clonal expansion is a fundamental process in adaptive immunity that amplifies antigen-specific T-cell responses. Upon encountering a specific antigen, T-cells become activated and differentiate into effector T-cells, such as cytotoxic and helper T-cells ⁴⁵.

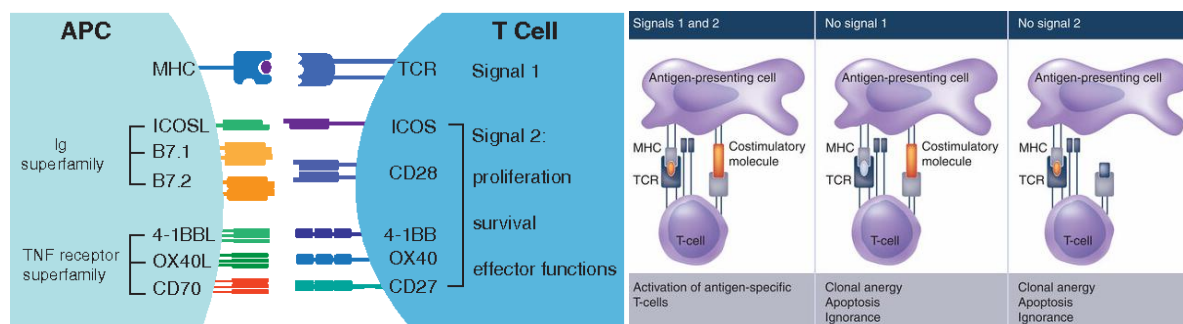


Figure 8: T-Cell Activation via MHC and Co-stimulatory Pathways ^{48,49}

2.3 T-Cell Differentiation

T-cells display diversity through distinct subsets as seen in **Figure 9**, each with unique roles. By restricting to MHC class II pathways, CD4⁺ T-cells are pivotal in coordinating immune reactions by producing cytokines that direct various immune cell activities. After an encounter with an antigen, CD4⁺ T-cells differentiate into three main categories of CD4⁺ effector T-cells: helper T-cells (T_H), T follicular helper (T_{FH}) cells, and regulatory T-cells (Treg). T_H cells can further be easily sub-defined by their expression of distinct cytokines: T helper 1 (T_{H1}), T_{H2}, T_{H9}, T_{H17}. These differentiated subgroups are not necessarily definitive as some degree of plasticity can be observed, however, T_{H2} cells would typically express interleukin (IL) 4 while T_{H17} expresses tumor necrosis factor alpha (TNF-α) ⁴⁵. Tregs, which arise from a different differentiation lineage, uphold immune tolerance by suppressing excessive responses against self-antigens, mitigating autoimmune reactions ⁵⁰. Another key factor to understand is the plasticity of T-cells in differing environments, which is an issue of great investigation. The plasticity of T_{H17} cells, for example, in which T_{H17} cells can transition into T_{H1}-like cells or other way called T_{H1}-T_{H17} cells. These cells are associated with cellular immunity and the defense against intracellular pathogens. This plasticity is particularly relevant in autoimmune diseases where both T_{H17} and T_{H1} responses are involved ⁵¹. T_{FH} cells navigate the world of germinal centers, fostering antibody production by guiding B-cells through affinity maturation and isotype switching.

CD8⁺ T-cells, also known as cytotoxic T-cells or cytotoxic T-lymphocytes (CTLs), are a subset of T-cells characterized by the presence of the cluster of differentiation (CD) 8 co-receptor on their surface. CD8⁺ T-cells play a crucial role in recognizing and destroying cells that are infected with intracellular pathogens, such as viruses. They recognize antigens presented on MHC class I molecules and are involved in cell-mediated immunity⁵².

Memory T-cells are a subset that emerges after the initial encounter with an antigen. While effector memory T-cells (T_{EM}) are primarily located in peripheral tissues and are immediately ready to mount immune responses, central memory T-cells (T_{CM}) reside in lymphoid tissues and provide long-term immune memory.

This subset is particularly intriguing in the context of atherosclerosis, where memory T-cells might retain information about prior endothelial insults or inflammatory events⁵⁴. In contrast, senescent T-cells, reflective of aging or chronic infections, demonstrate compromised function and may contribute to immune system deterioration. These cells serve as a reminder of the immune system's vulnerabilities⁵².

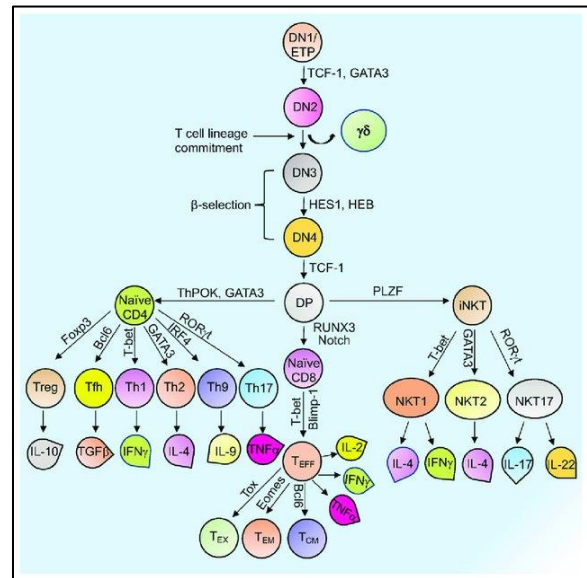


Figure 9: Main T-cell Differentiation⁵³

Invariant Natural Killer T (iNKT) cells bridge the gap between innate and adaptive immunity. Recognizing lipid antigens presented by CD1d molecules, iNKT cells rapidly secrete cytokines, influencing both innate and adaptive immune responses. They are active participants in various immune processes, including antimicrobial defense, inflammation, and regulation of autoimmune diseases⁴⁵.

Mucosal-Associated Invariant T (MAIT) cells, a unique lineage not noted in **Figure 9**, are abundant in mucosal tissues and recognize microbial metabolites presented by myofibrillogenesis regulator 1 (MR1) molecules⁴⁵. They contribute significantly to antimicrobial immunity at mucosal sites, playing a pivotal role in the early defense against bacterial infections. MAIT cells are also implicated in various inflammatory and autoimmune conditions⁵¹.

Gamma Delta (γδ) T-cells express a unique T-cell receptor composed of γ and δ chains, differing from the conventional αβ T-cell receptors. These cells exhibit tissue-specific distribution and respond to a wide range of antigens, including stress-induced molecules and microbial products. Gamma delta T-cells serve roles in immune surveillance, tumor immunity, as well as the regulation of immune responses⁵¹.

Terminal effector T (T_{TE}) cells represent a crucial subset of T-cells in the immune system, known for their rapid and specialized responses to infections⁵¹. What makes them particularly versatile is their ability to express both CD4 and CD8 surface markers. This dual positivity indicates their potential to differentiate into either CD4⁺ helper T-cells or CD8⁺ cytotoxic T-cells, depending on the specific immune response requirements. These cells have a relatively short lifespan and are generated during the acute phase of an immune response. Typically, terminal effector T-cells are found at the site of infection or inflammation, where they actively combat pathogens by releasing cytokines and performing cytotoxic functions, such as the release of granzymes and perforin. However,

once the infection is cleared, their numbers decline, making way for memory T-cells to provide long-term immunity.

2.4 T-Cell Receptors

T-cell receptors are membrane-bound proteins residing on the surface of T-cells and are critical components to adaptive immunity as well as the diversity of the adaptive immune system. TCRs orchestrate the body's defense against various pathogens and malignancies⁵⁷. TCRs are heterodimeric membrane proteins expressed on the surface of T-cells and recognize and bind to specific antigenic peptides presented by MHC molecules on the surface of APCs. This TCR-APC interaction triggers a cascade of signaling events, ultimately leading to T-cell activation and the initiation of immune responses. These receptors hold the power of specificity, with each T-cell carrying a unique TCR variant. Structurally, TCRs consist of α and β chains in $\alpha\beta$ T cells or γ and δ chains in $\gamma\delta$ T cells. Their primary function revolves around recognizing antigens as peptide fragments, presented by MHC molecules on APCs. This recognition is the cornerstone of T-cell mediated adaptive immune responses⁵⁸.

A primary focus of scientific investigation is diversity of TCRs, arising from gene rearrangement during T-cell development as seen in **Figure 10**. TCR diversity arises through random selection and gene rearrangement during T-cell development. Each TCR consists of a VDJ or variable (V), diversity (D), and joining (J) gene segment, allowing for the generation of a vast array of unique TCR sequences⁵⁷.

The repertoire of the TCR is oftentimes investigated using the three diversity indices: richness, entropy, and the Gini-Simpson index.

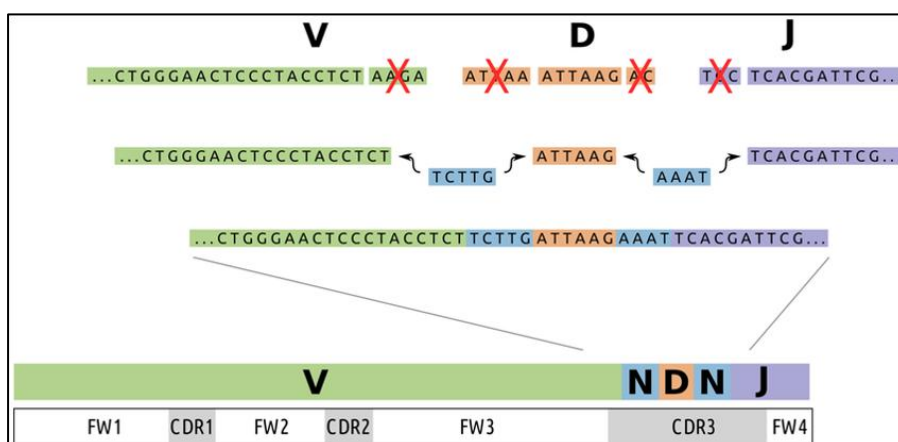


Figure 10: TCR Gene Rearrangement⁵⁹

Diversity indices are mathematical measures used to quantify the diversity of TCR repertoires. They provide insights into the variety and distribution of different TCR sequences within a T-cell population. One index, richness, is a straightforward measure of diversity that counts the total number of unique TCR sequences present in a sample⁶⁰. Richness therefore shows how many different types of TCRs are in each population. Richness provides a basic understanding of the number of distinct TCR variants present, but it doesn't consider the relative abundance or evenness of these variants. The Shannon index considers both the number of different TCR sequences (richness) and their relative abundances within a population. It provides a more comprehensive measure of diversity by considering not only the variety of TCRs but also the distribution of those variants⁶⁰.

A method used to analyze the differences among TCR repertoires is via categorizing or binning based on abundance or frequency⁶¹. Hyperexpanded clonotypes are notably dominant, comprising a small yet significant group of highly expanded immune cells with closely matching receptor sequences. They signify a potent and focused immune response, often directed at a specific antigen like a pathogen or tumor. Large clonotypes are abundant, though not as overwhelmingly prevalent as hyperexpanded ones. They hold functional importance in the immune response. Medium clonotypes, moderately abundant, contribute to the repertoire without being dominant. Small clonotypes, less common but still detectable, play a role in immune surveillance and diversity. Rare clonotypes, found in very low frequencies, add to the immune repertoire's diversity, even though their functional impact is limited. These categorizations help analyze immune receptor diversity, shedding light on the dynamics and significance of different clonal populations within a sample. The specific thresholds for these categories may vary based on the study and analytical methods employed.

2.5 T-Cell Mechanisms: Rupture vs. Erosion

The theorized mechanism of T-cell involvement in plaque rupture primarily centers on T_{H1}-driven inflammation⁶². T_{H1} cells play a pivotal role by releasing pro-inflammatory cytokines, particularly interferon-gamma (IFN- γ)⁴⁵. These cytokines activate macrophages, amplifying the inflammatory response within the atherosclerotic plaque. The cascade of events triggered by T_{H1} cells leads to collagen degradation, resulting in the thinning of the fibrous cap covering the lipid-rich core of the plaque. Additionally, the inflammatory balance of T-cell subsets and macrophages contribute to plaque instability by releasing matrix-degrading enzymes and further propagating the pro-inflammatory environment as depicted in **Figure 11** below⁶³.

In cases of plaque rupture, the fibrous cap becomes thin, typically measuring only ± 60 to 70 micrometers⁶⁴. T_{H1} cytokines, particularly IFN- γ , adversely affect the ability of smooth muscle cells (SMCs) to synthesize new collagen, impairing the repair and maintenance of the extracellular matrix of the fibrous cap. Matrix-degrading proteinases, heavily regulated by inflammatory mediators, become overactive and contribute to the dissolution of interstitial collagen, further weakening the fibrous cap⁶².

A subset of T_{H1} lymphocytes, known as CD4⁺CD28^{null} cells, has been identified in unstable ruptured atherosclerotic plaque⁶⁴. Their frequency has shown a direct relation to the risk of acute ACS. CD4⁺CD28^{null} T-cells are oligoclonal lymphocytes rarely found in healthy individuals younger than 40 years but are often present in high frequencies in patients with chronic inflammatory diseases and elderly individuals⁶⁴. Oligoclonal lymphocytes are where a small number of genetically similar cells or antibodies are produced, typically because of a limited immune response⁶⁵. These cells appear to be highly resistant to activation-induced cell death, suggesting altered responses to apoptosis-inducing signals⁶⁵.

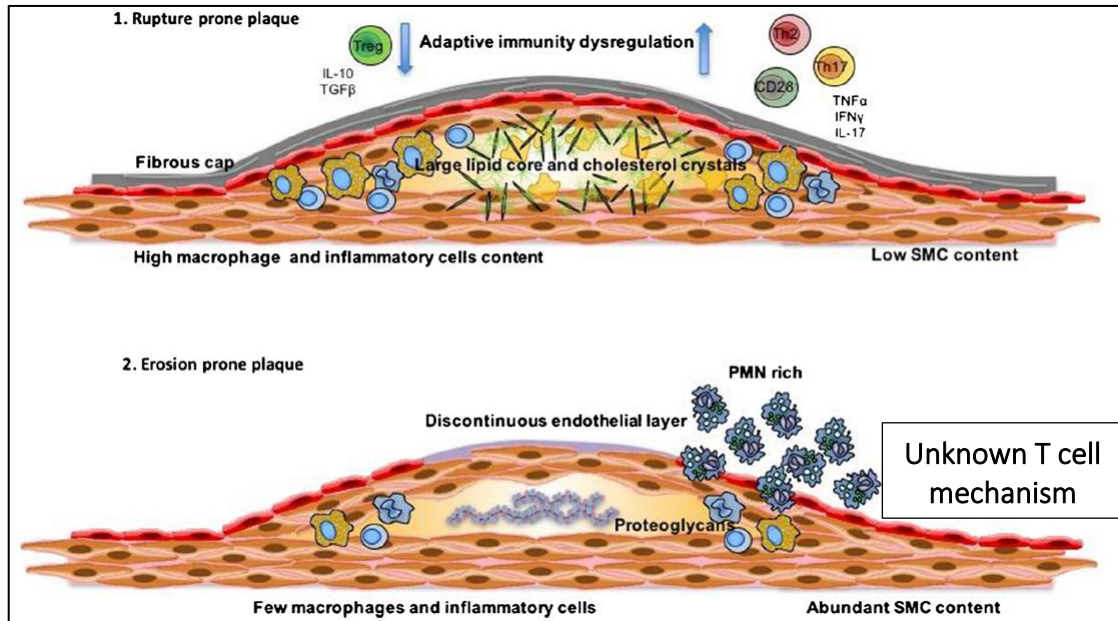


Figure 11: Comparison of Immune Cell Interactions: Rupture vs. Erosion⁶⁵

Contrasting with plaque rupture, plaque erosion involves a different immunological mechanism, polymorphonuclear neutrophils (PMNs) contribute to the inflammatory response and are believed to play a role in the erosion of the endothelial lining of the plaque⁶⁵. CTLs may have a role in plaque erosion as they are known for their ability to directly kill target cells, including endothelial cells⁶⁶. CTLs can contribute to the disruption of the endothelial barrier in plaque erosion, further exacerbating the inflammatory response.

Nonetheless, several aspects warrant further investigation. The precise triggers initiating plaque erosion, including specific antigens, or signaling molecules, are yet to be fully elucidated. T_H17 related cytokines, including IL-17, have been associated with the upregulation of specific matrix metalloproteinases (MMPs), which are enzymes that can degrade extracellular matrix components⁶⁷. These mentioned MMPs are MMP-2 and MMP-9, which can contribute to the degradation of the structural support to endothelial cells, therefore creating a theorized role of T_H17 cells playing a role in plaque erosion, however, much is left to be investigated⁶⁷.

Furthermore, exploring the role of other immune cell types, such as B-cells, dendritic cells, and natural killer cells, in the context of plaque erosion may provide a more comprehensive understanding of the immunological milieu. Additionally, understanding the interactions between T-cells and endothelial cells and their contribution to endothelial dysfunction in plaque erosion remains an important area for future research.

2.6 Beyond T Cells: The Multifaceted Immune Involvement

While T-cells occupy a central stage, the immunological landscape of ACS extends beyond their influence. Other immune cell subsets substantially contribute to plaque dynamics, interacting with T-cells and plaque-resident cells to shape the disease process. Macrophages, for instance, play dual roles in plaque progression. While some macrophages contribute to inflammation and plaque vulnerability by releasing pro-inflammatory cytokines and proteases, others exhibit anti-inflammatory functions and assist in resolving inflammation⁶⁹.

PMNs contribute to plaque erosion and endothelial damage through various mechanisms. In response to pro-inflammatory signals, PMNs are recruited to atherosclerotic plaques, where they release inflammatory mediators, including cytokines and chemokines, amplifying the local inflammatory environment⁶⁴. PMNs can also form NETs, which, while intended to trap pathogens, can contribute to tissue damage, including endothelial cell damage⁴⁵. Additionally, PMNs produce reactive oxygen species (ROS), and excessive ROS production can lead to oxidative stress and endothelial cell dysfunction⁶⁴. Interactions between PMNs and other immune cells within the plaque further activate immune responses, exacerbating endothelial damage⁶⁷.

Dendritic cells, known as professional antigen-presenting cells, bridge innate and adaptive immune responses. Their presence within plaques suggests their involvement in shaping the immune milieu, including T-cell responses, within the atherosclerotic lesion⁷⁰. Mast cells have been linked to plaque destabilization due to their ability to secrete mediators that promote inflammation and angiogenesis and are therefore often associated by their role in allergic responses,⁷¹. B-cells are critical players in humoral immunity and also contribute to the atherosclerotic process. B-cells ability to modulate the immune response by producing antibodies and cytokines allows for them to either enhance or dampen inflammation⁴⁵.

The collaboration between these diverse immune cell subsets is far from linear, creating a complex network that shapes plaque stability or rupture. The multifaceted immune involvement in ACS provides multiple potential targets for therapeutic interventions. Strategies aimed at modulating macrophage polarization, inhibiting dendritic cell activation, or tempering mast cell degranulation are emerging as promising avenues for stabilizing vulnerable plaques^{72,73}. The intricate interplay between various immune cell subsets necessitates a comprehensive approach considering their collaborative impact on plaque dynamics.

Chapter 3. Next Generation Sequencing

3.1 Single Cell RNA Sequencing with Droplet Microfluidics

Water-in-oil based droplet microfluidic technologies use a water-based solution as the dispersed phase and oil with a surfactant as a continuous phase⁷⁴. The flows of these two phases are controlled by microfluidic pumps. As soon as fluids meet, water-in-oil droplets are formed and stabilized by the surfactant dissolved in the oil carrier phase as seen in **Figure 12**. Droplets can be loaded with single cells by using a dilute cell suspension as the aqueous phase. The distribution of cells in droplets follows a Poisson distribution, minimizing the risk of encapsulation of multiple cells in one droplet but yielding up to $\pm 90\%$ of droplets containing no cells⁷⁵.

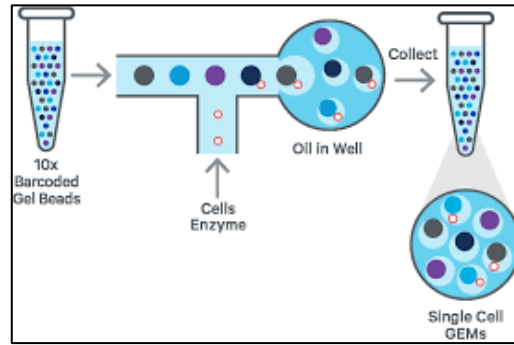


Figure 12: GEM formation via 10x Protocol ⁷⁷

There are multitudes of technologies that utilize droplet microfluidics to differing benefits and specifications. One widely used commercial option is the 10x Genomics Chromium platform using Gel Bead-In-Emulsions (GEMs), in which co-encapsulation of a barcoding bead and single cells using droplet microfluidics is completed with library preparation consisting of reverse transcription with template switching and PCR amplification ⁷⁶. In addition, since 3' coverage starting from the polyadenylic acid tail or poly(A) tail tends to lead to an underrepresentation of the 5' end of the mRNA, the chromium platform allows for single cell gene expression 5' by including a template switch oligo (TSO) sequence at the end of the barcoding primers instead of a poly-deoxythymidine or poly(dT) tail. As there are technologies to remove droplets with multiple cells inside of one droplet, there is a technique to 'superload' the microfluidic rate to carefully load a higher number of cells onto the chip than the recommended limit. Researchers do this to maximize the throughput and efficiency of the single-cell RNA sequencing (scRNA-seq) experiment, enabling the analysis of a larger number of cells in a single run. However, superloading requires careful optimization and validation to ensure that it does not compromise data quality or introduce biases ⁷⁶.

3.2 Multiplexing and Demultiplexing Samples

Cell multiplexing in single-cell sequencing is the process in which simultaneous analysis of multiple samples or conditions are undertaken within a single experiment ⁷⁹. One advanced method for achieving multiplexing is through a technique known as 'cell hashing' which utilizes oligonucleotide-tagged antibodies to label cells with specific Deoxyribonucleic acid (DNA) barcodes or hashtags. These barcodes can be thought of as cell-specific identifiers. When cells from different samples are mixed, they are individually labeled with different DNA hashtags, allowing them to be distinguished during the subsequent steps of library preparation and sequencing. An example of an oligonucleotide-tagged antibody and its different components may be seen in **Figure 13** below.

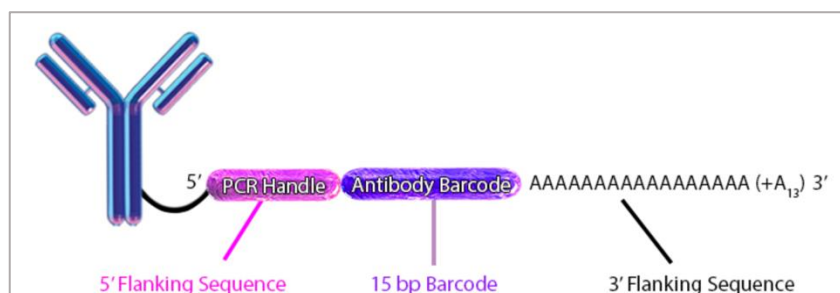


Figure 13: Example of an oligonucleotide-tagged antibody by Biolegend ⁷⁹

One method for cell demultiplexing in single-cell sequencing is to employ the concept of oligonucleotide hashtags to distinguish and categorize individual cells within a mixed sample. This technique relies on the incorporation of unique barcode sequences, or hashtags, into the cellular Ribonucleic acid (RNA) or DNA during library preparation⁷⁹. Each cell is assigned a distinct combination of these molecular tags. During sequencing, the hashtags are read alongside the cellular transcriptome, enabling the identification of which cell produced a specific read. Advanced computational algorithms then parse the data, sorting sequences based on their associated hashtags⁸⁰. This demultiplexing process allows researchers to dissect complex cell populations, decipher the unique genetic profiles of individual cells, and unraveling intricate biological processes. Oligonucleotide hashtags have revolutionized single-cell genomics by enhancing data accuracy and expanding our understanding of cellular heterogeneity, contributing to groundbreaking discoveries in fields such as cancer biology, immunology, and neuroscience⁸¹.

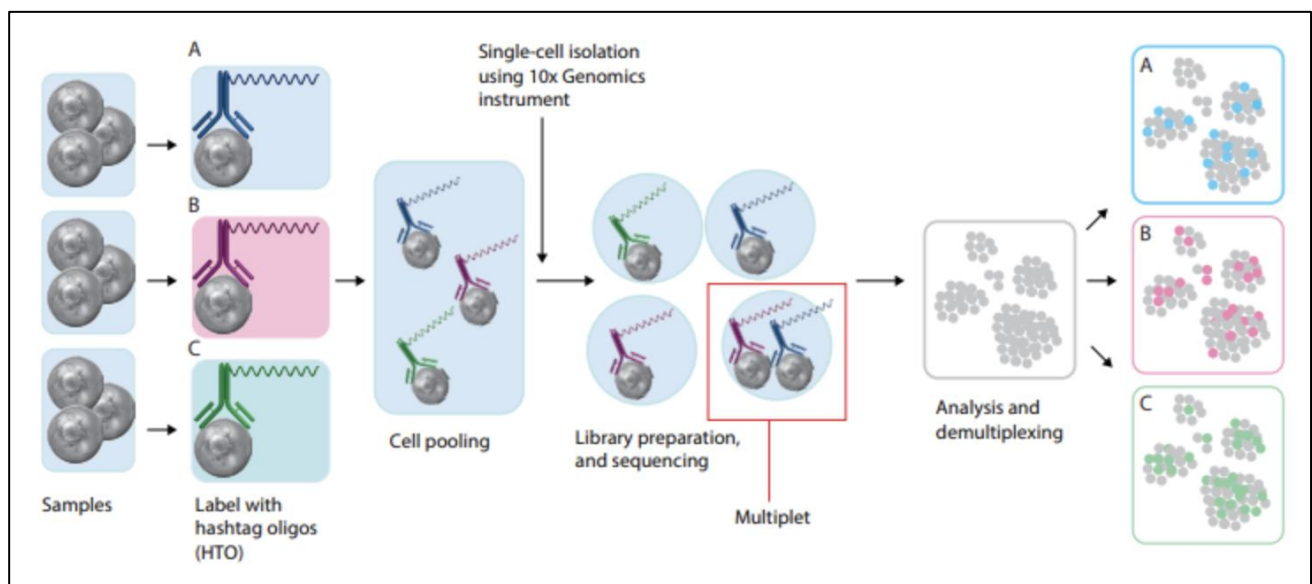


Figure 14: Multiplexing & Demultiplexing Process Overview⁷⁹

3.3. Data transformation Files: FASTA to FASTQ

In the realm of scRNA-seq and the transition from sequencing to data analysis, distinguishing between FASTA and FASTQ file formats holds significant importance. FASTA (FAST-ALL) is a text-based format used to store biological sequences like nucleotide or amino acid sequences, typically accompanied by brief headers for each sequence⁸². It primarily contains the raw sequence data, making it suitable for storing reference genomes, gene sequences, or transcripts. Conversely, FASTQ (FAST-QUALITY) is another text-based format that not only stores sequences but also incorporates associated quality scores for each base. Each record in a FASTQ file includes a sequence identifier, the actual sequence, a separator line, and quality scores. This format is extensively used in sequencing applications such as scRNA-seq, encompassing raw sequence data and crucial quality information essential for downstream analysis and quality control. In the context of scRNA-seq, FASTQ files serve

as the primary output of the sequencing process, providing the individual reads for each sequenced cell, complete with nucleotide sequences and quality scores. These files act as a foundational resource for critical processes like read alignment, transcript quantification, and cell barcode extraction ⁸³. Discerning the distinctions between FASTA and FASTQ is paramount for the effective management and processing of sequencing data in scRNA-seq analysis workflows, ensuring the retention of quality information vital for accurate downstream analyses.

3.4 Uniform Manifold Approximation & Projection

Uniform Manifold Approximation and Projection (UMAP) has emerged as a transformative dimensionality reduction technique with widespread utility, particularly in the realm of scRNA-seq data analysis ⁸⁴. UMAP's core methodology revolves around constructing a high-dimensional graph representation of the data, where each data point (e.g., a single cell's gene expression profile) is connected to its nearest neighbors via pairwise distance or affinities based on metrics such as Euclidean distance and cosine similarity ⁸⁵. This connection forms a simplex as seen in **Figure 15** below while these mathematical metrics are often described as a K-nearest Neighbor (KNN) graph. This initial graph establishes the foundation for the subsequent optimization of a lower-dimensional embedding called a 'fuzzy topological structure' whereby the UMAP estimated connectivity or affinity strength between data points based on their distance to one another ⁸⁶. UMAP's strength lies in its ability to find a delicate equilibrium between preserving both local and global data structures, ensuring that the representation remains evenly distributed without the pitfalls of crowding, a challenge encountered by some other dimensionality reduction methods ⁸⁵. The optimization process in UMAP minimizes the distortion of pairwise distances between data points in the original high-dimensional space and their corresponding counterparts in the reduced-dimensional space, resulting in a lower-dimensional representation that accurately captures the intrinsic relationships between data points. The utilization of UMAP has been instrumental in unraveling the intricate landscapes of scRNA-seq data, offering unprecedented insights into cellular heterogeneity, differentiation processes, and functional states ⁸⁶. UMAP's proficiency in revealing both fine-grained details and overarching patterns within complex biological systems has significantly advanced scientific research and contributed to the broader understanding of intricate high-dimensional datasets.

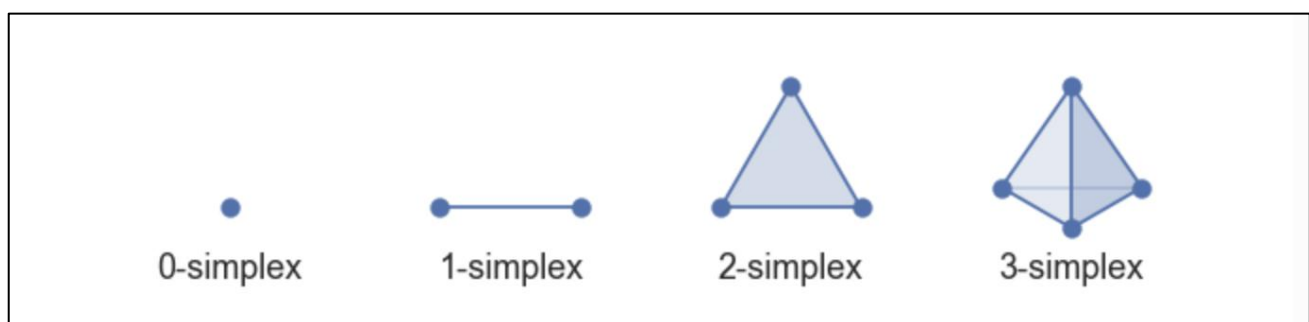


Figure 15: Simplices: The Core Building Blocks to Topological Spaces ⁸⁷

3.5 CITE-seq: Cellular Indexing of Transcriptomes & Epitopes

The cellular indexing of transcriptomes and epitopes (CITE-seq) stands as a groundbreaking convergence of scRNA-seq and high-throughput protein quantification. In the pursuit of understanding the complexities of cellular identity and function, CITE-seq offers a holistic approach by concurrently

capturing transcriptomic and proteomic data from individual cells. It accomplishes this through the incorporation of CITE-seq antibodies, oligonucleotide-labeled antibodies targeting cell-surface proteins⁸⁸. These antibodies facilitate the simultaneous quantification of gene expression and protein abundance, bridging the divide between genomics and proteomics.

At its core, CITE-seq operates within the framework of scRNA-seq. It begins by encapsulating single cells into droplets, employing cell-specific barcoding to label RNA molecules⁸⁹. However, CITE-seq introduces an additional layer of complexity by including CITE-seq antibodies. These antibodies bind to cell-surface proteins, and their associated oligonucleotides are co-encapsulated with the cell's RNA. Post-encapsulation, droplets are processed to release and amplify both the RNA and antibody-linked oligonucleotides, effectively linking transcriptomic and proteomic information for each cell⁸⁸.

The integration of transcriptomic and proteomic data via CITE-seq holds immense promise in deciphering complex cellular phenomena. It enables the simultaneous exploration of gene expression and protein abundance, thereby facilitating a deeper understanding of cell types, cellular state transitions, immune responses, and disease heterogeneity. An example of the benefits to investigating immune cells may be seen below in **Figure 16**, where the antibody expression or antibody derived tags (ADT) as well as RNA expression are comparatively different in side-by-side reference as reflected in biology⁴⁵.

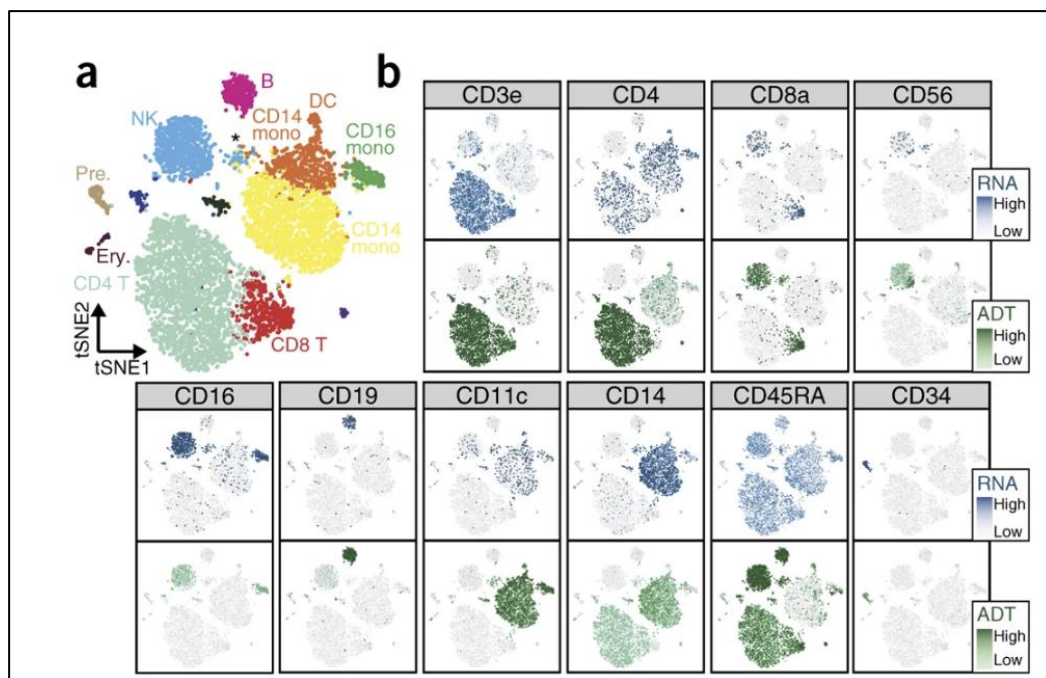


Figure 16: Cellular Indexing of Transcriptomes & Epitopes⁸⁸

3.6 Isotypes & Isotype Controls

In the context of immunology, an ‘isotype’ is a specific class or subclass of immunoglobulins, otherwise called antibodies, that share certain structural and functional characteristics⁴⁵. Immunoglobulins are produced by B-cells and play a critical role in the immune response through the recognition and and destruction of pathogens. In mammals, immunoglobulins are divided into five isotypes, each of which has distinct properties that make them suitable for different immune functions.

IgM, the first antibody produced during the primary immune response, forms a pentameric structure and is effective in agglutination, complement activation, and neutralizing early infections⁹⁰. IgG, the most abundant Ig in circulation, plays a versatile role in opsonization, complement activation, and immune memory. Notably, IgG crosses the placenta, providing passive immunity to the developing fetus⁴⁵. IgA, found in monomeric form in circulation and dimeric form in mucosal secretions, guards mucosal surfaces against pathogens and toxins by preventing attachment and neutralization⁹⁰. In contrast, IgE, although present in low abundance, triggers allergic responses by binding to allergens and activating mast cells, contributing to allergies and defense against parasites⁴⁵. Lastly, IgD, primarily located on B-cell surfaces, is involved in activation and differentiation, with its exact role still being explored⁴⁵. Together, these isotypes play pivotal roles in immune responses, encompassing defense, memory, allergic reactions, and mucosal protection.

An 'isotype control' in the context of flow cytometry as well as CITE-seq antibody panels, is a reference sample of a primary antibody that does not recognize the specific target antigen of interest in the given experiment⁹¹. Isotype controls are crucial for accurate data interpretation and compensation in flow cytometry analyses. They aid in distinguishing between true positive staining and non-specific binding of antibodies to cell surfaces. By using an isotype control that matches the isotype of the primary antibody, researchers can determine the background fluorescence level and set appropriate gating parameters to distinguish signal from noise⁹¹.

3.7 TCR Sequencing Technologies

Single-cell TCR sequencing (scTCR sequencing), such as the 10x VDJ kit, typically involves isolating individual T-cells in separate reaction chambers and amplifying their TCR chain gene regions using PCR⁹⁵. The amplified TCR sequences are then subjected to high-throughput sequencing. This approach ensures that the DNA or RNA from a single T-cell is sequenced independently⁹⁵. Due to single cell isolation methodology all chain forms can be sequenced (β , α , γ , and δ -chains). Therefore, the T cells entire TCR is sequenced, whether $\alpha\beta$ or $\gamma\delta$ T cells. Through bioinformatics analysis, unique TCR sequences are assigned to each individual T-cell, enabling the reconstruction of clonal lineages and diversity at the single-cell level⁹⁵. This technique is beneficial when investigating clonality as it provides the full clonotype of a T-cell as opposed to just the β -chain. In addition, as all chains of the TCR provide to the shape, they also affect the shape of the antigen-binding site, which in turn affect antigen specificity and diversity of T-cells.

3.8 Weighted Nearest Neighbor Analysis

Weighted Nearest Neighbor (WNN) analysis is an approach that enhances the construction of UMAP embeddings by incorporating weights when computing the pairwise distances between cells or simplexes⁹⁶. This method aims to improve the representation of high-dimensional scRNA-seq data in a lower-dimensional space, such as a UMAP plot. In traditional scRNA-seq UMAP construction, a KNN graph is constructed as previously mentioned in section 3.4. In WNN analysis, weighted similarities are assigned which allow for the KNN graph to be curated based on a stochastic relationship between both modalities, such as in the case of CITE-seq for dual RNA and protein expression. This multimodal relationship is weighed based on which immune cells the algorithm is constructing the KNN graph for at the time. The exact data that was used for the supervised stochastic modeling of said immune cell weights has been published in Hao et al.'s 2021 Cell paper⁹⁶.

3.9 Cell Annotation Via Anchoring

Query-reference anchoring is a powerful tool for the annotation and interpretation of scRNA-seq data. As depicted in **Figure 17** below, query-reference anchoring normally undergoes a type of correlation analysis between a reference data set and new data, such as via conical correlation analysis (CCA), allowing for similarities to be found against two different and separate data matrixes (**17A**)⁹⁷. By having one data matrix cells fully annotated, this reference dataset may be compared to a non-annotated or query matrix of similar cells. Once CCA has found linear correlations or anchors (**17C**), these anchors are assigned correspondence scores of similarities to their neighbors. These scores may be manually adjusted to filter for higher-score correspondence (**17D**) or lower (**17E**) depending on the research question at hand. Once package that utilizes Query-reference anchoring, uniquely with CITE-seq multimodal information, is the package *Azimuth* – often referred to as the ‘App for reference-based single-cell analysis’⁹⁷.

Azimuth computes similarity scores between individual single cell query data against CITE-seq reference populations based on gene and antibody expression patterns. Depending on the selected reference library, subsequently assigning of cell type or state annotations are assigned based at varying depth of resolution⁸⁶. Quality control measures and visualizations facilitate reliable annotations and provide a robust foundation for downstream analyses. While specific references for *Azimuth* may be limited, its functionality is integrated within the Seurat framework, with details about its use available in the official Seurat documentation^{86,96}.

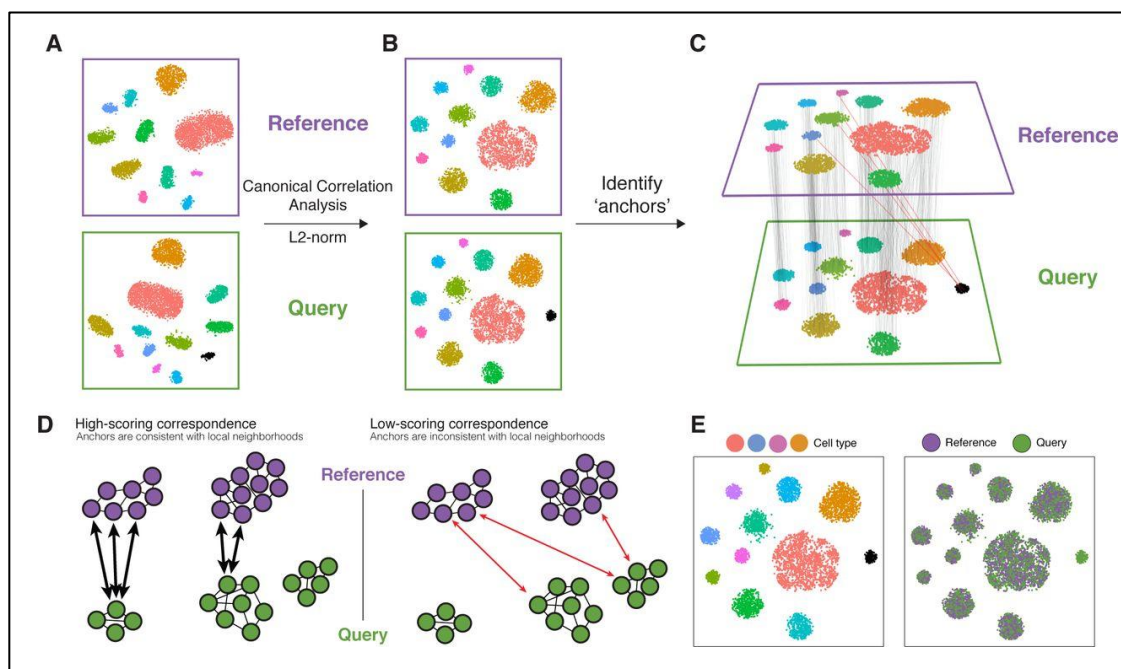


Figure 17: Cell Annotation via Reference-Query Anchoring⁸⁶

While *Azimuth* utilizes data based on both transcriptomic and protein expression single cell data, several annotation packages allow for anchoring based annotation from RNA-based reference

libraries. These packages, such as *SingleR* for query-reference analysis and *CellDex* for reference libraries themselves, are especially beneficial when on single cell research at a high resolution, for example, with several T-cell subsets ⁹⁸.

AIMS & OBJECTIVES

Chapter 4. Investigation Aim

4.1 Recent Findings: Unravelling Discrepancies between Erosional and Ruptured ACS

In 2020, collaborators and developers of the OPTICO-ACS study, discovered a significant enrichment of CTLs ($p = 0.04$, 95% CI 0.01;0.26) and $CD4^+$ T-cells ($p = 0.01$, 95% CI 0.03;0.016) in erosional patients as compared to ruptured ACS patients via FACS analysis of PBMCs from the site of culprit plaque as depicted in **Figure 18** ⁶⁶. In addition, T-cell effector molecules granzysin ($p < 0.01$, 95% CI 0.29;1.50), perforin ($p = 0.02$, 95% CI 0.10; 1.08), and granzyme A ($p = 0.04$, 95% CI 0.02; 0.54) were also found to be at a significantly higher standardized difference within erosional patients, thereby foreshadowing a potential importance of CTLs and T-cells within the plaque erosion mechanism.

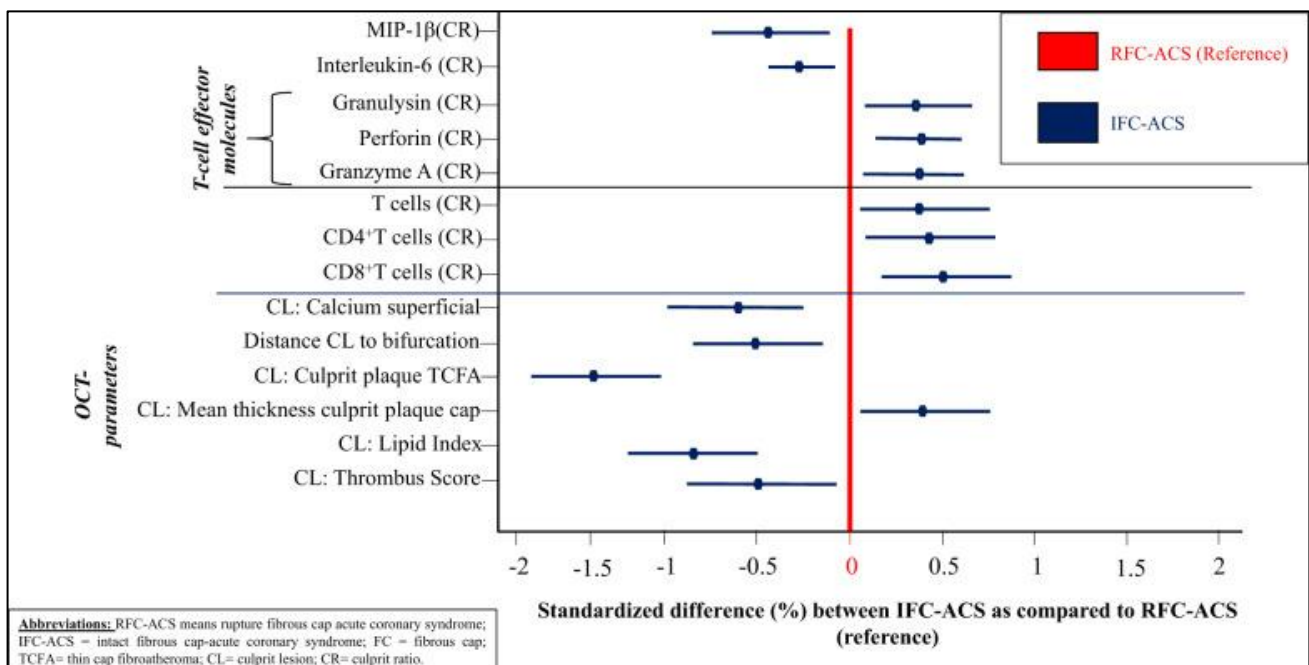


Figure 18: Results from OPTICO-ACS Study in 2020 ⁶⁶

4.2 Investigation Aim & Objectives

This dissertation's goal is to investigate the discrepancies between erosional and ruptured acute coronary syndromes via a multi-omics approach. The timing of this investigation is essential to furthering our comprehension of these two different pathomechanisms as new opportunities have granted themselves to confidently assign pathology with the aid of optical coherence tomography. In addition, the development of new multimodal techniques such as CITE-seq and single-cell TCR sequencing opens the door to investigating molecular mechanisms.

It is therefore clear that the next step in investigation is to further the resolution of immune archetypes of these ACS patients in hopes to find new outlooks to translational research. Therefore, this thesis aims to further elucidate the discrepancies in molecular mechanisms between erosional and ruptured myocardial infarction in patient isolated peripheral blood mononuclear cells (PBMCs) by combined use of CITE-seq and single cell TCR sequencing data to compare between amongst erosional, rupture, and with chronic coronary syndrome patients as a control group from acute pathology.

Objectives

1. To construct an integrated multimodal atlas as a CAD reference library.
2. To investigate the underlying molecular mechanisms involved in erosional and rupture plaques in coronary artery disease via a T-cell focused lens.
3. To identify potential biomarkers for preventative medications against erosional and rupture plaques in coronary artery disease.

MATERIALS & METHODS

Chapter 5. OPTICO-ACS Study: Patient Selection

5.1 The OPTICO-ACS Study

This dissertation works with a subset of the patient samples collected during the OPTICAL-COherence Tomography in Acute Coronary Syndrome (OPTICO-ACS) clinical trial as a follow-up investigation to further resolution in preliminary findings made by collaborators at the Charité University Berlin⁶⁶. The OPTICO-ACS study is an observational case-control study started April 28, 2017, under the Clinical Trials Identifier: *NCT03129505*. As seen in **Figure 19**, nearly 600 patients were recruited for the OPTICO-ACS study. After consideration of all study inclusion/exclusion criteria (**Table 1**), 398 ACS patients were remaining with completed follow-up (FU). From the total ACS population, 247 ruptured (62.1%) and 98 erosion (24.6%) patients were fully recruited⁶⁶.

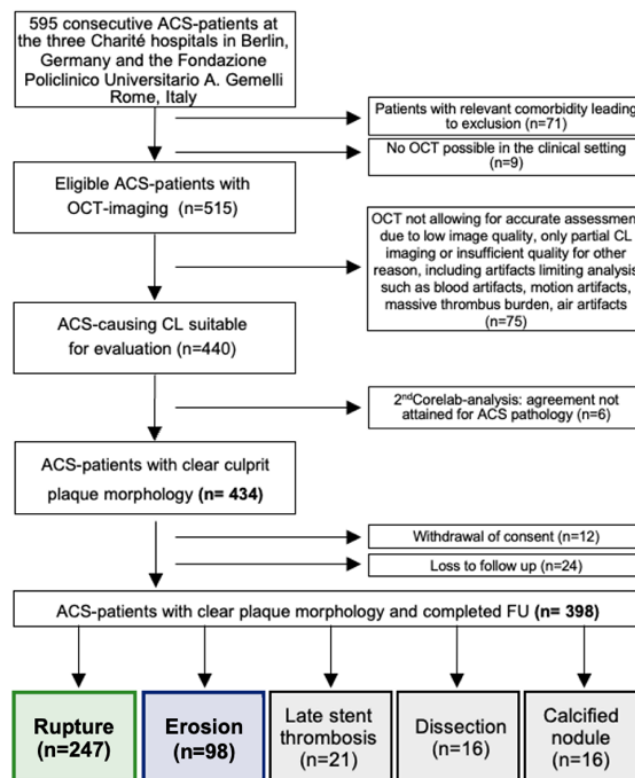


Figure 19: Patient recruitment from the OPTICO-ACS study⁶⁶

5.2 Patient Cohort Considerations

Patient sample size and cell yield aims were determined due to several factors such as available funding, wet lab processing time, and the number of lanes per single 10x chip. For single-cell sequencing, whole blood was obtained from 22 patients who underwent percutaneous coronary PCI as part of the OPTICO-ACS study.

Patients were matched for age, gender, and cardiovascular risk profile and met all study inclusion/exclusion criteria as seen in **Table 1**. The study was approved by the Medical Ethics Committee at Charité University Berlin (study approval numbers: EA4/021/15; EA1/270/16)⁶⁶. Upon enrollment, eligible patients underwent coronary angiography, followed by OCT imaging of the ACS-causing culprit lesion. All OCTs were analyzed for the underlying ACS-causing culprit pathophysiology by two independent core labs (Charité University Medicine, Berlin, and German Heart Center, Munich, Germany) using the Medis QIvus 3.0 (Medis Medical Imaging Service, Leiden, Netherlands), according to the standardized operating procedures⁶⁶.

Table 1: Study Inclusion/Exclusion Criteria⁶⁶

Inclusion Criteria	Exclusion Criteria
<ul style="list-style-type: none"> -ST segment myocardial infarction: Angina pectoris ≥ 20 minutes, withing 24 hours with one of the following ECG-signs: ST segment elevation ≥ 1 mm in neighboring ECG leads OR new left bundle branch block. - OR non ST segment elevation acute myocardial infarction: Angina pectoris ≥ 20 minutes, within 45 hours with one of the following: ST-segment depression ≥ 1 mm in ≥ 1 neighboring ECG leads - OR High sensitive Troponin T or I or CK/CK-MB above upper reference value - Age ≥ 18 years and ≤ 85 years - Suitability of the patient for the performance of the examinations in the opinion of the attending physician -Written informed consent -Patient must have coronary artery disease with an angiographically clearly identifiable culprit lesion 	<ul style="list-style-type: none"> -Active pregnancy, birth within the last 90 days, or while breastfeeding -Clinical evidence of active septicemia -Acute psychosis -Known systolic heart failure with Left ventricular ejection fraction (LVEF) ≤ 30% -Cardiogenic shock or circulatory depression with indication to intubation or therapy with positive inotropic drugs or mechanical circulatory support -Ventricular arrhythmias with indication for pharmacological or electrical therapy -Patients with organ transplants or patients on the waiting list for an organ transplant -Known chronic kidney disease with serum creatinine ≥ 1.5mg/dl -Patients with other chronic systemic diseases (active or non-curatively remediated tumor disease, chronic active inflammatory diseases) that require long-term therapy or are associated with an anticipated life expectancy of less than one year, or patients with active substance abuse -Stenosis of the left main artery ≥ 50 % -Acute coronary syndrome with the culprit lesion in a bypass vessel or caused by a stent/BVS thrombosis -Extent of coronary artery disease so advanced that bypass grafting will be necessary within the next year -Culprit lesion is not suitable for imaging by optical coherence tomography -Severe calcification or extreme vessel tortuosity -Culprit lesion in a very distal location -Infarcted vessel with a diameter > 4 mm or < 2.5 mm - In ST segment elevation myocardial infarction “no-reflow” (TIMI 0-1) after thrombus aspiration or pre-dilatation

BVS= Biovascular scaffold, ECG = Electrocardiogram, LVEF = Left ventricular ejection fraction, TIMI = Thrombolysis in Myocardial Infarction Score.

Chapter 6. Patient Sample Processing to Sequencing

6.1 Whole Blood Processing

The blood collection and processing methods of the OPTICO-ACS study, as seen in **Figure 20**, involved distinct approaches for ACS patients and control participants ⁶⁶. For patients with ACS, immediately after diagnostic angiography but preceding OCT imaging and PCI, coronary arterial blood samples were directly aspirated from the culprit lesion responsible for the ACS. CCS or control samples were gathered post-diagnostic angiography, just prior to PCI, through the arterial sheath (right radial artery: n=155/91%; femoral artery: n=25/9%) ⁶⁶. The method employed for aspiration of all samples involved the Export Advance aspiration catheter system (Medtronic, Minneapolis, MN, USA) ⁶⁶. Post-aspiration, all samples were immediately coated with Ethylenediamine tetraacetic acid (EDTA) and filtered to remove thrombotic components.

6.2 Isolation & Storage

Samples were immediately transferred to an in-house laboratory, supplemented with anticoagulant and filtered through a 40 µm CellTrics cell strainer within a maximum of 60 minutes after acquisition (Sysmex, 04-004-2327). PBMCs were isolated from whole blood by continuous density gradient centrifugation as per Ficoll guidelines ⁹⁹. For this process, blood was diluted at a 5:4 ratio with phosphate-buffered saline (PBS) and 2 mM EDTA and carefully layered on Ficoll-Paque at a 2:1 ratio (Cytiva, 17-1440-03). Samples were centrifuged for 30 minutes at 500 relative centrifugal force (RFC) while maintained at a 20°C temperature.

According to their specific density, during density centrifugation, PBMCs are retained between the Ficoll-solution and the plasma and can be visually identified and collected. Isolated PBMCs were washed twice in PBS at room temperature, counted and resuspended at 1×10^6 PBMCs/mL in freezing medium. The freezing medium consisted of Roswell Park Memorial Institute (RPMI) 1640 + 10% cold fetal bovine serum (FBS) with 10% Dimethyl sulfoxide (DMSO) (Thermo Fisher Scientific, 12633012, 16000044, D12345). Aliquots were gradually cooled in a Mr. Frosty freezing container over 24 hours and then transferred into liquid nitrogen at Charité University Medicine Berlin, Campus Benjamin-Franklin, Berlin Germany until further use (ThermoFisher Scientific, 5100-0001). The experimental setup from blood aspiration to end of wet lab for single cell processing may be seen below in **Figure 20**.

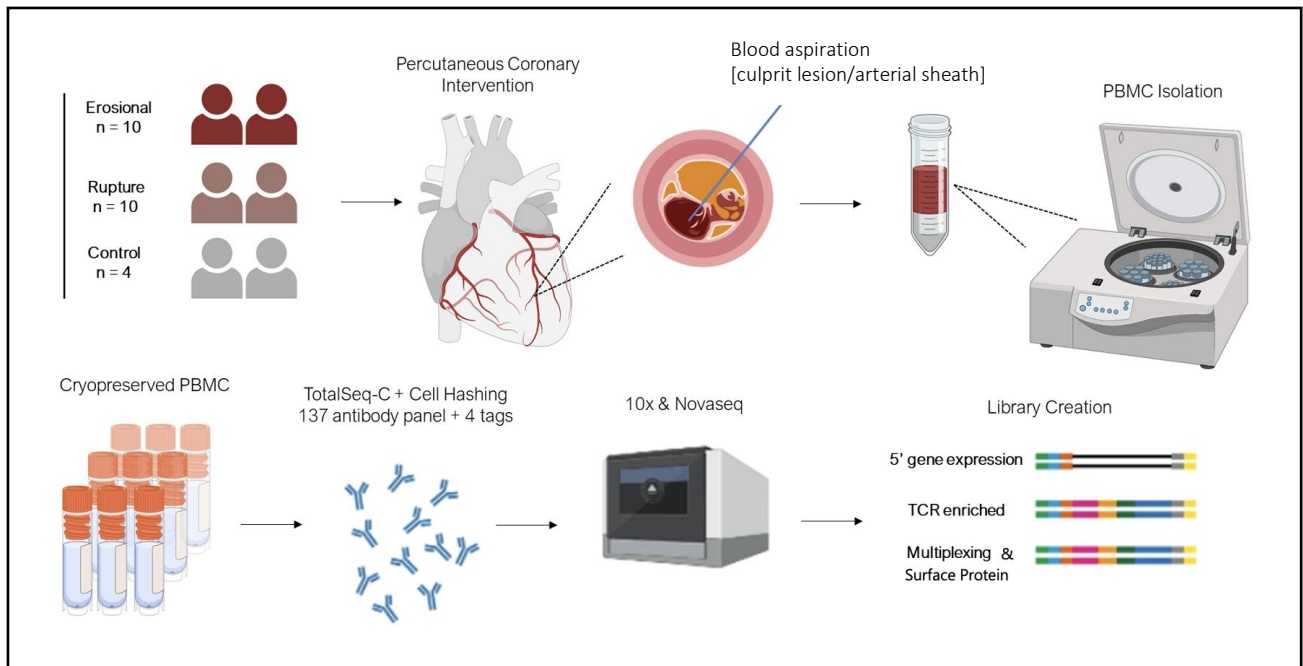


Figure 20: Experimental Setup from Aspiration to Library Creation

6.3 Cell Surface Staining & Cell Hashing

The cell surface staining workflow was performed based on the BioLegend protocol for TotalSeq-C while adding the hashtag staining in at the same antibody incubation time⁹⁶. All experiments were performed in low protein binding plastic ware. For profiling of cell surface protein, the commercial 137-target TotalSeq-C Human Universal Cocktail V1.0 (BioLegend, 399905), containing antibody-derived tags for 130 different cell surface antigens and seven isotype controls (**Table 3**).

TotalSeq-C hashtag antibody numbers 0251-025 were used for multiplexing (**Table 2**). Lyophilized cell surface and cell hashing reagents were reconstituted and Master Mixtures prepared according to the BioLegend's instructions¹⁰¹. To minimize cell apoptosis and ensure samples were sequenced within 6 hours of thawing. Experiments were spread out over three days and divided into mixed disease subsets to minimize batch effects. Day 1 was a pilot experiment and thus, after reconsideration, the amount of patient pooling was changed from 4 patients to 3 patients for the following experimental days to make workload simplified. PBMCs were thawed immediately after removal from liquid nitrogen by agitation in a 37°C water bath. Samples were washed three times using a pre-warmed Cell Staining Buffer (BioLegend, 420201), counted, and assessed for viability by trypan blue staining on cell counting chamber slides. In case of a viability <80%, the patient sample was removed from the single-cell pipeline and replaced to ensure high sample and data quality.

Cells were incubated with Human TruStain Fc (fragment crystallizable) Receptor Block Solution (BioLegend, 422301) for 10 minutes. Cells were then incubated with a master mixture containing the antibody panel and one specified hashtag for 30 minutes at 4 °C, washed three times and filtered through a 40 µm Flowmi cell strainer (Bel-Art SP Scienceware, H136800040). Cells were stained for viability using 7-Aminoactinomycin D (7-AAD) (ThermoFisher Scientific, A1310) and 50,000 viable cells

per sample were sorted on a BD FACS Aria Fusion cell sorter at the Cologne Center for Genomics (CCG) under the gating strategy seen in **Figure 21** below.

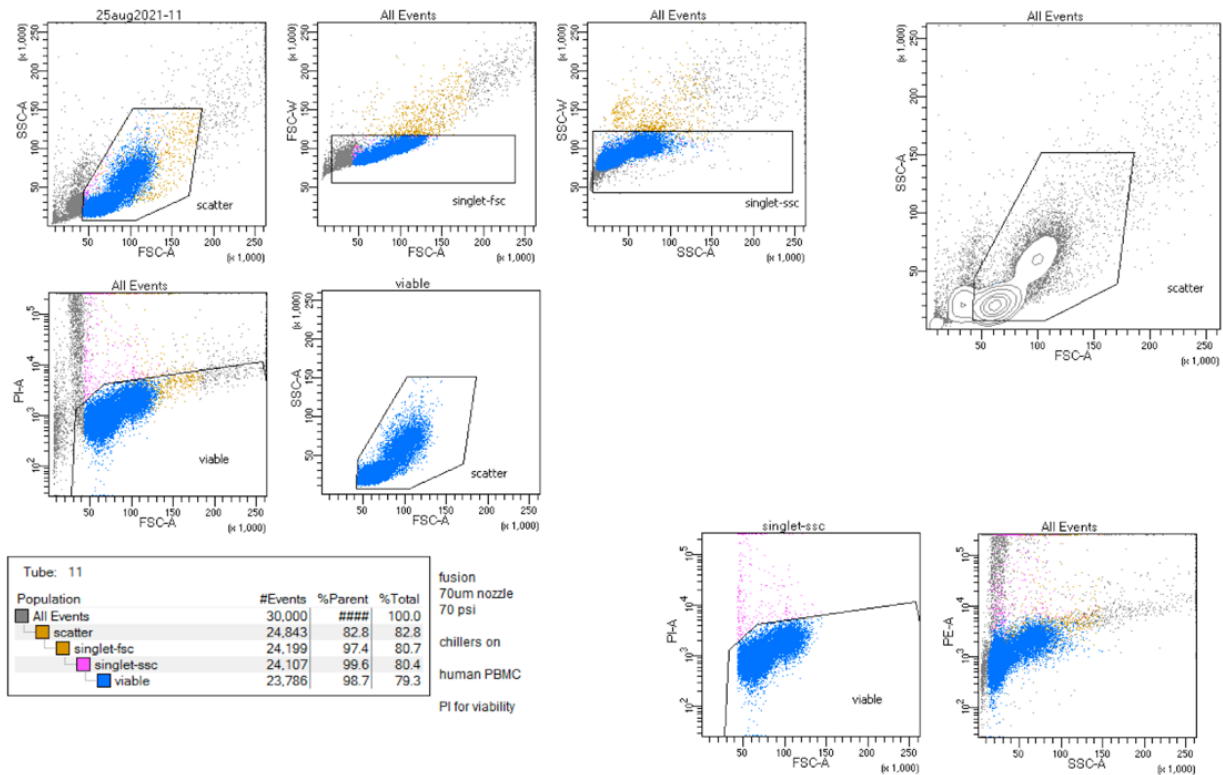


Figure 21: Cell Viability Gating Strategy for Sorting on BD FACS Aria

Table 2: Custom Whitelist for Demultiplexing via TotalSeq Hashtags

id,name,read,pattern,sequence,feature_type	Library Type	Catalog #
HTO_C0251,Name,R2,5PNNNNNNNNNN(BC),GTCAACTCTTTAGCG,Antibody	Capture	394661
HTO_C0252,Name,R2,5PNNNNNNNNNN(BC),TGATGGCCTATTGGG,Antibody	Capture	394663
HTO_C0253,Name,R2,5PNNNNNNNNNN(BC),TTCCGCCTCTCTTG,Antibody	Capture	394669
HTO_C0254,Name,R2,5PNNNNNNNNNN(BC),AGTAAGTTCAGCGTA,Antibody	Capture	394667

Table 3: Whitelist for TotalSeq-C Human Universal Cocktail ¹⁰⁰

DNA_ID	Description	Clone	Barcode	Gene name
C0944	anti-human CD101 (BB27)	BB27	CTACTTCCCTGTCAA	CD101
C0145	anti-human CD103 (Integrin α E)	Ber-ACT8	GACCTCATTGTGAAT	ITGAE
C0068	anti-human CD105	43A3	ATCGTCGAGAGCTAG	ENG
C0155	anti-human CD107a (LAMP-1)	H4A3	CAGCCCACCTGCAATA	LAMP1
C0024	anti-human CD112 (Nectin-2)	TX31	AACCTTCCGTCTAAG	NECTIN2
C0219	anti-human CD119 (IFN- γ R α chain)	GIR-208	TGTGTATTCCCTTGT	IFNGR1
C0185	anti-human CD11a	TS2/4	TATATCCTTGTGAGC	ITGAL
C0161	anti-human CD11b	ICRF44	GACAAGTGATCTGCA	ITGAM
C0053	anti-human CD11c	S-HCL-3	TACGCCTATAACTTG	ITGAX
C0246	anti-human CD122 (IL-2R β)	TU27	TCATTTCCCTCCGATT	IL2RB
C0064	anti-human CD123	6H6	CTTCACTCTGTCAGG	IL3RA
C0363	anti-human CD124 (IL-4R α)	G077F6	CCGTCCTGATAGATG	IL4R
C0390	anti-human CD127 (IL-7R α)	A019D5	GTGTGTTGTCCCTATG	IL7R
C0364	anti-human CD13	WM15	TTTCAACGCCCTTTC	ANPEP
C0158	anti-human CD134 (OX40)	Ber-ACT35 (ACT35)	AACCCACCGTTGTTA	TNFRSF4
C0355	anti-human CD137 (4-1BB)	4B4-1	CAGTAAGTTCGGGAC	TNFRSF9
C0081	anti-human CD14	M5E2	TCTCAGACCTCCGTA	CD14
C0163	anti-human CD141 (Thrombomodulin)	M80	GGATAACCGCGCTTT	THBD
C0134	anti-human CD146	P1H12	CCTTGGATAACATCA	MCAM
C0151	anti-human CD152 (CTLA-4)	BNI3	ATGGTTCACGTAATC	CTLA4
C0032	anti-human CD154	24-31	GCTAGATAGATGCAA	CD40LG
C0023	anti-human CD155 (PVR)	SKII.4	ATCACATCGTTGCCA	PVR
C0420	anti-human CD158 (KIR2DL1/S1/S3/S5)	HP-MA4	TATCAACCAACGCTT	KIR2DL1
C0592	anti-human CD158b (KIR2DL2/L3)	DX27	GACCCGTAGTTTGAT	KIR2DL3
C0599	anti-human CD158e1 (KIR3DL1, NKB1)	DX9	GGACGCTTTCCTTGA	KIR3DL1
C0083	anti-human CD16	3G8	AAGTTCACCTTTGTC	FCGR3A
C0149	anti-human CD161	HP-3G10	GTACGCAGTCCTTCT	KLRB1
C0358	anti-human CD163	GHI/61	GCTTCTCCTTCCTTA	CD163
C0206	anti-human CD169 (Siglec-1)	7-239	TACTCAGCGTGTGTTG	SIGLEC1
C0385	anti-human CD18	TS1/18	TATTGGGACACTTCT	ITGB2
C0140	anti-human CD183 (CXCR3)	G025H7	GCGATGGTAGATTAT	CXCR3
C0144	anti-human CD185 (CXCR5)	J252D4	AATTCAACCGTCGCC	CXCR5
C0050	anti-human CD19	HIB19	CTGGGCAATTACTCG	CD19
C0071	anti-human CD194 (CCR4)	L291H4	AGCTTACCTGCACGA	CCR4
C0141	anti-human CD195 (CCR5)	J418F1	CCAAAGTAAGAGCCA	CCR5
C0143	anti-human CD196 (CCR6)	G034E3	GATCCCTTTGTCACT	CCR6
C0160	anti-human CD1c	L161	GAGCTACTTCACTCG	CD1C
C0164	anti-human CD1d	51,1	TCGAGTCGCTTATCA	CD1D
C0367	anti-human CD2	TS1/8	TACGATTTGTCAGGG	CD2
C0100	anti-human CD20	2H7	TTCTGGGTCCCTAGA	MS4A1
C0181	anti-human CD21	Bu32	AACCTAGTAGTTCGG	CR2
C0393	anti-human CD22	S-HCL-1	GGGTTGTTGTCTTTG	CD22
C0152	anti-human CD223 (LAG-3)	11C3C65	CATTTGTCTGCCGGT	LAG3
C1052	anti-human CD224	KF29	CTGATGAGATGTCAG	GGT1

DNA_ID	Description	Clone	Barcode	Gene name
C0368	anti-human CD226 (DNAM-1)	11A8	TCTCAGTGTGTTGTGG	CD226
C0897	anti-human CD23	EBVCS-5	TCTGTATAACCGTCT	FCER2
C0180	anti-human CD24	ML5	AGATTCCCTTCGTGTT	CD24
C0189	anti-human CD244 (2B4)	C1.7	TCGCTTGGATGGTAG	CD244
C0085	anti-human CD25	BC96	TTTGTCCGTGTACGCC	IL2RA
C0396	anti-human CD26	BA5b	GGTGGCTAGATAATG	DPP4
C0247	anti-human CD267 (TACI)	1A1	AGTGATGGAGCGAAC	TNFRSF13B
C0215	anti-human CD268 (BAFF-R)	11C1	CGAAGTCGATCCGTA	TNFRSF13C
C0154	anti-human CD27	O323	GCACTCCTGCATGTA	CD27
C0020	anti-human CD270 (HVEM, TR2)	122	TGATAGAAACAGACC	TNFRSF14
C0170	anti-human CD272 (BTLA)	MIH26	GTTATTGGACTAAGG	BTLA
C0007	anti-human CD274 (B7-H1, PD-L1)	29E.2A3	GTTGTCCGACAATAC	CD274
C0088	anti-human CD279 (PD-1)	EH12.2H7	ACAGCGCCGTATTTA	PDCD1
C0386	anti-human CD28	CD28.2	TGAGAACGACCCTAA	CD28
C0369	anti-human CD29	TS2/16	GTATTCCCTCAGTCA	ITGB1
C0034	anti-human CD3	UCHT1	CTCATTGTAACTCCT	CD3D
C0370	anti-human CD303 (BDCA-2)	201A	GAGATGTCCGAATTT	CLEC4C
C0124	anti-human CD31	WM59	ACCTTTATGCCACGG	PECAM1
C0165	anti-human CD314 (NKG2D)	1D11	CGTGTGTTGTTCCTCA	KLRK1
C0830	anti-human CD319 (CRACC)	162,1	AGTATGCCATGTCTT	SLAMF7
C0142	anti-human CD32	FUN-2	GCTTCCGAATTACCG	FCGR2A
C0902	anti-human CD328 (Siglec-7)	6-434	CTTAGCATTTCACTG	SIGLEC7
C0052	anti-human CD33	P67.6	TAACCTCAGGGCCTAT	CD33
C0101	anti-human CD335 (NKp46)	9E2	ACAATTTGAACAGCG	NCR1
C0167	anti-human CD35	E11	ACTTCCGTGATCTT	CR1
C0864	anti-human CD352 (NTB-A)	NT-7	AGTTTCCACTCAGGC	SLAMF6
C0407	anti-human CD36	5-271	TTCTTTGCCCTFGCCA	CD36
C0389	anti-human CD38	HIT2	TGTACCCGCTFGTGA	CD38
C0176	anti-human CD39	A1	TTACCTGGTATCCGT	ENTPD1
C0072	anti-human CD4	RPA-T4	TGTTCCCGCTCAACT	CD4
C0031	anti-human CD40	5C3	CTCAGATGGAGTATG	CD40
C0353	anti-human CD41	HIP8	ACGTTGTGGCCTTGT	ITGA2B
C0216	anti-human CD42b	HIP1	TCCTAGTACCGAAGT	GP1BB
C0391	anti-human CD45	HI30	TGCAATTACCCGGAT	PTPRC
C0063	anti-human CD45RA	HI100	TCAATCCTTCCGCTT	PTPRC
C0087	anti-human CD45RO	UCHL1	CTCCGAATCATGTTG	PTPRC
C0026	anti-human CD47	CC2C6	GCATTCTGTACCTA	CD47
C0029	anti-human CD48	BJ40	CTACGACGTAGAAGA	CD48
C0575	anti-human CD49a	TS2/7	ACTGATGGACTCAGA	ITGA1
C0371	anti-human CD49b	P1E6-C5	GCTTTCTTCAGTATG	ITGA2
C0576	anti-human CD49d	9F10	CCATTCAACTTCCGG	ITGA4
C0138	anti-human CD5	UCHT2	CATTAACGGGATGCC	CD5
C0033	anti-human CD52	HI186	CTTTGTACGAGCAA	CD52
C0217	anti-human CD54	HA58	CTGATAGACTTGAGT	ICAM1
C0047	anti-human CD56	5.1H11	TCCTTTCTTGATAGG	NCAM1
C0168	anti-human CD57 Recombinant	QA17A04	AACTCCCTATGGAGG	B3GAT1
C0174	anti-human CD58 (LFA-3)	TS2/9	GTTCCTATGGACGAC	CD58
C0147	anti-human CD62L	DREG-56	GTCCCTGCAACTTGA	SELL
C0218	anti-human CD62P (P-Selectin)	AK4	CCTTCCGTATCCCTT	SELP
C0162	anti-human CD64	10,1	AAGTATGCCCTACGA	FCGR1A
C0146	anti-human CD69	FN50	GTCTCTTGGCTTAAA	CD69
C0066	anti-human CD7	CD7-6B7	TGGATTCCCGGACTT	CD7
C0394	anti-human CD71	CY1G4	CCGTGTTCCCTATTA	TFRC
C0577	anti-human CD73 (Ecto-5'-nucleotidase)	AD2	CAGTTCCCTCAGTTCG	NT5E
C0187	anti-human CD79b (Igβ)	CB3-1	ATTCTTCAACCGAAG	CD79B
C0046	anti-human CD8	SK1	GCGCAACTTGATGAT	CD8A

DNA_ID	Description	Clone	Barcode	Gene name
C0373	anti-human CD81 (TAPA-1)	5A6	GTATCCTTCCTTGGC	CD81
C0920	anti-human CD82	ASL-24	TCCCACCTCCGCTTT	CD82
C0359	anti-human CD83	HB15e	CCACTCATTTCCGGT	CD83
C0896	anti-human CD85j (ILT2)	GHI/75	CCTTGTTGAGGCTATG	LILRB1
C0006	anti-human CD86	IT2.2	GTCTTTGTCTAGTGCA	CD86
C1046	anti-human CD88 (C5aR)	S5/1	GCCGCATGAGAAACA	C5AR1
C0867	anti-human CD94	DX22	CTTTCCGGTCTTACA	KLRD1
C0156	anti-human CD95 (Fas)	DX2	CCAGCTCATTAGAGC	FAS
C0845	anti-human CD99	3B2/TA8	ACCCGTCCCTAAGAA	CD99
C0853	anti-human CLEC12A	50C1	CATTAGAGTCTGCCA	CLEC12A
C0179	anti-human CX3CR1	K0124E1	AGTATCGTCTCTGGG	CX3CR1
C0352	anti-human FcεR1α	AER-37 (CRA-1)	CTCGTTTCCGTATCG	FCER1A
C0912	anti-human GPR56	CG4	GCCTAGTTTCCGTTT	ADGRG1
C0058	anti-human HLA-A,B,C	W6/32	TATGCGAGGCTTATC	HLA-A
C0159	anti-human HLA-DR	L243	AATAGCGAGCAAGTA	HLA-DRA
C0918	anti-human HLA-E	3D12	GAGTCGAGAAATCAT	HLA-E
C0894	anti-human Ig light chain κ	MHK-49	AGCTCAGCCAGTATG	IGKC
C0898	anti-human Ig light chain λ	MHL-38	CAGCCAGTAAGTCAC	
C0384	anti-human IgD	IA6-2	CAGTCTCCGTAGAGT	IGHD
C0136	anti-human IgM	MHM-88	TAGCGAGCCGTATA	IGHM
C0153	anti-human KLRG1 (MAFA)	SA231A2	CTTATTTCTCGCCT	KLRG1
C0591	anti-human LOX-1	15C4	ACCCTTTACCGAATA	OLR1
C0581	anti-human TCR Vα7.2	3C10	TACGAGCAGTATTCA	
C0582	anti-human TCR Vδ2	B6	TCAGTCAGATGGTAT	
C0224	anti-human TCR α/β	IP26	CGTAACGTAGAGCGA	
C0089	anti-human TIGIT (VSTM3)	A15153G	TTGCTTACCGCCAGA	TIGIT
C0070	anti-human/mouse CD49f	GoH3	TTCCGAGGATGATCT	ITGA6
C0214	anti-human/mouse integrin β7	FIB504	TCCTTGGATGTACCG	ITGB7
C0171	anti-human/mouse/rat CD278 (ICOS)	C398.4A	CGCGCACCCATTAAG	ICOS
C0073	anti-mouse/human CD44	IM7	TGGCTTCAGGTCTTA	CD44
C0241	Armenian Hamster IgG Isotype Ctrl	HTK888	CCTGTCATTAAGACT	
C0090	Mouse IgG1, κ isotype Ctrl	MOPC-21	GCCGGACGACATTAAG	
C0091	Mouse IgG2a, κ isotype Ctrl	MOPC-173	CTCCTACCTAAACTG	
C0092	Mouse IgG2b, κ isotype Ctrl	MPC-11	ATATGTATCACGCGA	
C0236	Rat IgG1, κ isotype Ctrl	RTK2071	ATCAGATGCCCTCAT	
C0238	Rat IgG2a, κ Isotype Ctrl	RTK2758	AAGTCAGGTTTCGTTT	
C0095	Rat IgG2b, κ Isotype Ctrl	RTK4530	GATTCTTGACGACCT	

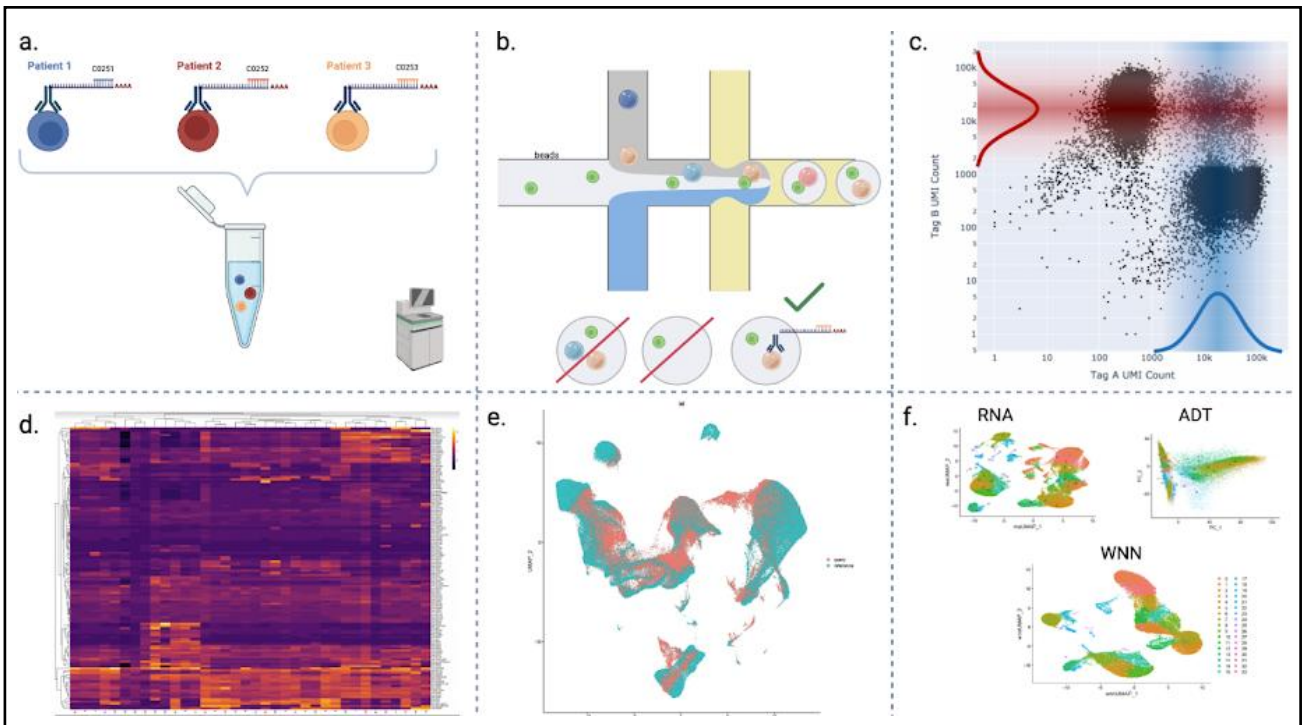


Figure 22: Methodological Outline from Sequencing to a Demultiplexed Multi-modal UMAP

As seen in **Figure 22**, the methodological outline from sequencing to a demultiplexed multi-modal UMAP is shown above **a**. Pooling of patient samples with unique oligonucleotide tags (C0251-C0253). **b**. sorting after sequencing which GEMs are containing only singlets: no doublets or empty GEMS. **c**. scattergram of centralized cell counts by unique oligonucleotide tag for demultiplexing cells with only one tag. **d**. Balancing of TotalSeq-C antibody panel using background antibody noise and isotype controls. **e**. Anchoring patient single-cell data with that of reference data of control patients via Azimuth. **f**. Weighted nearest neighbor stochastic merging of RNA and antibody data as seen in Hao et al., 2021⁹⁶.

6.4 Library Preparation & Sequencing

Single cell suspensions in 1X PBS containing 0,04% bovine serum albumin (BSA) (700-1200 nuclei/ μ L concentration) were checked for viability and processed with the Chromium Next GEM Single Cell 5' Kit v2 with dual indices together with the Single Cell V(D)J Reagent Kits v1.1 with Feature Barcode technology for Cell Surface Protein, and aiming for a target of 10,000 cells/sample at the CCG^{76,95}. Cells and the appropriate master mixture were loaded on a Chromium Next GEM Chip K and ran on the Chromium Controller to generate GEMs according to the manufacturer's' protocol after incubation (10x Genomics, PN-10000287). The GEMs were broken, and the pooled fractions were recovered. Silane magnetic beads were used to remove leftover biochemical reagents and primers from the post GEM reaction mixture. Full-length, barcoded cDNA was then amplified by PCR to generate sufficient mass for library construction. Library construction was performed, including End Repair, A-tailing, Adaptor Ligation and PCR. Similarly, for each sample pool a separate TCR library was

generated with aliquots from the amplified cDNA after V(D)J amplification ⁷⁶. Feature barcode DNA was amplified and used for the generation of the feature barcode library. The final libraries were quantified (Qubit) and pooled, and the pool was then quantified by using the Peqlab KAPA Library Quantification Kit and the Applied Biosystems 7900HT Sequence Detection System. Libraries were sequenced on an Illumina NovaSeq 6000 sequencing instrument with 29+89bp read length ^{76,95}.

Chapter 7. Bioinformatic Methodology

7.1 Cell Ranger Multi

After sequencing, data was transformed using Illumina’s *bcl2fastq* conversion software from binary base call (BCL) files to FASTQ files by the CCG ¹⁰¹. Following this data handover, *Cell Ranger Multi* v6.1.2 via 10x Genomics Cloud Analysis was incorporated to enable simultaneous profiling of the T-cell V(D)J repertoire (VDJ_T), ADT, antigen specificity, and gene expression (GEX) data ¹⁰². Thus, alignment, filtering, barcode counting, UMI counting on the Gene Expression and Feature Barcode libraries were performed via *Cellranger Multi*. Reads were mapped to the latest human reference genome, GRCh38 v5.0.0, which provides great improvements in artifact correction ¹⁰². The experimental design for the *Cell Ranger Multi* analysis was designed by patient pools, as shown in **Figure 23**.

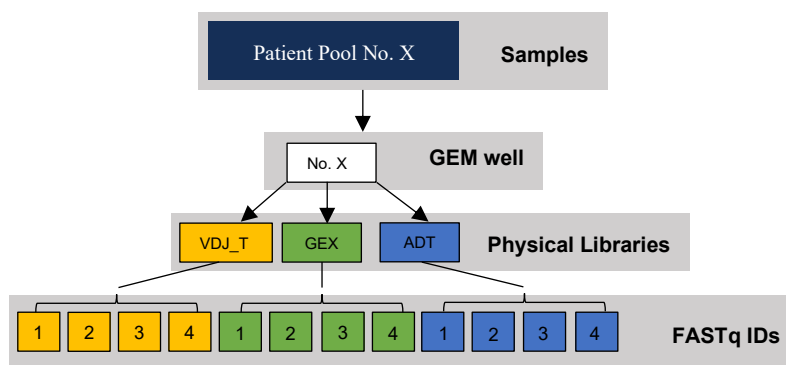


Figure 23: Experimental Design for *Cell Ranger Multi* Analysis by Pooled Patients

7.2 Gaussian-Mixture-Model-based Demultiplexing

Demultiplexing patient samples was employed using the Gaussian-Mixture-Model-based or *GMM-Demux* Python package. This package allows for the removal of sample multiplets or ‘phony’ cells in a cell hashing dataset and the separation of cells by specific hashing oligonucleotide sequences seen in **Table 2** ¹⁰³. As the experimental design for sequencing included both an oligonucleotide sequences for the TotalSeq-C panel as well as the Totalseq-C hashtag antibodies, *Cell Ranger Multi* was used for the patient pools in which *GMM-Demux* was then implemented to safely valid manually output results and manual cutoffs to ensure quality control as depicted in **Figure 24**.

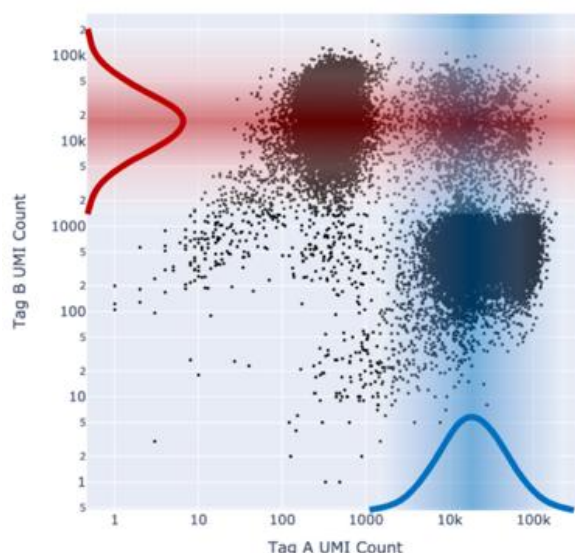


Figure 24: Quality Control Demultiplexing Histogram Example ⁷⁶

Once the validated cell ID lists were curated from *GMM-Demux* per patient, these cell ID barcodes were used to manually demultiplex TCR information as *Cell Ranger Multi* only fulfilled information by the pool and not by the patient ¹⁰³. The VDJ information was curated per pool. This manual TCR demultiplexing was conducted by matching the cell IDs from the *Cell Ranger Multi* for an entire pool to the validated patient by patient list from *GMM-Demux* via macro code in Excel and the major command of *VLOOKUP* or vertical lookup.

In the cases of no custom reverse transcription (RT) primer reactions, CITE-seq + Multiplexing combinational sequencing contains major technical limitation as seen in **Figure 25**. Presented in **Figure 25**, ADT, and hashtag oligo (HTO) libraries have a very similar size, approximately 180 base pairs, and therefore typically require custom RT primers when combining in one sequencing experiment ¹⁰⁴.

By manually instructing *Cell Ranger Multi* to interpret the HTO library as part of the ADT library in a custom whitelist (**Tables 2-3**), the expression signals of the HTO library are considered as an antibody expression in conjunction with the TotalSeq-C panel. This solution requires a more manual and thorough demultiplexing of the patient samples whereby *GMM-Demux* was employed to maximize the performance of singlet retrieval as seen in the histogram example of two tags and the identification of overlap noise (**Figure 24**). As depicted in **Figure 26**, this patient pool example of three patients held 80,306 'drops' and was demultiplexed by hashtags of **Table 2**. The result was a singlet confidence of 85.27%, in which was maximum histogram quality for this pool, and was demultiplexed into 5,849, 13,444, and 3,710 cells for hashtags C0251, C0252, and C0253, respectively.

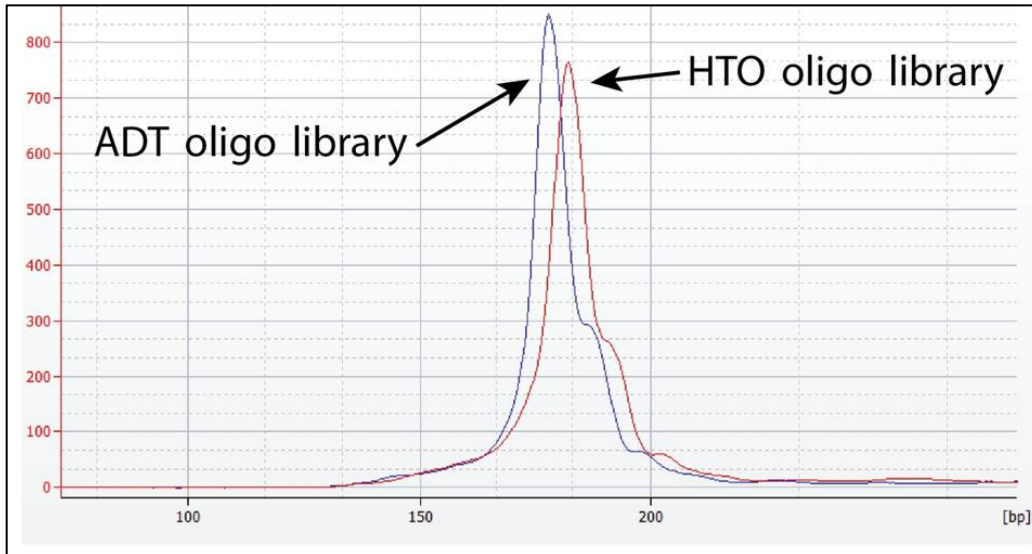


Figure 25: Technical Limitations for Multiple Oligonucleotide-tagged Libraries ¹⁰⁴

```

=====GMM-Demux Initialization=====
Confidence threshold: 0.8
Output directory: SSD_mtx
MSM-free droplets are stored in folder SSD_mtx

=====Full Report=====
+-----+-----+-----+-----+-----+-----+-----+-----+-----+
|      | #Drops | Capture rate | #Cells | Singlet | MSM | SSM | RSSM | Negative | Unclear |
+-----+-----+-----+-----+-----+-----+-----+-----+-----+
| Total | 80306 | 62.48 | 23003 | 85.27 | 9.1 | 5.64 | 6.61 | 1.39 | 2.02 |
+-----+-----+-----+-----+-----+-----+-----+-----+-----+

=====Per Sample Report=====
+-----+-----+-----+
|      | C0251 | C0252 | C0253 |
+-----+-----+-----+
| #Cells | 5849 | 13444 | 3710 |
| #SSDs | 2695 | 6941 | 1644 |
| RSSM | 3.6 | 8.14 | 2.29 |
+-----+-----+-----+

```

Figure 26: GMM-Demux Manual Patient Demultiplexing from Pool

7.3 Denoised & Scaled Antibody Expressions

The R package “Denoise and Scale by Background” or *DSB*, was employed to normalize and denoise droplet-based protein expression data via the usage of empty droplet matrixes and isotype control information ¹⁰⁵. Within the Cell Ranger pipeline exists raw feature barcode matrices, which

include information about the expression of empty GEMs before formatting. *DSB* utilizes this extra data by calculating the amount of unbound or “ambient” ADT expression encapsulated in the empty GEMs¹⁰⁵. With the additional ability to include single-cell level isotype control information, the data was normalized and denoise by sample-specific ambient ADT levels and as well as the seven isotype controls contained inside of the TotalSeq-C panel (**Table 3**). To eliminate the noise of the high antibody expression from demultiplexing methods, hashtag antibody (**Table 2**) expression was removed. In addition, as recommended for data containing multiple run days, quantile clipping was implemented such that the most extreme expressions of the panel were removed whereby *quantile.clip* = c(0.001, 0.995). *DSB* was first employed on a pool specific level for batching reasons and then again used to normalize all protein patient information together in replacement of centered log ratio transformation (CLR), which was the previous standard methodology for CITE-seq data⁹⁶. Finally, as seen below in **Figure 27**, all patients single cells expression of each antibody of the TotalSeq-C panel were quality controlled on a patient individual status and during merging.

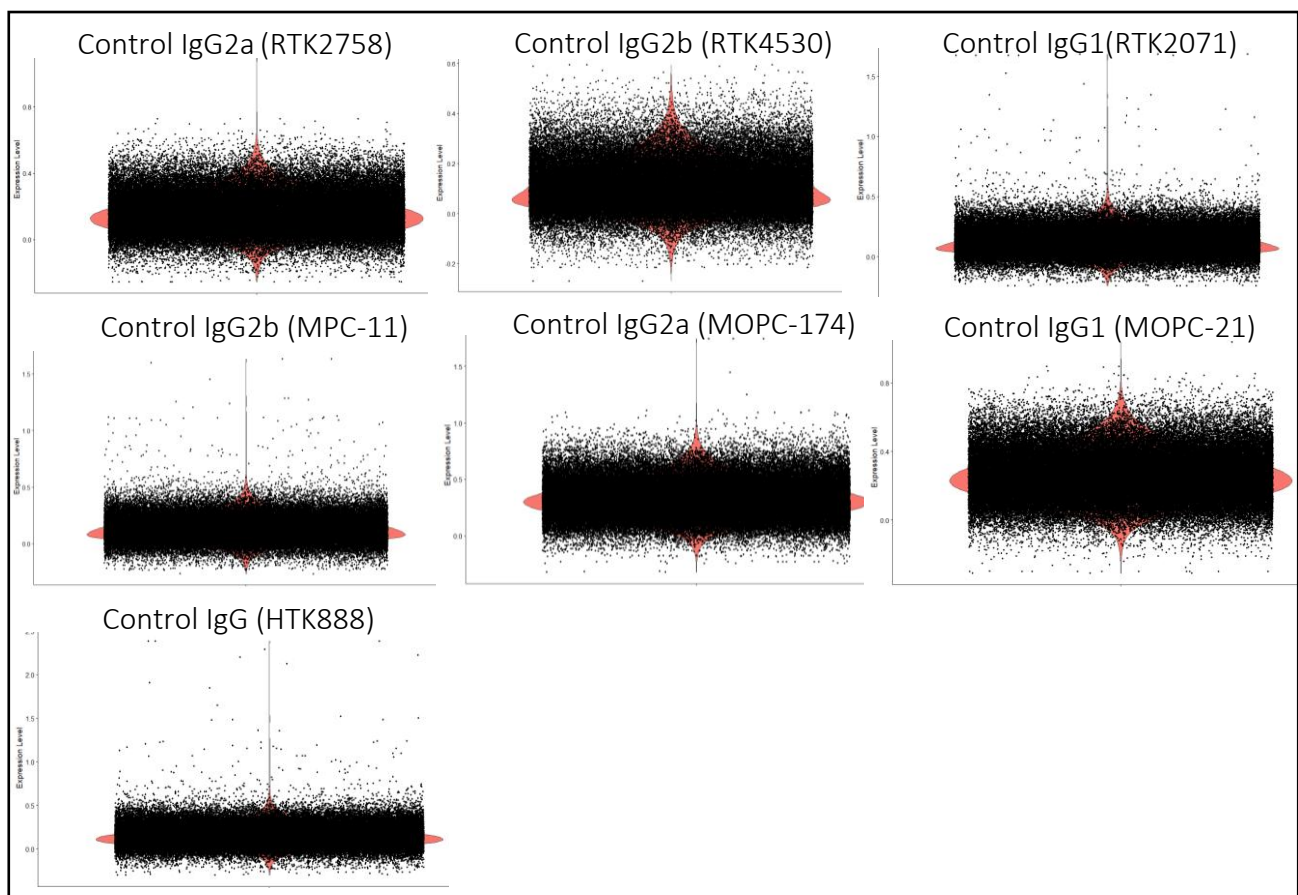


Figure 27: Final Isotype Control Distributions After Quality Control

7.4 Creation of a Multimodal Seurat File

All files were pre-processed individually while transcriptomic and protein epitope libraries were combined into one multimodal *Seurat* object per patient as seen in **Figure 28**. **Figure 28** shows the main code for *DSB* normalization (**sections 1-2**), integration between transcriptomic and protein epitope libraries (**section 3**), and meta-data assignment for differentiation between disease subsets

and patient individuality (**section 4**). This code was created as a loop for all patients to run for each patient automatically.

```

1 Object = colnames(Object$`Gene Expression`)
  background = setdiff(colnames(Raw.Pool.DSB$`Gene Expression`), Object)
  protein = Raw.Pool.DSB$`Antibody Capture`
  RNA = Raw.Pool.DSB$`Gene Expression`
  mtgene = grep(pattern = "^MT-", rownames(rna), value = T)

2 Object.adt.raw = Object.adt.raw[!rownames(Object.adt.raw) == 'Hashtags', ]
  background.adt.mtx = background.adt.mtx[!rownames(background.adt.mtx) == 'Hashtags', ]

  isotype.controls = c("Isotype_HTK888", "Isotype_MOPC.173",
    "Isotype_MOPC.21", "Isotype_MPC.11", "Isotype_RTK2071", "Isotype_RTK2758", "Isotype_RTK4530")
  Object.dsb.norm = DSBNormalizeProtein(
    cell_protein_matrix = Object.adt.raw,
    empty_drop_matrix = background.adt.mtx,
    denoise.counts = T,
    use.isotype.control = T,
    quantile.clipping = T,
    scale.factor = 'mean.subtract',
    quantile.clip = c(0.001, 0.9995),
    isotype.control.name.vec = isotype.controls)

3 Object.2 = Seurat::CreateSeuratObject(counts = Object.rna.raw, meta.data = Objectmd, assay =
  "RNA", min.cells = 20)
  Object.2[["CITE"]] = Seurat::CreateAssayObject(data = Object.dsb.norm)
  protein = rownames(Object.2@assays$CITE@data) [1:127]

4 DefaultAssay(Object.2) = "RNA"
  Object$Patients <- "Patient.ID"
  Object$Disease <- "Rupture"

```

Figure 28: Multimodal Integration of RNA and Protein Expression Data by Patient

In addition, T-cell receptor data was implemented into the previously created multimodal patient specific object via the R package *scRepertoire*¹⁰⁶. *ScRepertoire* allows for the integration of the ‘filtered_contig_annotiations’ output file from *Cell Ranger Multi* to a *Seurat* object. The ‘filtered_contig_annotiations’ output file houses critical information on single cell ID, clonal expansion, as well as other important genetic information of the TCR itself such as α and β -chain nucleotide sequences. This method allowed for full integration at the single cell resolution of the previously curated CITE-seq *Seurat* object into a CITEseq+TCR *Seurat* object.

Due to the process of separated library creation, the indexing of the single cell barcodes of both libraries was slightly different and therefore the command ‘*stripBarcode*’ was employed to remove non-critical meta-data¹⁰⁶. Binning of clonal expansion information was created as per the recommendation of *ScRepertoire* for analytic purposes as clonotype binning is used to understand the relative space occupied by clones at specific proportions¹⁰⁶. **Figure 29** below shows the cutoffs for

binning into different clonotype categories. The hyperexpanded bin, for example, may reach between 10% and 100% of a patients TCR repertoire.

	Range	Percentile Range
Rare	0-1e - 04	0 - 0.01%
Small	1e-04 - 0.001	0.01 - 0.1%
Medium	0.001 - 0.01	0.1 - 1%
Large	0.01 - 0.1	1 - 10%
Hyperexpanded	0.1 - 1	10 - 100%

Figure 29: Clonotype Binning as Recommended by *ScRepertoire* ¹⁰⁶

7.5 Merging Seurat Objects, Pre-Processing, and Weight nearest neighbor analysis

Individual patient multimodal *Seurat* objects were then merged and pre-processed of unwanted cellular events with a range fit of genes between 500 and 4000 and a percentage of mitochondrial (MT) genes <8% as seen in the violin plots of **Figure 30** ⁹⁶. *Seurat's FindNeighbors* and *FindClusters* were employed ⁹⁶. Cluster determination employed a Smart Local Moving (SLM) algorithm as opposed to Louvain clustering to optimize large network community detection ¹⁰⁷. The protein expression of the merged multimodal *Seurat* object was normalized again using *DSB* normalization as per package recommendations ¹⁰⁵. Transcriptomic and protein epitope libraries were combined into one multimodal *Seurat* object with *Seurat* v4 and per WNN analysis guidelines ⁹⁶.

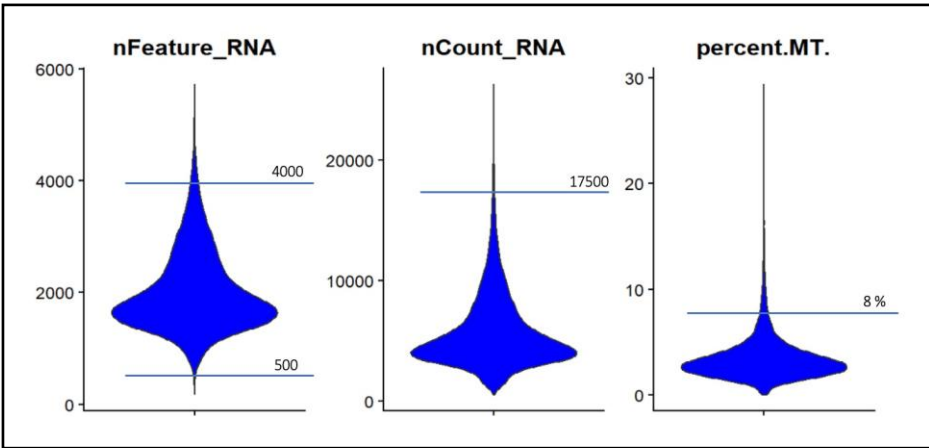


Figure 30: Quality Control of Gene Expression Distributions

7.6 The App for Reference-Based Single-Cell Analysis: *Azimuth*

As part of the Human BioMolecular Atlas Program (HuBMAP), the *Azimuth* software was used for the reference-based mapping of the WNN CITEseq+TCR *Seurat* object. *Azimuth* uses the RNA expression of the data to be mapped input. The Human PBMC reference library, which is a part of the

Azimuth software, consists of 8 healthy volunteers enrolled in an HIV vaccine trial, in whose PBMCs were sequencing with the Biolegend TotatSeq-A panel⁹⁶. Annotation of the WNN CITEseq+TCR *Seurat* object was performed via Query-Reference Mapping with the Human-PBMC reference dataset⁹⁶. The intermediate level of resolution from the *Azimuth* software, named Celltype.l2 was used to for the annotation. Below in **Table 4**, the markers used for cell assignment algorithm for Celltype.l2 may be seen.

Table 4: PBMC Reference Dataset Annotation Details for Celltype.l2⁹⁶

Label	Transcriptomic Markers
Mature B cell	MS4A1, TNFSF13B, IGHM, IGHD, AIM2, CD79A, LINC01857, RALGPS2, BANK1, CD79B
Memory B cell	MS4A1, COCH, AIM2, BANK1, SSPN, CD79A, TEX9, RALGPS2, TNFRSF13C, LINC01781
Naïve B cell	IGHM, IGHD, CD79A, IL4R, MS4A1, CXCR4, BTG1, TCL1A, CD79B, TBX3
Plasmablast	IGHA2, MZB1, TNFRSF17, DERL3, TXNDC5, TNFRSF13B, POU2AF1, CPNE5, HRASLS2, NT5DC2
CD4 ⁺ CTL	GZMH, CD4, FGFBP2, ITGB1, GZMA, CST7, GNLY, B2M, IL32, NKG7
CD4 ⁺ Naïve	TCF7, CD4, CCR7, IL7R, FHIT, LEF1, MAL, NOSIP, LDHB, PIK3IP1
CD4 ⁺ Proliferating	MKI67, TOP2A, PCLAF, CENPF, TYMS, NUSAP1, ASPM, PTTG1, TPX2, RRM2
CD4 ⁺ T _{CM}	IL7R, TMSB10, CD4, ITGB1, LTB, TRAC, AQP3, LDHB, IL32, MAL
Treg	RTKN2, FOXP3, AC133644.2, CD4, IL2RA, TIGIT, CTLA4, FCRL3, LAIR2, IKZF2
CD8 ⁺ Naïve	CD8B, S100B, CCR7, RGS10, NOSIP, LINC02446, LEF1, CRTAM, CD8A, OXNAD1
CD8 ⁺ Proliferating	MKI67, CD8B, TYMS, TRAC, PCLAF, CD3D, CLSPN, CD3G, TK1, RRM2
CD8 ⁺ T _{CM}	CD8B, ANXA1, CD8A, KRT1, LINC02446, YBX3, IL7R, TRAC, NELL2, LDHB
CD8 ⁺ T _{EM}	CCL5, GZMH, CD8A, TRAC, KLRD1, NKG7, GZMK, CST7, CD8B, TRGC2
AXL ⁺ DC	PPP1R14A, LILRA4, AXL, IL3RA, SCT, SCN9A, LGMN, DNASE1L3, CLEC4C, GAS6
CD141 ⁺ DC	CLEC9A, DNASE1L3, C1orf54, IDO1, CLNK, CADM1, FLT3, ENPP1, XCR1, NDRG2
CD1c ⁺ DC	FCER1A, HLA-DQA1, CLEC10A, CD1C, ENHO, PLD4, GSN, SLC38A1, NDRG2, AFF3
CD14 ⁺ Mono	S100A9, CTSS, S100A8, LYZ, VCAN, S100A12, IL1B, CD14, GOS2, FCN1
CD16 ⁺ Mono	CDKN1C, FCGR3A, PTPRC, LST1, IER5, MS4A7, RHOC, IFITM3, AIF1, HES4
NK CD56 ^{dim}	GNLY, TYROBP, NKG7, FCER1G, GZMB, TRDC, PRF1, FGFBP2, SPON2, KLRF1
NK Proliferating	MKI67, KLRF1, TYMS, TRDC, TOP2A, FCER1G, PCLAF, CD247, CLSPN, ASPM
NK CD56 ^{Bright}	XCL2, FCER1G, SPINK2, TRDC, KLRC1, XCL1, SPTSSB, PPP1R9A, NCAM1, TNFRSF11A
Eryth	HBD, HBM, AHSP, ALAS2, CA1, SLC4A1, IFIT1B, TRIM58, SELENBP1, TMCC2
HSPC	SPINK2, PRSS57, CYTL1, EGFL7, GATA2, CD34, SMIM24, AVP, MYB, LAPTM4B
ILC	KIT, TRDC, TTLL10, LINC01229, SOX4, KLRB1, TNFRSF18, TNFRSF4, IL1R1, HPGDS
Platelet	PPBP, PF4, NRGN, GNG11, CAVIN2, TUBB1, CLU, HIST1H2AC, RGS18, GP9
DN T	PTPN3, MIR4422HG, NUCB2, CAV1, DTHD1, GZMA, MYB, FXYD2, GZMK, AC004585.1
γδT	TRDC, TRGC1, TRGC2, KLRC1, NKG7, TRDV2, CD7, TRGV9, KLRD1, KLRG1
MAIT	KLRB1, NKG7, GZMK, IL7R, SLC4A10, GZMA, CXCR6, PRSS35, RBM24, NCR3

7.7 Re-clustering T-cell Specific Subset & Annotations

For the re-clustering to a T-cell subset, the R package *SingleR* v3.17 was employed¹⁰⁸. *SingleR* is a type of cell type annotation software, like *Azimuth*, with more reference libraries. To re-cluster the atlas to allow for further T-cell resolution, *Azimuth* prediction scores were employed such that any

cells not assigned as CD4⁺ T-cells, CD8⁺ T-cells, or 'other' T-cells with a score of confidence $\geq 80\%$ by the *Azimuth* algorithm were removed for further processing. These barcodes were then kept as a list and used to subset the main merged Seurat object pre-normalization and clustering to allow create a T-cell specific multimodal UMAP structure, following the same methods described previously for the ACS atlas, however, instead of employing *Azimuth again*, the package *SingleR* was utilized in combination with the reference library by list format via the *scater* R package ^{108,109}.

For every individual cell within the experimental dataset, *SingleR* was employed to compute a similarity score as is similar with the *Azimuth* software. This score quantifies how closely the gene expression profile of each cell matches the average gene expression profile of known cell types or states from our selected reference dataset. *SingleR* assesses the resemblance between each cell in our dataset and the reference cell types. This process involves a combination of cosine similarity and Pearson correlation relationship to employ a similarity index between gene expression profiles, thereby aiding in identify the most likely cell type or state for each cell in the dataset ¹⁰⁸. The chosen reference library was selected from the popular library package *celldex*, specifically the reference library from Monaco et al., in which specifically focuses primarily on T-cells ^{110, 111}.

As *SingleR* was constructed for the package *SingleCellExperiment* (*sce*) formatted single cell data, data from the Seurat object was attempted to be converted to a *sce* object and then re-converted using the *as.Seurat* function ¹¹². Due to an interoperability failure between *Seurat* v5 and *SingleCellExperiment* v3.17, conversion back into a *Seurat* object was not possible. Therefore, the metadata curated from *SingleR* as an *sce* object was then saved and assigned to the original *Seurat* object via the *AddMetaData* function.

Following the *SingleR* analysis, cell types were assigned to each cell based on the computed similarity scores. The cell type assignment was straightforward: assignment of each cell was determined from the reference dataset with the highest similarity score. This approach effectively allowed for annotation and categorizing of the individual cells within the dataset. The resulting cell type annotations formed a higher T-cell resolution than previously with the *Azimuth* package.

RESULTS

Chapter 8. Constructing an Integrated Multimodal Atlas

8.1 Patient Characteristics

Table 5: Individual Patient Characteristics

ID	Age	Type	Diagnosis	Gender
Con25	55	Control	Stable CAD	Male
Con19	60	Control	Stable CAD	Male
Con23	44	Control	Stable CAD	Male
Con3	71	Control	Stable CAD	Male
3381	54	Erosion	NSTEMI	Female
3367	50	Erosion	NSTEMI	Female
3424	51	Erosion	STEMI	Male
3427	54	Erosion	STEMI	Male
3402	58	Erosion	NSTEMI	Male
3359	49	Erosion	STEMI	Male
3395	61	Erosion	NSTEMI	Male
380	79	Erosion	NSTEMI	Male
3360	68	Rupture	NSTEMI	Female
3422	68	Rupture	STEMI	Female
3369	68	Rupture	STEMI	Male
3361	83	Rupture	STEMI	Male
3408	57	Rupture	NSTEMI	Male
3403	66	Rupture	STEMI	Male
3409	43	Rupture	STEMI	Male
3428	60	Rupture	STEMI	Male
3413	75	Rupture	STEMI	Male
3357	62	Rupture	STEMI	Male

As presented in Table 5 above, the selected patients from the Optico-ACS cohort consisted of 22 patients, 18 males and 4 females, aged 44-83 years old with a median of 60 years of age. After all inclusion/exclusion criteria as presented in the methods, this cohort for single-cell sequencing consisted of four patients of stable CAD or ‘controls’, eight patients of erosional ACS, and ten patients of ruptured ACS. When comparing between these erosional vs. ruptured ACS patients’ clinical information (that physicians would have on file of these patients or gained directly at admission to the hospital), only creatine kinase (CK) was indicative of a significantly different (p -value=0.043) as seen in Figure 6 below.

Table 6: Baseline Characteristics

Patient Characteristics	All patients (n=18)	Erosion (n=8)	Rupture (n=10)	p-value*
Age, years \pm SD	61.5 \pm 10.8	57.0 \pm 9.8	65.1 \pm 10.6	0.057
CAD Family History, n (%)	5 (28%)	2 (25%)	3 (30%)	0.814
Smoking, n (%)	12 (67%)	7 (88%)	5(50%)	0.094
Diabetes mellitus, n (%)	1 (6%)	0 (0%)	1 (10%)	0.357
Arterial hypertension, n (%)	10 (56%)	4 (50%)	6 (60%)	0.671
Dyslipidemia, n (%)	13 (72%)	6 (75%)	7 (70%)	0.814
Previous History of PCI, n (%)	0 (0%)	0 (0%)	0 (0%)	n.a.
ACS characteristics				
Presentation as STE-ACS, n (%)	11 (61%)	3 (38%)	8 (80%)	0.066

CK peak, U/l (mean ± SD)	1417.9 ± 1429.6	595.3 ± 649.9	1993.7 ± 1567.6	0.043
LV-EF at discharge, % (mean ± SD)	57.9 ± 8.6	56.6 ± 8.4	58.9 ± 9.0	0.780
Coronary Angiographic Data				
Single-vessel disease, n (%)	11 (61%)	6 (75%)	5 (50%)	0.234
Two-vessel disease, n (%)	3 (17%)	0 (0%)	3 (30%)	
Three-vessel disease, n (%)	4 (22%)	2 (25%)	2 (20%)	
Laboratory data**				
Total cholesterol (mg/l; mean ± SD)	213.9 ± 36.2	194.5 ± 33.3	222.6 ± 35.8	0.348
LDL cholesterol (mg/l; mean ± SD)	143.1 ± 39.8	123.8 ± 34.8	158.6 ± 38.1	0.057
HDL cholesterol (mg/l; mean ± SD)	51.6 ± 19.2	48.3 ± 21.0	54.2 ± 18.6	0.519
Serum creatinine (mg/l; mean ± SD)	1.0 ± 0.1	1.0 ± 0.2	1.0 ± 0.1	0.633
Hemoglobin (g/dl)	14.6 ± 1.2	14.2 ± 1.5	14.9 ± 0.68	0.370
Leukocytes (per ml)	10.8 ± 2.1	9.9 ± 2.0	11.4 ± 2.0	0.27
hs-CRP (mg/l; mean ± SD)	2.5 ± 4.5	3.5 ± 6.5	1.7 ± 1.9	0.999
Medication prior to hospitalization				
ASS	0 (0%)	0 (0%)	0 (0%)	n.a.
Clopidogrel	0 (0%)	0 (0%)	0 (0%)	n.a.
Prasugrel	0 (0%)	0 (0%)	0 (0%)	n.a.
Ticagrelor	0 (0%)	0 (0%)	0 (0%)	n.a.
Warfarin	0 (0%)	0 (0%)	0 (0%)	n.a.
NOACs	1 (6%)	1 (13%)	0 (0%)	0.274
β-Blocker	1 (6%)	0 (0%)	1 (10%)	0.331
ACE-Inhibitors/AT-II-Blocker	2 (12%)	1 (13%)	1 (10%)	0.929
Diuretics	1 (6%)	1 (13%)	0 (0%)	0.274
Aldosterone antagonists	0 (0%)	0 (0%)	0 (0%)	n.a.
Digitalis	0 (0%)	0 (0%)	0 (0%)	n.a.
Calcium inhibitors	1 (6%)	1 (13%)	0 (0%)	0.274
Nitrates	0 (0%)	0 (0%)	0 (0%)	n.a.
Inhalation anti-obstructive therapy	0 (0%)	0 (0%)	0 (0%)	n.a.
Oral steroid therapy	0 (0%)	0 (0%)	0 (0%)	n.a.
Statins	0 (0%)	0 (0%)	0 (0%)	n.a.
Ezetemibe	0 (0%)	0 (0%)	0 (0%)	n.a.

Values of continuous variables expressed as mean ± standard deviation.

* p-values determined between erosion and rupture ACS.

** measured at admission to hospital.

ACE-Inhibitor = Angiotensin-converting enzyme inhibitor, ASS= Acetylsalicylic Acid, AT-II-Blocker = Angiotensin II receptor blocker, BMI = body mass index, HDL = high density lipoprotein, hsCRP = high sensitive C-reactive protein, LDL = low density lipoprotein, n= number, n.a. = not applicable, NOAC= Non-Vitamin K antagonist Oral Anti-Coagulant, SD = standard deviation.

8.2 Wet Lab Organizational Output

As mentioned in methods, patients were pooled based on three or four oligonucleotide hashtags depending on the run day as seen in **Table 7** below. In addition, the received viability after wet lab thawing and total cells are reported. The entire sequencing experiments over three run days successfully sequenced eight pools and 24 samples among the 22 patients reported in **Table 5**. In addition, the reports of viability and total cells after sorting, as well as total cells sequenced directly from the NovaSeq-6000 system, may also be seen below.

To note, erosional patient 3381 has a complimentary sample from the peripheral blood in addition to comparing against the patients' coronary arterial blood sample taken during PCI. In addition, ruptured patient 3360 was successfully sequenced twice, due to the chance of being successfully sequenced twice as 34 samples failed at some point during cold chain shipment, thawing, sorting, or sequencing. This creates a total number of 24 samples.

Table 7: Sampling Pooling, Cell Viability Measurements, and RNA Sequencing Yield

ID	Sample Pool No.	Hashtag	Total Cells (Million) Thawing	Initial Viability (%)	Run Day	Type*	Total Cells Sequenced
3381 _p **	1	C0253	2.1	79	1	E	6,005
3360		C0254	1.8	82	1	R	1,409
3369		C0251	2.0	80	1	R	1,550
Con25		C0252	5.6	90	1	C	2,744
3427	2	C0252	1.87	92	2	E	4,534
3361		C0251	1.34	87	2	R	5,628
Con19		C0253	1.47	87	2	C	1,292
3408	3	C0251	1.11	88.3	2	R	5,752
Con23		C0252	1.5	80	2	C	7,660
Failed		C0253	1.18	92	±	R	×
3381	4	C0252	2.42	88	2	E	9,174
3424		C0253	2.63	90	2	E	9,168
3360 ₂ ***		C0251	2.93	89.2	2	R	2,563
3402	5	C0251	1.34	91.8	3	E	5,080
3422		C0253	2.32	91.8	3	R	8,411
3357		C0252	1.78	82.6	3	R	4,353
3367	6	C0252	1.89	87.83	3	E	7,921
3403		C0253	1.4	90.7	3	R	5,137
3409		C0251	4.57	87.3	3	R	4,280
3359	7	C0253	3.48	83.91	3	E	10,902
380		C0252	2.21	89.6	3	E	11,126
3428		C0251	2.6	87	3	R	6,170
3395	8	C0251	2.21	84.2	3	E	4,500
3413		C0253	1.4	94.3	3	R	2,220
Con3		C0252	2.72	87.9	3	C	7974

* Type of erosional (E), ruptured (R) ACS or Stable CAD (C).

**Complimentary peripheral sample

***Secondary sample of same patient

8.3 Demultiplexing Results

The manual demultiplexing of patients from pools is shown in **Table 8** below. Patient information is separated by total cells sequenced and approved singlets, or single-cells, without multiplets detected. The capture rate percentage per pool in the table depicts the successful proportion of sequenced cells out of all total GEMs processed for that individual pool lane on the 10x chip. The singlets sorted percentage presents the total amount of singlets, without multiples, retrieved from the total amount of captured cells per pool. The individual quality control filtering of duplicates or otherwise insufficient cells may be seen on a patient-by-patient basis. Patients are labeled by their hashtag identification, which can be cross-referenced to all other patient information through **Table 7**. Pool 3 contains only two samples due to quality concerns of one sample as it was dropped while pooling right before sequencing.

Table 8: Manual Demultiplexing Singlets Sorted Per Patient

Pool	Type	C0251	C0252	C0253	C0254	Capture Rate	Singlets Sorted
1	Cells	3,937	8,852	18,849	5,355	38.65%	80.65%
	Singlets	1,500	2,744	6,005	1,409		
2	Cells	9,839	7,987	2,178		59.91%	84.31%
	Singlets	5,672	4,534	1,292			
3	Cells	9,484	17,543	<i>Discarded</i>		62.76%	81.77%
	Singlets	5,752	7,660	<i>Discarded</i>			
4	Cells	4,027	15,363	15,567		59.99%	76.57%
	Singlets	2,563	9,174	9,168			
5	Cells	8,164	6,939	13,978		64.56%	78.59%
	Singlets	5,080	4,353	8,411			
6	Cells	7,528	14,477	9,105		64.89%	77.83%
	Singlets	4,280	7,921	5,137			
7	Cells	15,144	27,694	27,158		58.73%	65.35%
	Singlets	6,170	11,126	10,902			
8	Cells	5,849	13,444	3,710		62.34%	85.27%
	Singlets	4,500	7,974	2,220			

8.4 *DSB* Normalized Antibody Panel

As seen in **Figure 31** below, a comparison of the TotalSeq-C 137 antibody panel before and after *DSB* normalization shows improvement in panel equity. In **31a**, the non-normalized panel of Pool 1 ($n = 3$) may be seen with heavy disproportionality of just a few antibodies in the upper left quadrant of the panel. Maximum expression levels are shown in yellow. In contrast, a large proportion of the non-normalized panel consists of zero or near-zero expression levels, as shown in black. In **31b**, the exact same cells are now shown after *DSB* normalization. In the normalized panel, the amount of dimmed low expression levels as well as polarization of high antibody expression, is lessened, as seen by a decrease in in total expression range. In **31c**, the fully integrated *Seurat* object with all patients may be seen. The panel presents itself as a relatively proportioned panel with few dead spaces of zero or near zero expression in black as well as a decreased polarization of expression range. In addition, a separation of clusters, as seen in the x-axis, is beginning to present itself.

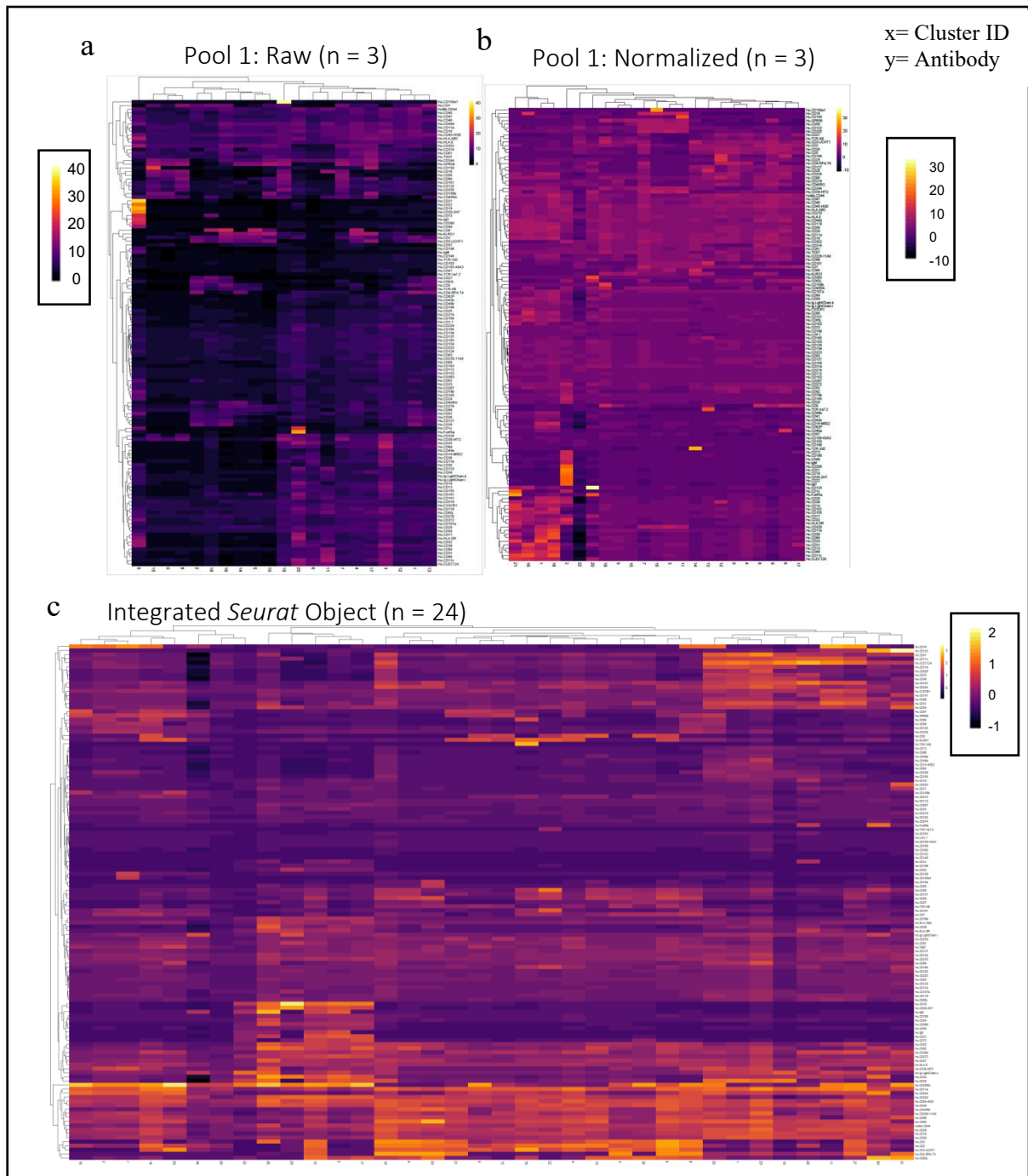


Figure 31: DSB Normalization Effects of TotalSeq-C Antibody Body Panel on Integrated Object

8.4 Creating a WNN UMAP

As seen in **Figure 32** below, the RNA-integrated UMAP information (**32a**) and the ADT UMAP information (**32b-c**) integrate into weighted pairwise affinity information (**32d**) and form 33 weighted nearest neighbor clusters with an n of 24 patient samples, 22 patients, and 129,563 single-cells (**32e**).

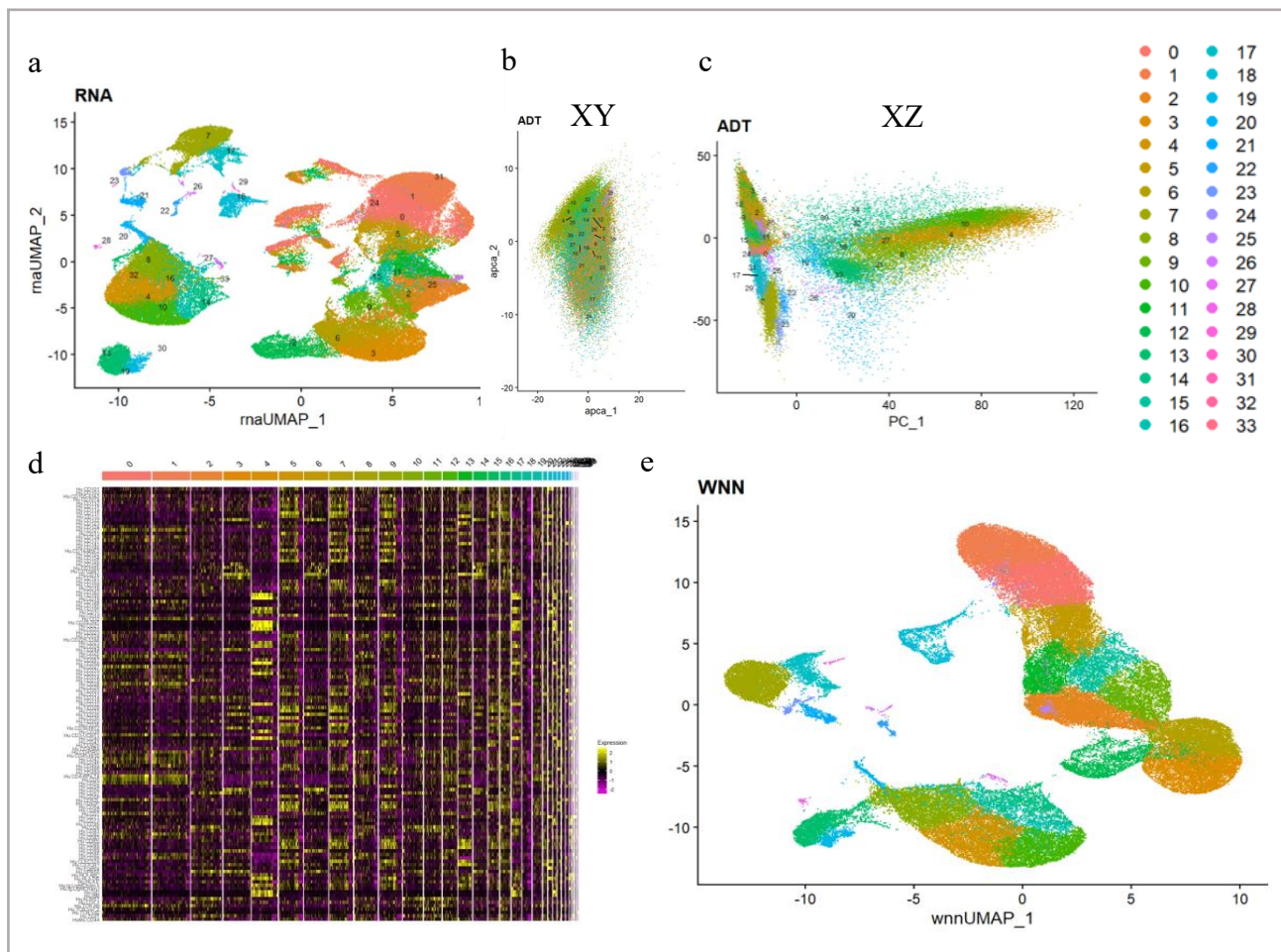


Figure 32: Constructing Weighted Nearest Neighbor UMAP

8.5 Constructing an Integrated Multimodal Atlas

As depicted in **Figure 33**, a Query-Reference by Anchoring technique whereby the blue reference and red query allows for the previously annotated cells of the reference (as seen in the right panel of **33a**) to form anchors against the query and perform annotation prediction scores (**33b**). The *Azimuth* software between the Human-PBMC CITE-seq reference library and the integrated WNN object identified 31 unique immune cell clusters from the 33 natural clusters already created in the WNN process⁹⁶. For the 22-patient cohort, 122,985 single cells were successfully annotated (**33c**). The integrated atlas may be separated (**33d**) via patient subgroup as well as by individual patients (**Figure 34**).

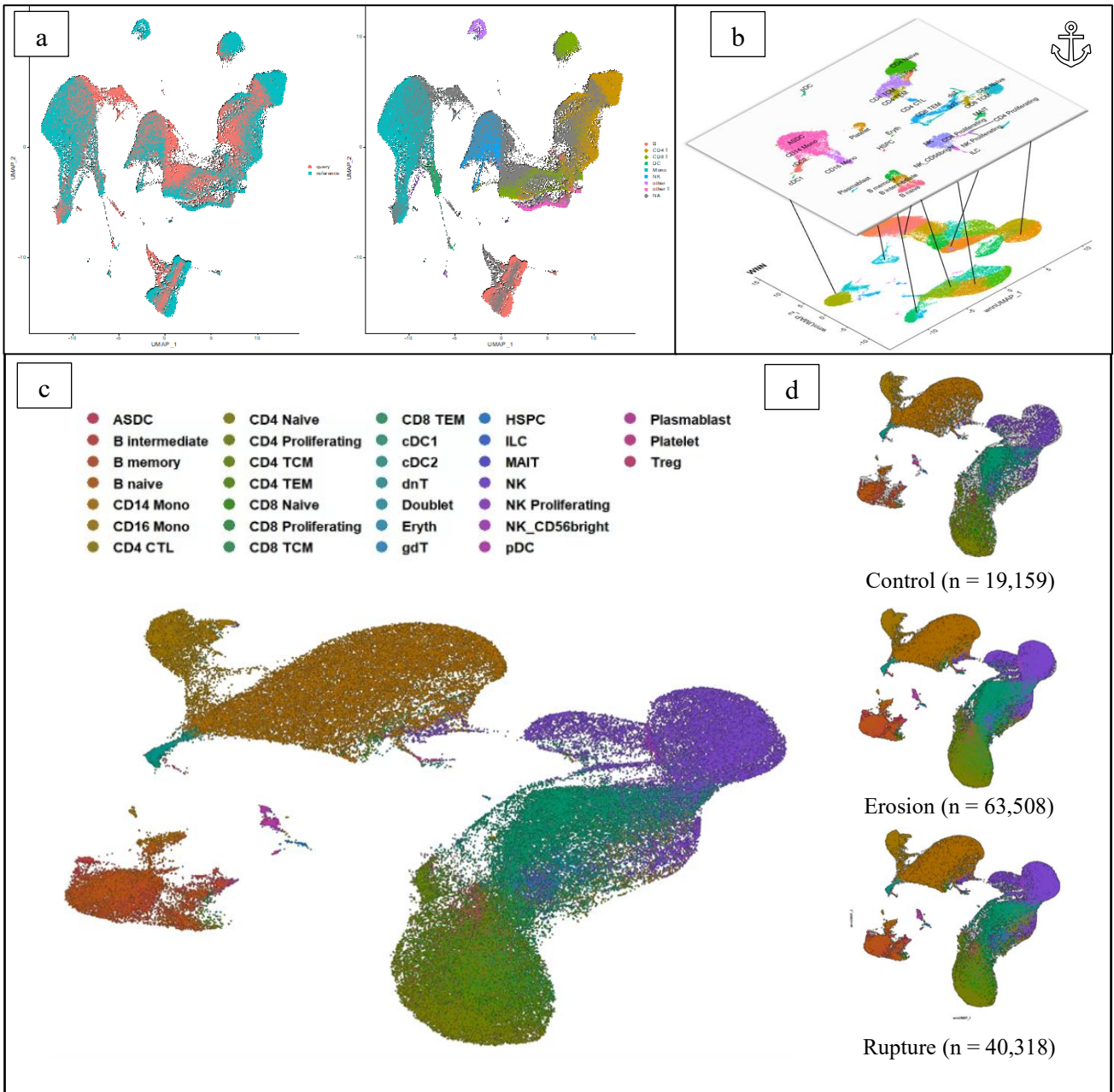


Figure 33: Constructing an Integrated Multimodal Object with Anchored Annotations (n = 129,563)



Figure 34: Patient Separated UMAPs of Integrated Multimodal Atlas

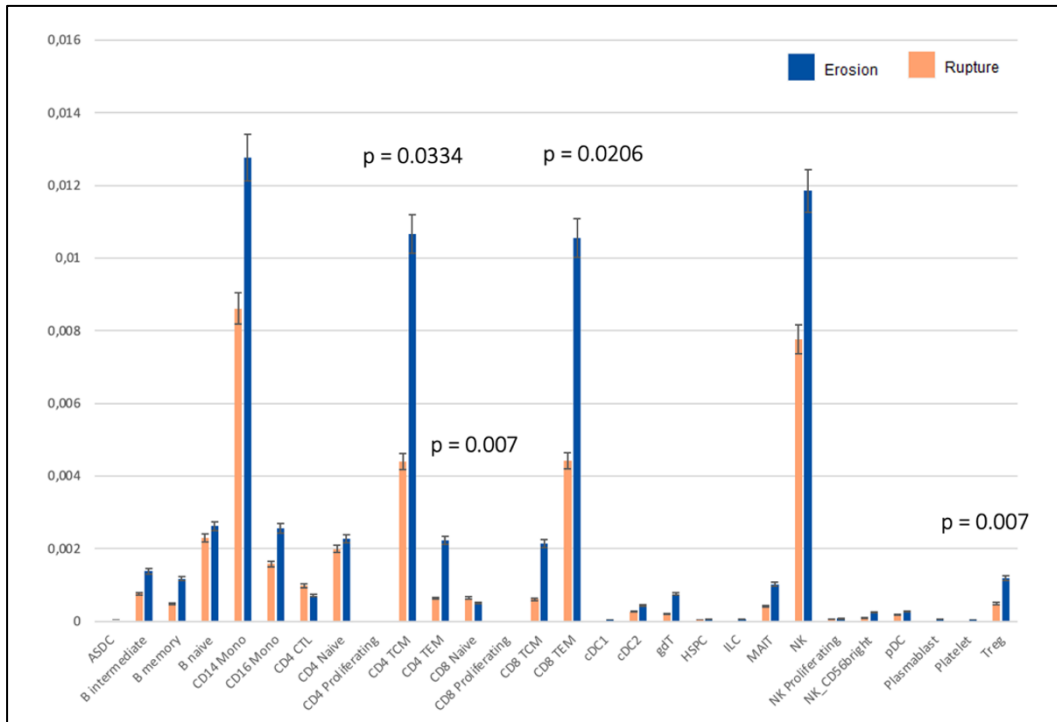


Figure 35: Mean Frequency of Immune Cell Types: Erosion vs. Rupture

Figure 35 above highlights the distribution of immune cell types, with blue representing the immune cells constituting 100% of the erosional ACS subset, and peach denoting the immune cells collectively constituting 100% of the ruptured ACS subset. In this mid-level immune cell resolution of annotation, only particular T-cells are statistically different in their frequencies between erosional and ruptured patient cells. Moreover, these differences are only seen to be as an increased frequency among these certain erosional T-cells. The T-cells that are statically different between the erosional and ruptured subsets are $CD8^+ T_{EM}$, $CD4^+ T_{CM}$, $CD4^+ T_{EM}$, $\gamma\delta T$, and Tregs. (p-values: $CD8^+ T_{EM}$ - 0.020678, $CD4^+ T_{CM}$ - 0.033409, $CD4^+ T_{EM}$ - 0.007, $\gamma\delta T$ - 0.006, Treg - 0.037443).

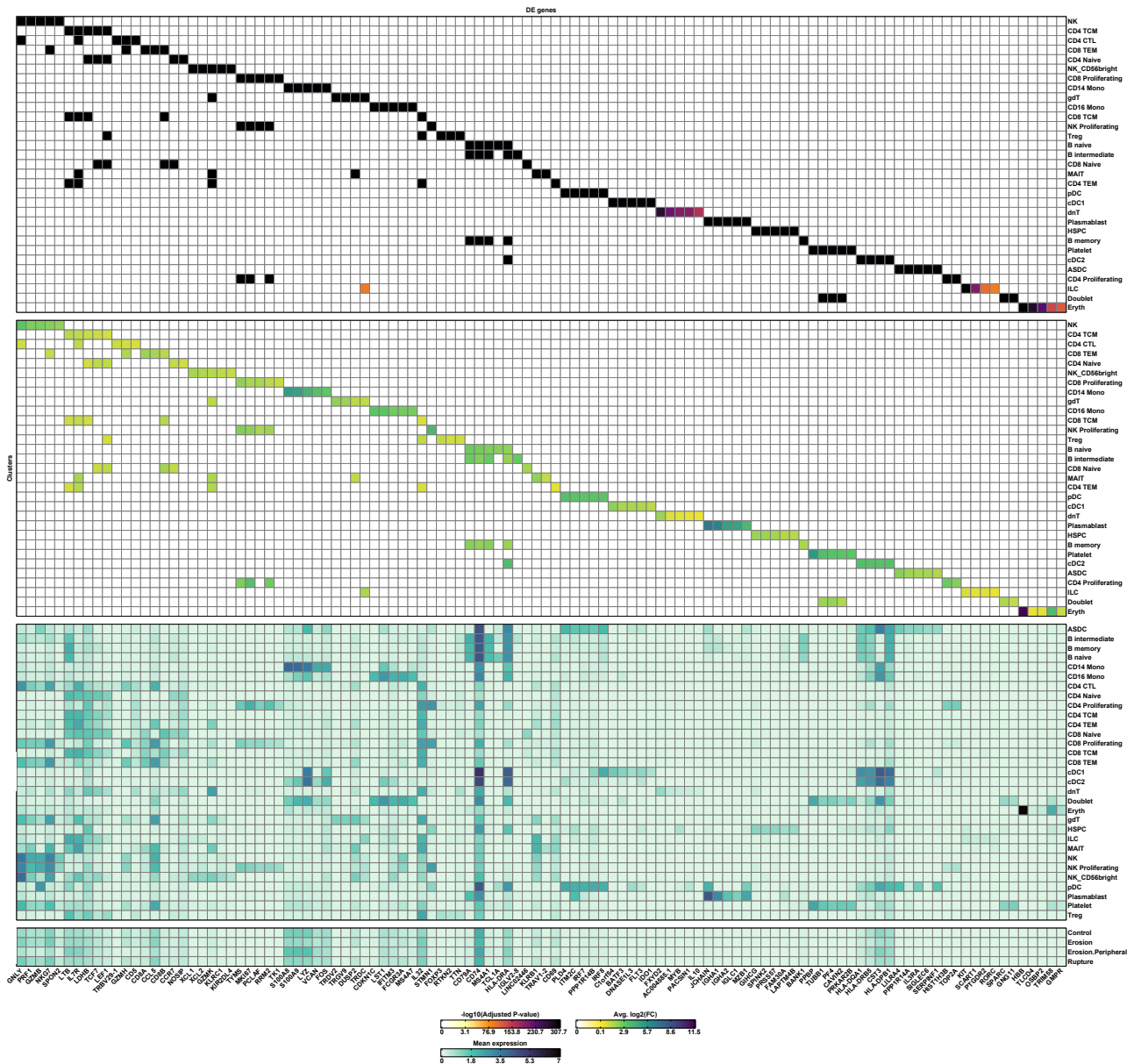


Figure 36: DE Genes of Atlas Against Immune Cell Subtypes

The differentially expressed (DE) genes of the atlas are seen in **Figure 36** above. The DE genes were calculated via Wilcoxon rank sum and a binary logarithm fold change (Log₂FC) cutoff of 0.25 to calculate the defining features of each immune cell subset against all other immune cells. The top panel of the figure presents the -Log₁₀ adjusted p-value of the immune cell subgroups against the top (max = 5) DE genes that are presented at the bottom of the figure. Following this, the secondary panel presents the same information at the top panel; however, in average Log₂FC. Finally, the bottom two panels show the mean expression of the DE genes against the patients' subgroups as well as the immune cell subtypes. With a similar process, the DE antibodies (Log₂FC cutoff = 0.1) from the TotalSeq-C panel may be seen in **Figure 37** below.

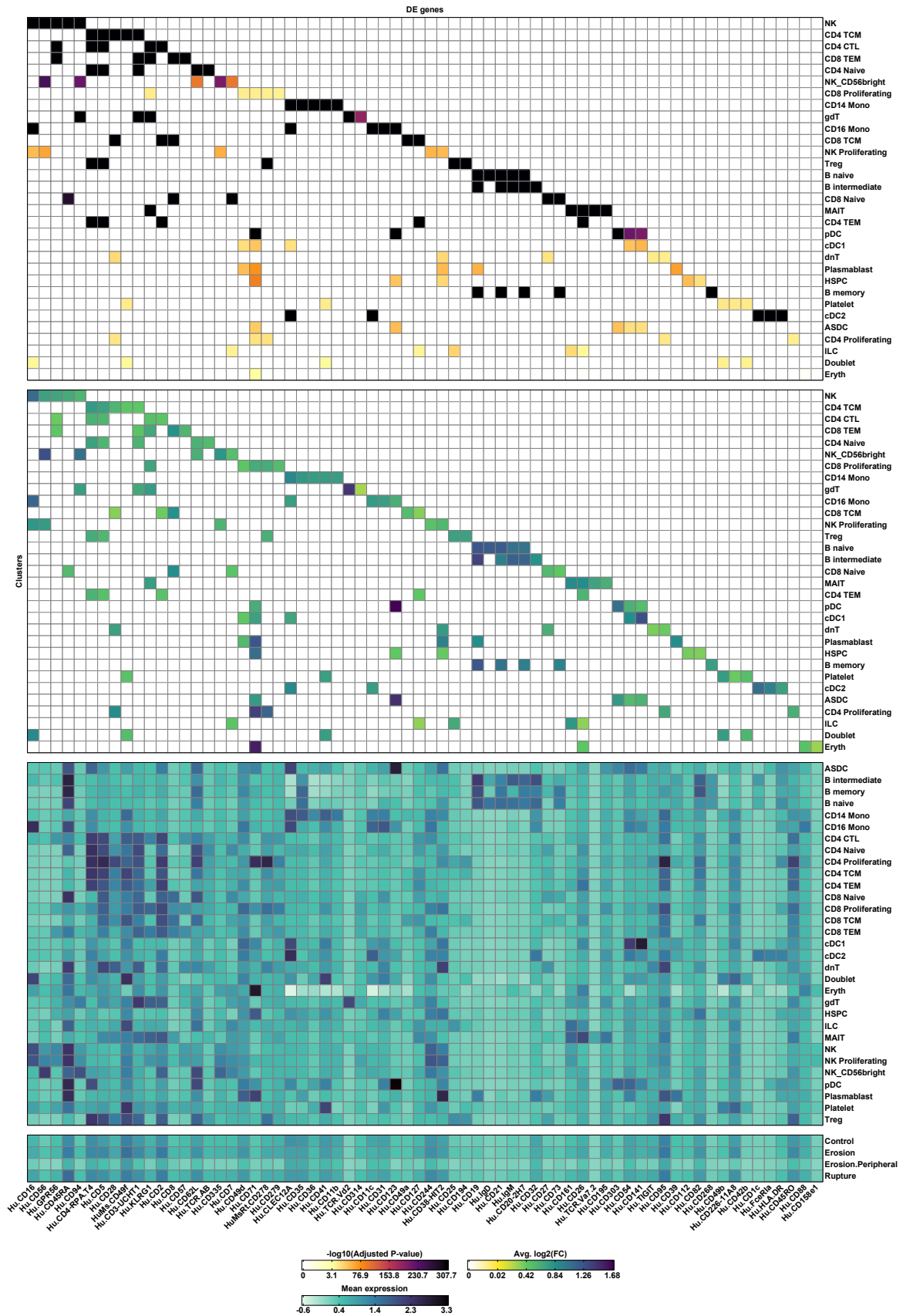


Figure 37: DE TotalSeq-C Antibodies of Atlas Against Immune Cell Subtypes

Chapter 9. T-Cell Sub-Clustering Analysis

9.1 T-Cell Sub-clustering: Nearest Neighbor Groupings

As previously mentioned, a process of sub-clustering of the main object's T-cells was conducted. This sub-clustering analysis yielded 15 unique T-cell clusters, as shown in **Figure 39** below. Naïve CD4⁺ (5) and CD8⁺ subsets (6) grouped in the top left corner contributed to the characteristics of the y-dimension or 'WNN UMAP 2'. In contrast, CD8⁺ terminal effector T-cells (10) grouped at the furthest right region and therefore contributed to the characteristics of the x-dimension or 'WNN UMAP 1'. Naïve CD8⁺ T-cells (6) gravitated further along the x-dimension than CD4⁺ T cells (5). Follicular T-cells (3) grouped just under the similarly expressing CD45RA CD4⁺ T-cells⁴⁵. The other helper T-cell clusters T_{H1} (11), T_{H2} (14), T_{H17} (13), and T_{H1}-T_{H17} (12) grouped together throughout the y-dimension and on the left half of the x-dimension. Tregs (8) grouped in the bottom left corner thereby contributing the least to the characteristics of both dimensions. While MAIT (4) and $\gamma\delta$ T V δ 2⁺ (15) cells clustered remotely away from many of the other clusters, $\gamma\delta$ T (7) cells clustered together with CD4⁺ T_{TE} and CD8⁺ T_{TE} cells on the furthest right grouping of clusters along the x-dimension. Finally, CD8⁺ T_{CM} (1) and CD8⁺ T_{EM} (2) are grouped together to the left of the terminal effector cells; however, on the right, a larger grouping of clusters is separate from the helper cells.

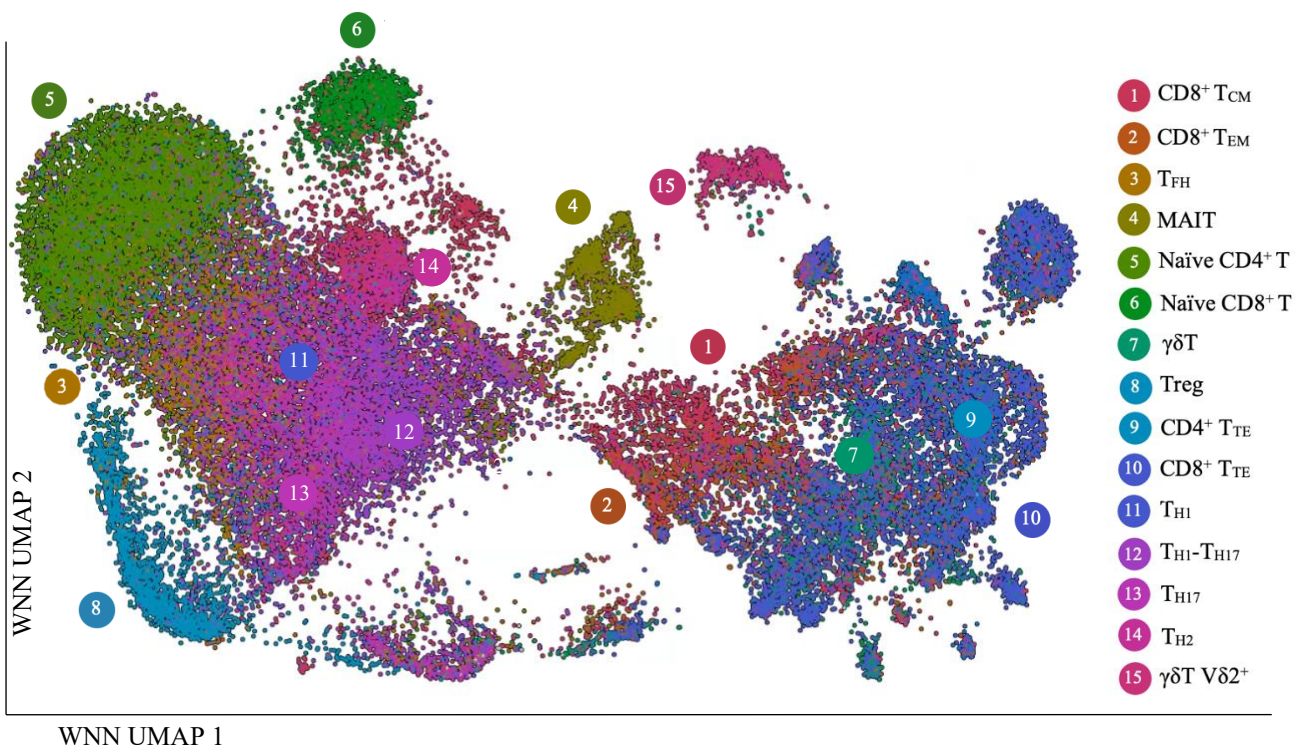


Figure 39: WNN T-cell Sub-clustering (n = 47,575)

9.2 T-Cell Sub-Clustering Frequencies

The mean patient subtype frequency for each T-cell subset may be seen in **Figure 40** below for sample subgroupings of control (n = 4), erosion (n = 9), and rupture (n = 11). The significance of enrichment was calculated using the students t-test, assuming unequal variances and a significance threshold of $p < 0.05$ ¹¹³. For ruptured ACS, both ruptured Naïve CD4⁺ T-cells ($p = 0.0412$, 95% CI 0.185 – 1.95) as well as CD4⁺ T_{TE} cells ($p = 0.0092$, 95% CI 0.257 – 1.922) were enriched compared to erosion. For erosional ACS, T_{H1}-T_{H17} cells ($p = 0.0392$, 95% CI 0.155 – 0.165) as well as CD8⁺ T_{CM} cells were found to be enriched as compared to control ($p = 0.0498$, 95% CI 0.194 – 0.206). In addition, erosional T_{H17} cells were enriched as compared to both rupture and control cells ($p = 0.019$, 95% CI 0.166 – 0.174 and $p = 0.008$, 95% CI 0.151 – 0.159, respectively).

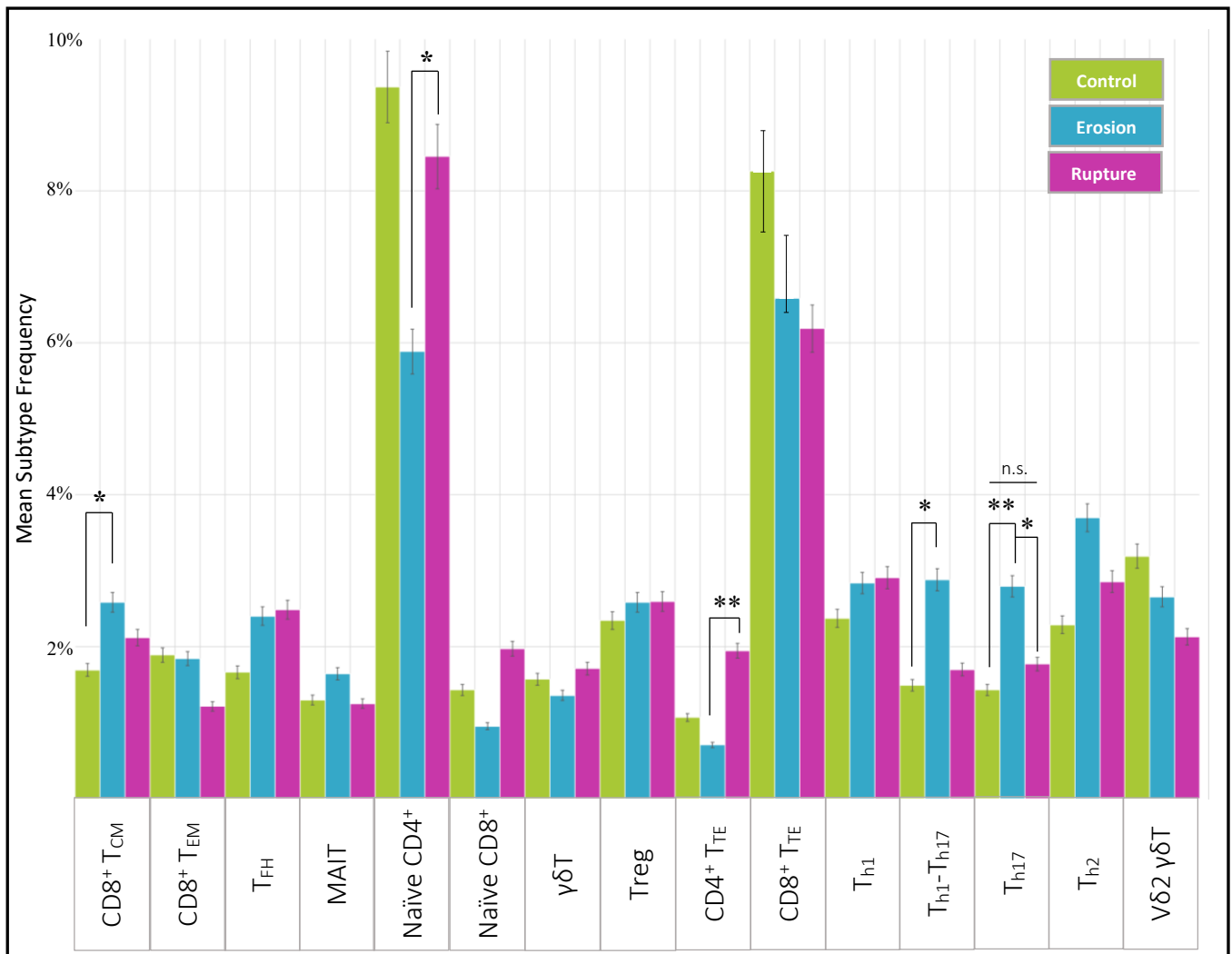


Figure 40: Mean Frequency of T-cell Subsets in Each Patient Subtype

8.3 UMAP Separation by Patient Subsets & Individual Patients

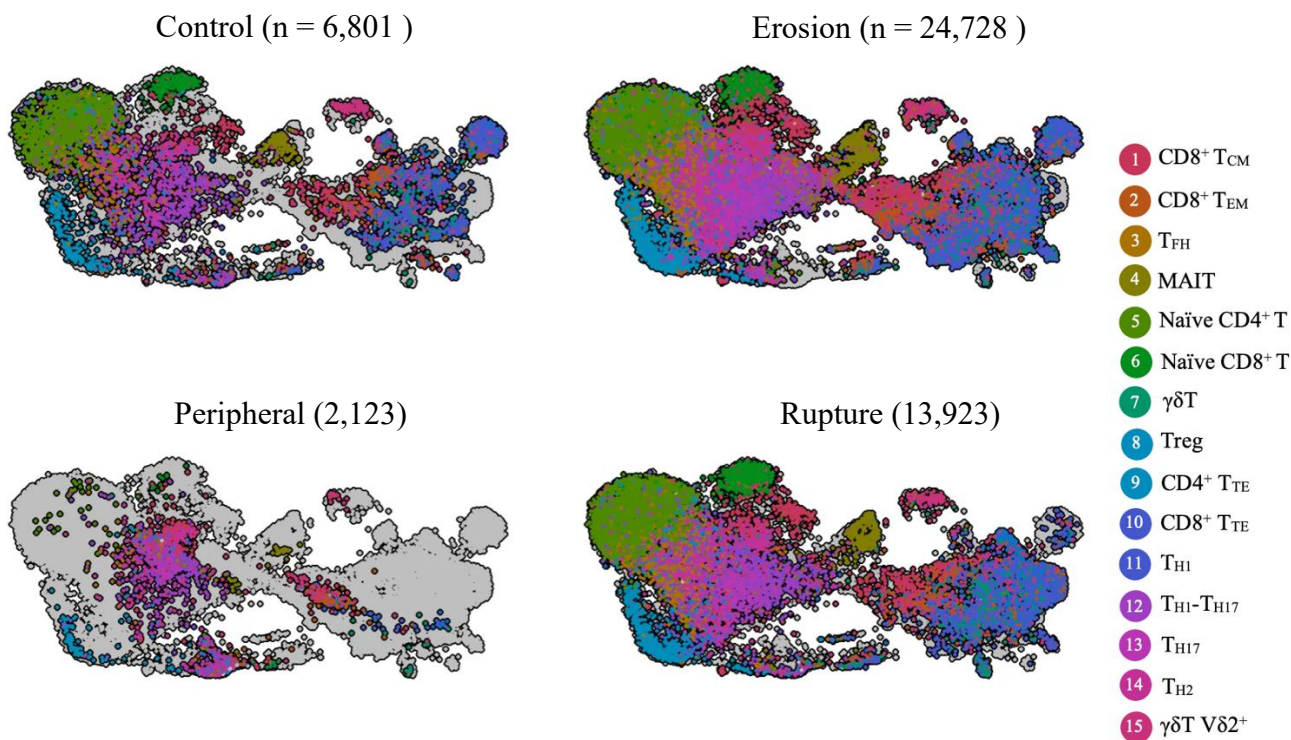


Figure 41 : Separation of UMAP by Patient Subtype

As seen in **Figure 41** above, the T-cell sub-clustering may be separated by patient subtype as was done previously for the entire multimodal UMAP. The proportion of total T-cells was 4.41% higher in erosion than in rupture (38.94% and 34.53%, respectively) when calculating between the T-cell sub-clustering and the entire multimodal UMAP. The proportion of total T-cells was also 35.35% for the peripheral sample and 35.49% for the control subtype. In **Figures 42-43** below, the T-cell sub-clustering separated by individual patients may be seen.

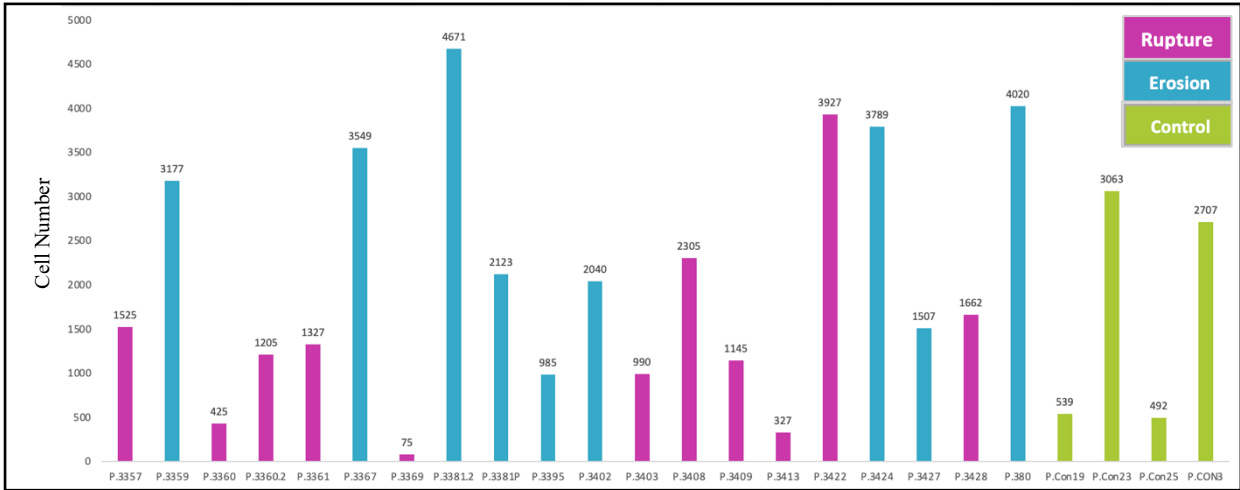


Figure 42: T-cell Numbers Derived from Each Patient

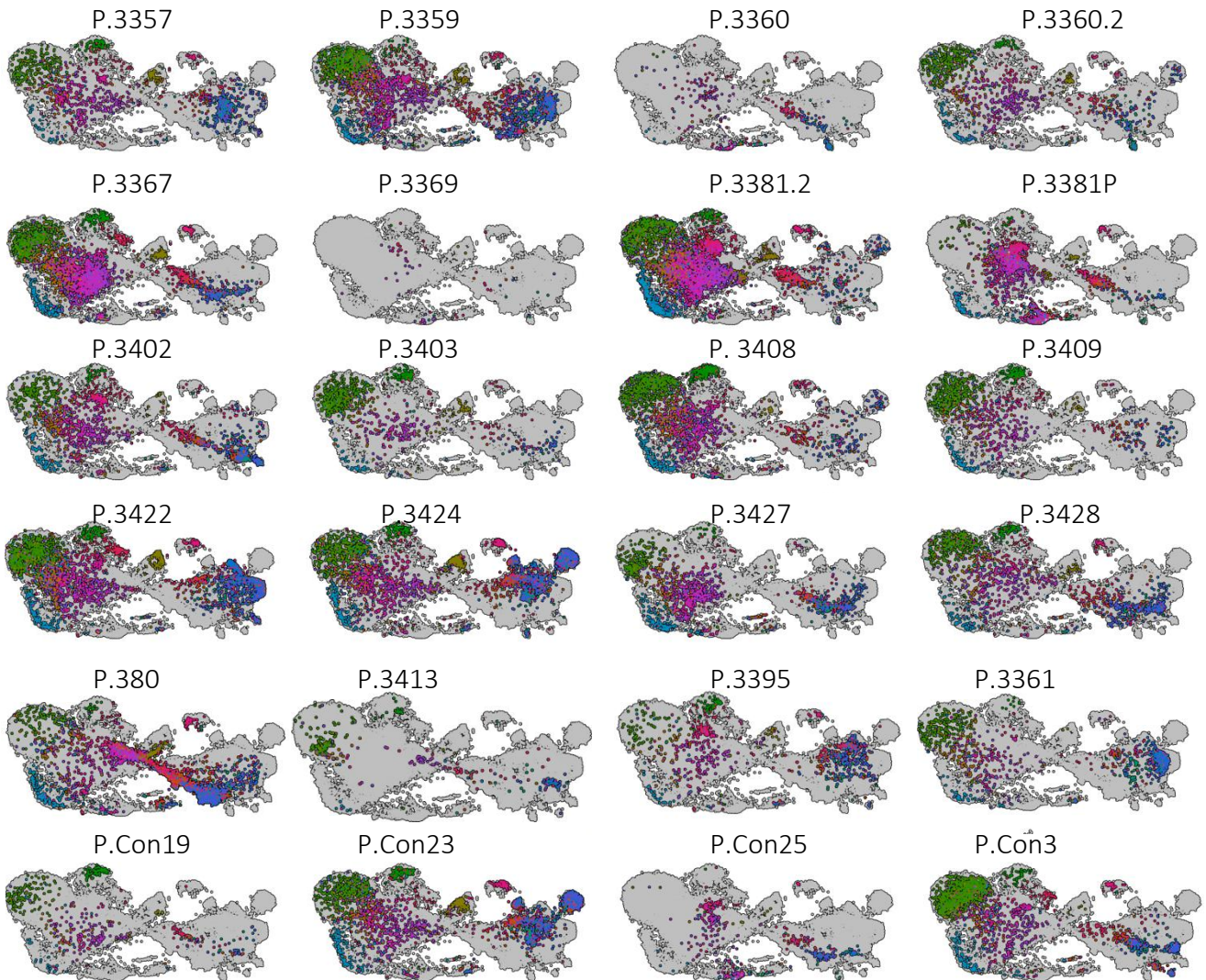


Figure 43: Separation of UMAP by Individual Patients

9.3 Group-wise Differential Expression Analysis

Figure 44 below depicts the DE genes of the T-cell sub-clustering. A Wilcoxon rank sum test was used with a log2 fold change threshold of 0.25 whereby groups were defined as patient subgroups with a command to include T-cell subtype information into the test. The $-\log_{10}$ adjusted P-values for the DE genes against the T-cell clusters may be seen in the top panel, followed by their average Log2FC below. The bottom panel of the Figure depicts the mean expression differences amongst the de genes based on patient subtype groupings: control, erosion, peripheral, and rupture. The protein Cystatin F encoded by the *CST7* gene, is known to be expression in natural killer and CD8⁺ T-cells and is thought of as a marker of acute inflammation in humans; it appears to present a slightly higher mean expression in control (1.5) & erosional (1.25) $\gamma\delta$ T (non-V δ 2) cells than rupture or the peripheral sample (1) ¹¹⁴. In contrast, the *IL7R* gene, which provides instructions for the synthesis of the interleukin 7 receptor (IL-7R) alpha chain protein, appears to presents a slightly higher mean expression in rupture and erosion (2.4) as compared to control (1.9), while the peripheral sample shows an very high (2.9) mean expression in T_{H1}-T_{H17} cells.

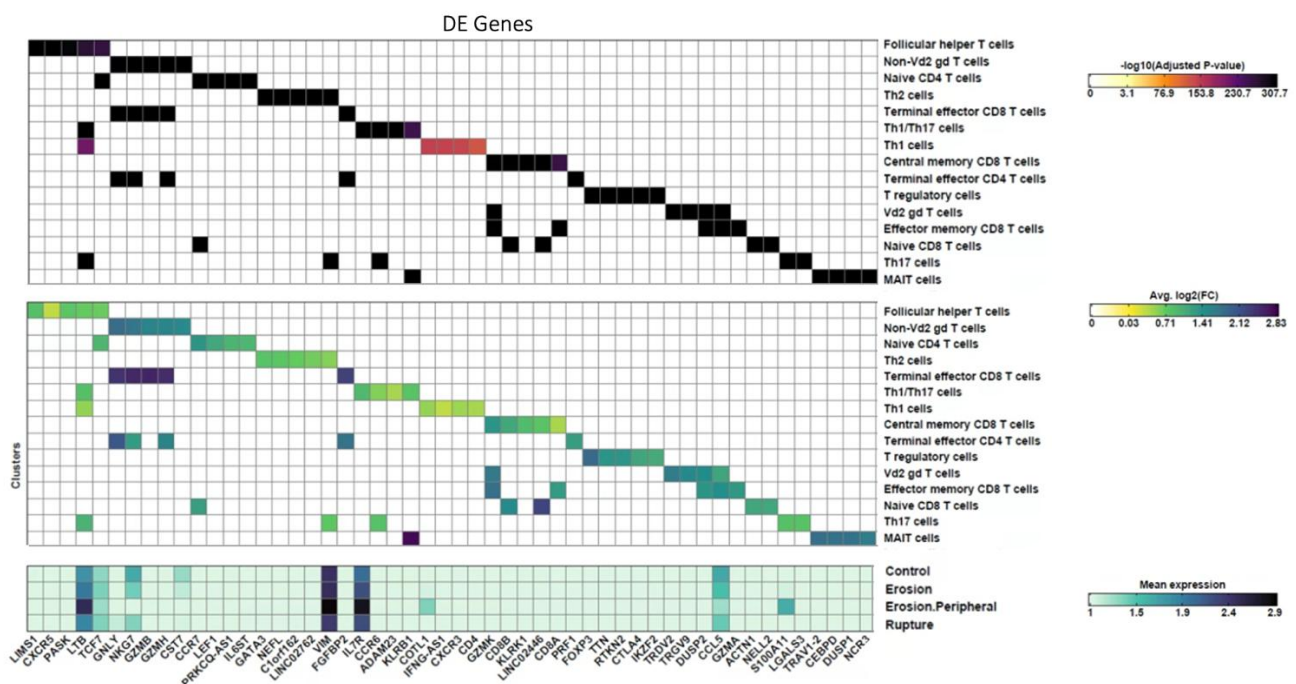


Figure 44: T-Cell DE Group-Wise Analysis from RNA Expression Against Immune Cell Subtypes

Figure 45 below depicts the DE TotalSeq-C antibodies of the T-cell sub-clustering. A Wilcoxon rank sum test was used with a Log2FC threshold of 0.1 whereby groups were defined as patient subgroups with a command to include T-cell subtype information into the test. The $-\text{Log}_{10}$ adjusted

p-values for the DE genes against the T-cell clusters may be seen in the top panel, followed by their average log2FC below. The bottom panel of the figure depicts the mean expression differences amongst the de genes based on patient subtype groupings: control, erosion, peripheral, and rupture. The cell surface protein Integrin $\alpha 6$ or CD49f is encoded by the *ITGA6* gene and mediates cell-to-cell and cell-to-stroma adhesion¹¹⁵. In **Figure 45**, CD49f appears to present a higher mean expression in erosion (1.9) than rupture or control (1.4) for all T helper cell subsets; however most significantly for Th₁₇ and Th₂ cells. In addition, CD45RA and CD62L mean expression appears higher in rupture than erosion or control for naïve and $\gamma\delta$ T-cells. Finally, CD28 and CD82 mean expression appears higher in erosion and rupture than control for all T-cell subsets.

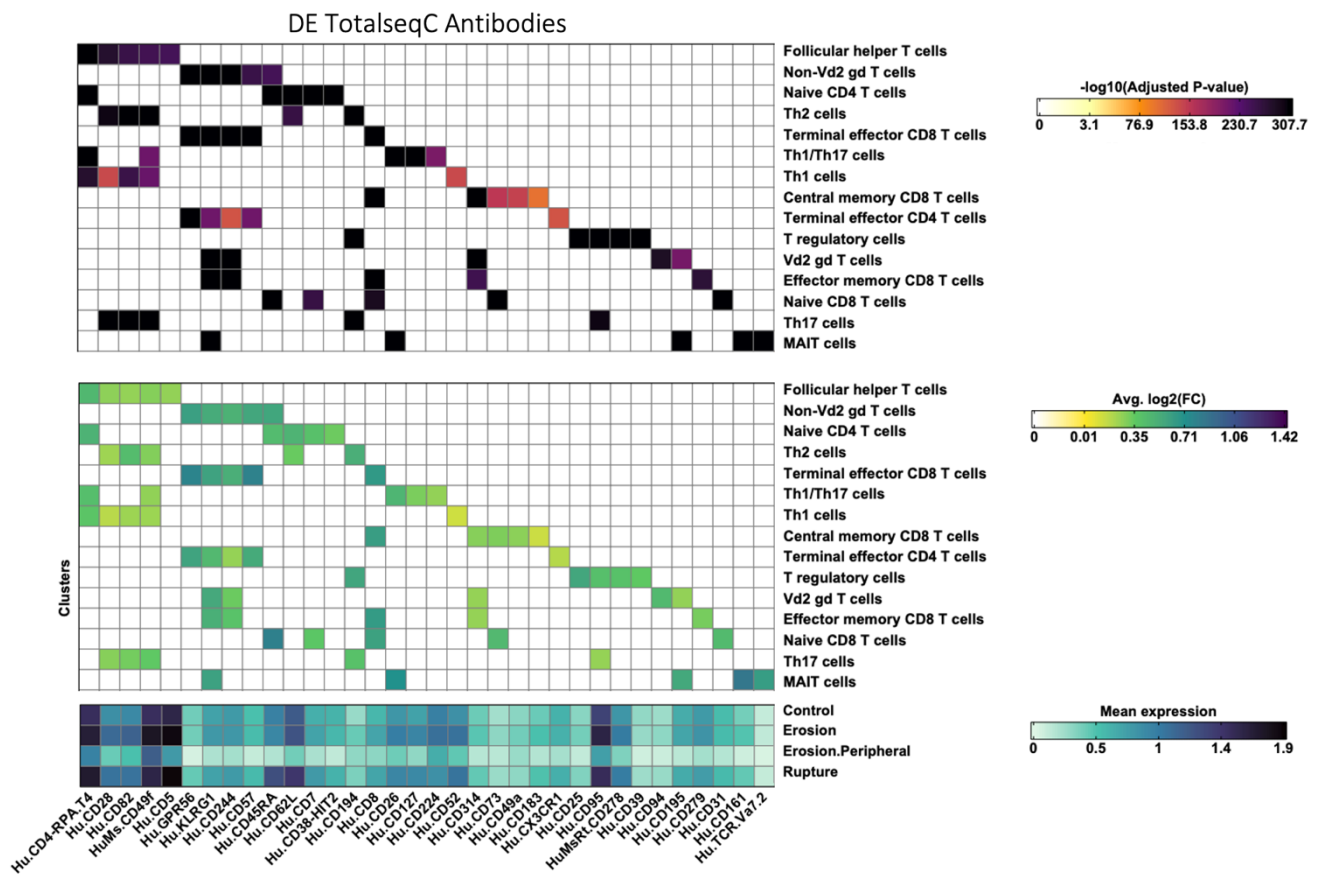


Figure 45: T-Cell DE Analysis from TotalSeq-C Antibody Panel Against Immune Cell Subtypes

9.4 Functional Enrichment Analysis of Erosional T_{H17} Cells

In **Figure 46**, a functional enrichment analysis of T_{H17} cells was conducted using the g:Profiler software ¹¹⁶. The genes for input into g:Profiler were selected through Wilcoxon rank sum differential expression analysis, comparing erosional T_{H17} cells to ruptured T_{H17} cells (Erosion n = 1,685 cells; Rupture n = 591 cells) using the *Seurat* R package. A Log₂FC cutoff of 0.25 was applied, and significance was determined using the g:SCS algorithm ¹¹⁶. The Gene Ontology (GO) source presented in **Figure 46** arises from the GO cellular component. GO terms for cell junction (p = 1.050e⁻⁶), anchoring junction, cell-substrate junction (p = 3.597e⁻¹³) and focal adhesion (2.128e⁻¹³) were found to be significantly enriched in erosional T_{H17} cells as opposed to rupture TH17 cells.

From the DE analysis, three genes stood out. First, Cathepsin D (*CTSD*), a protease involved in protein degradation and tissue modeling was found enriched in erosional T_{H17} cells (adjusted p-value < 0.001; Log₂FC = 1.15)¹¹⁷.

Secondly, *TYROBP* or tyrosine kinase-binding protein, which encodes a transmembrane signaling polypeptide that contains an immunoreceptor tyrosine-based activation motif (ITAM), was the second most upregulated gene in erosional T_{H17} cells as compared to ruptured T_{H17} cells (p < 0.001; Log₂FC = 3.33) ¹¹⁸.

Finally, the NK cell granule protein (*NKG7*), which regulates cytotoxic granule exocytosis and inflammation, was the highest upregulated gene in erosional T_{H17} cells as compared to rupture T_{H17} (p < 0.001; Log₂FC = 4.02) ¹¹⁹.

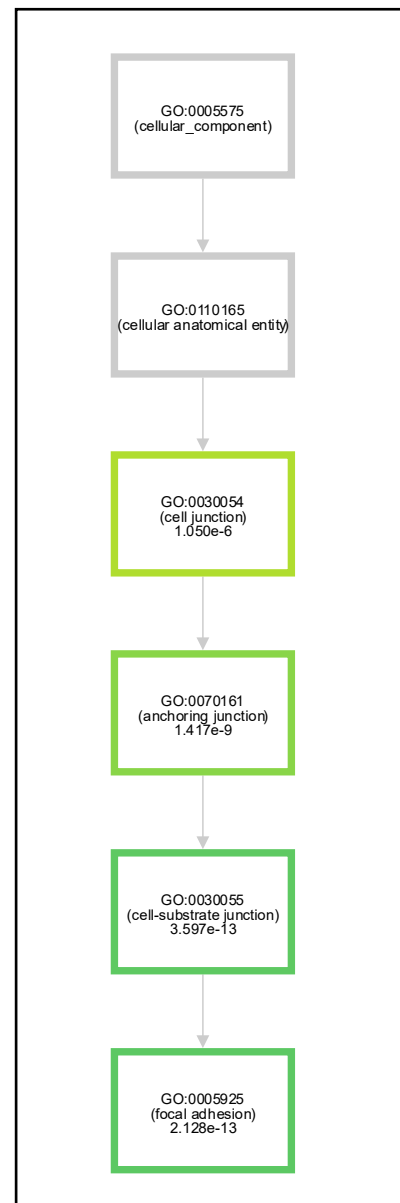


Figure 46: Erosional T_{H17} GO Enrichment

Chapter 10. Looking Closer at the TCR Repertoire of ACS Patients

10.1 A Trimodal UMAP: Erosion vs. Rupture

After integrating all library information and patient information into one UMAP, annotating T-cell information to a more detailed resolution via software package *SingleR*, and software patching the *scReptoire* package to cooperate with Seurat objects- a trimodal WNN Repertoire UMAP was created to investigate further the T-cells with a focus of comparing the erosional vs. rupture TCR repertoires.

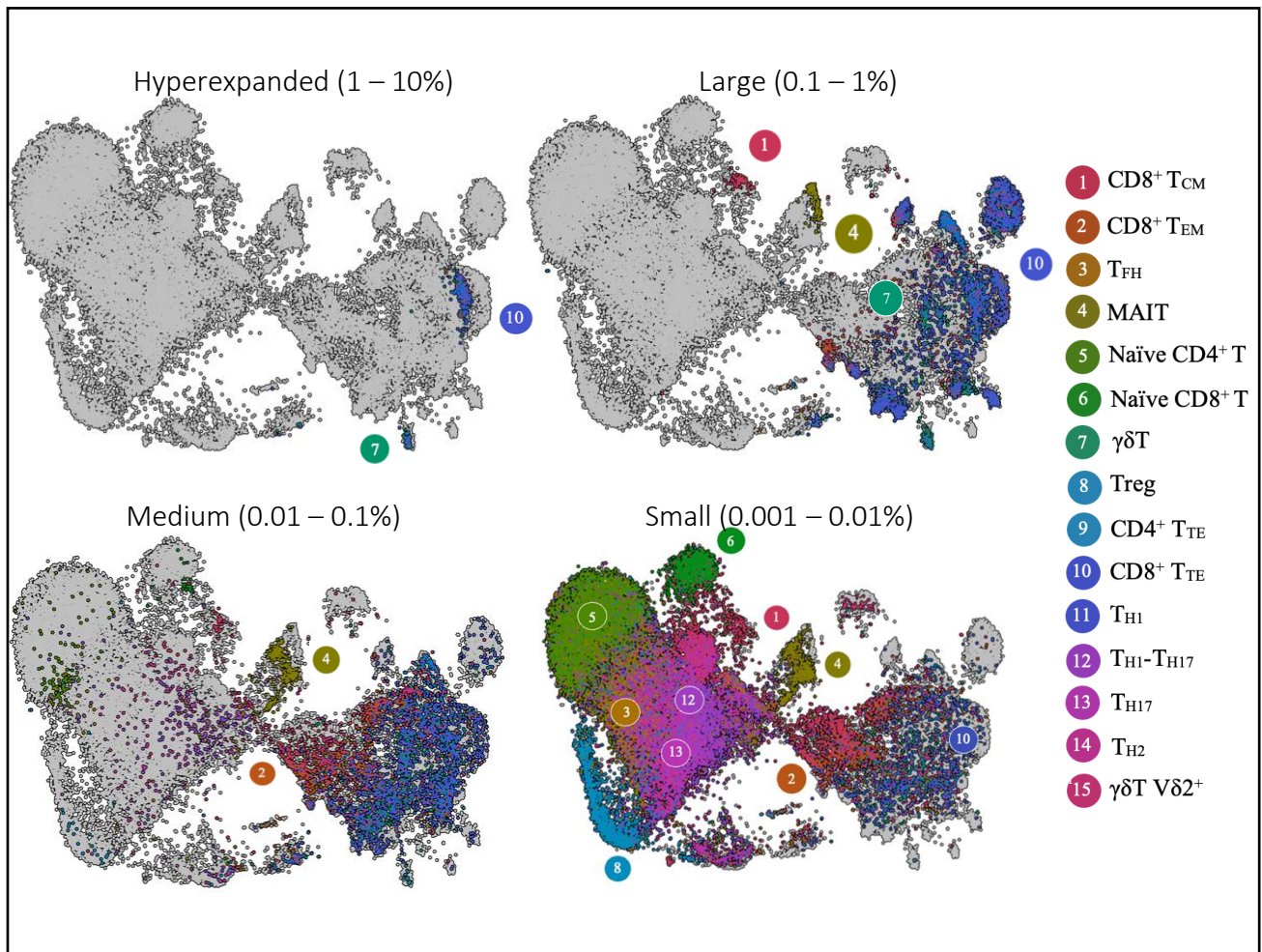


Figure 47: T-Cell Subset Locations at Different Clonotype Expansion Levels (n = 32,164)

As seen above, **Figure 47** presents the 15 unique T-cell subtype clusters now in a trimodal UMAP. Cells are binned based on the different clonotype expansion levels: hyperexpanded (1-10%), large (0.1-1%), medium (0.01-0.1%), and small (0.001-0.01%). Within the binned hyperexpanded cells, CD8⁺ T_{TE} cells (10) as well as γδT (non-Vδ2⁺) (7) cells appear. Within the large bin, more γδT (non-Vδ2⁺) and CD8⁺ T_{TE} cells appear, as well as CD8⁺ T_{CM} cells (1). Within the binned medium cells, CD8⁺ T_{EM} cells (2) and Naïve CD4⁺ T-cells (5) appear on top of previously mentioned cells. Within the small bin, Tregs (8) and the remaining of the Naïve and helper T-cells appear.

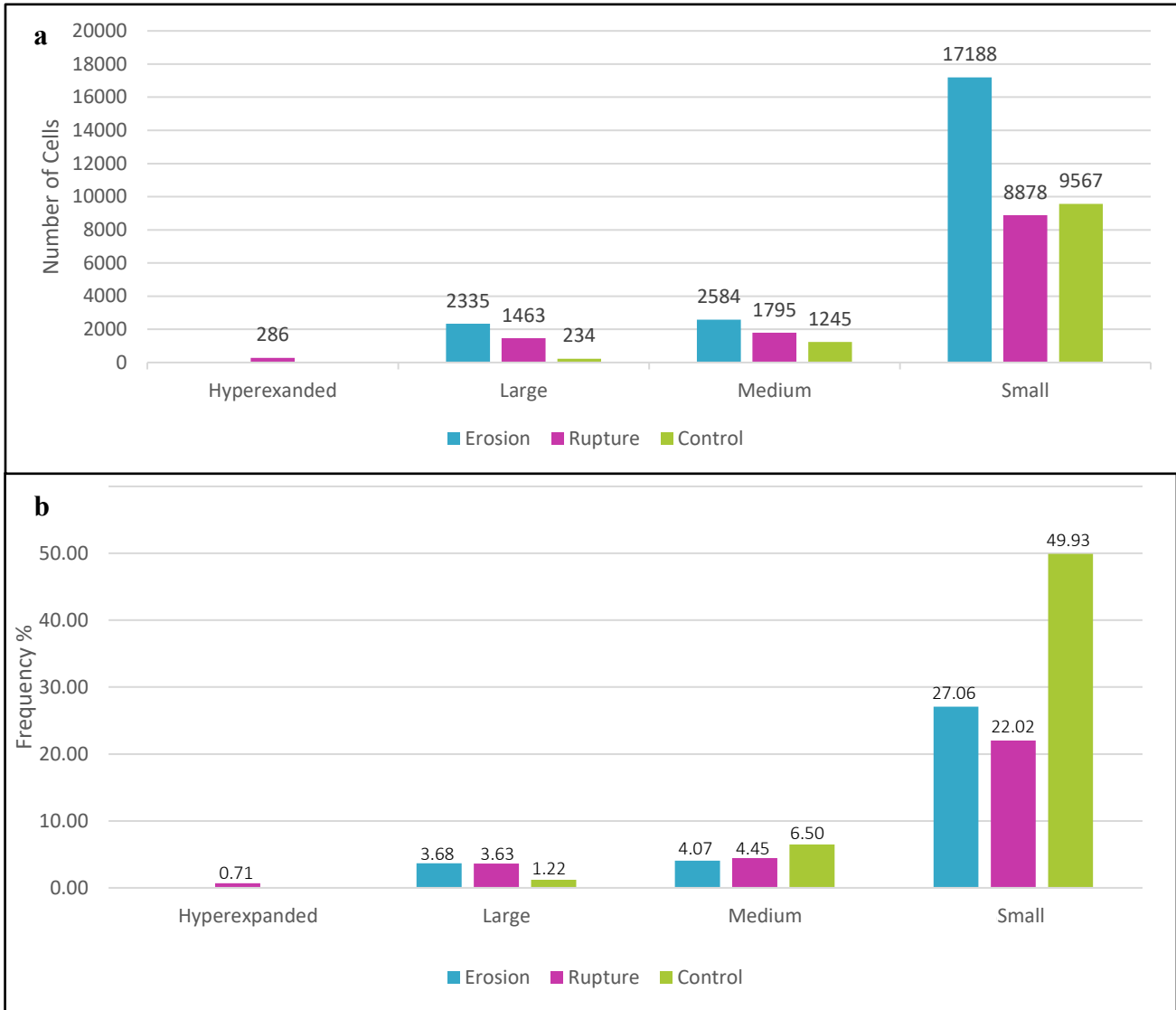


Figure 48: Binning Quantities of Clonal Expansion Among Patient Subtyping (n = 45,575)

Above in **Figure 48**, the quantities of clonal expansion per patient subtyping are depicted by expansion levels. Sections **48a** and **48b** portray the number of cells and the proportion of cells by subtype, respectively.

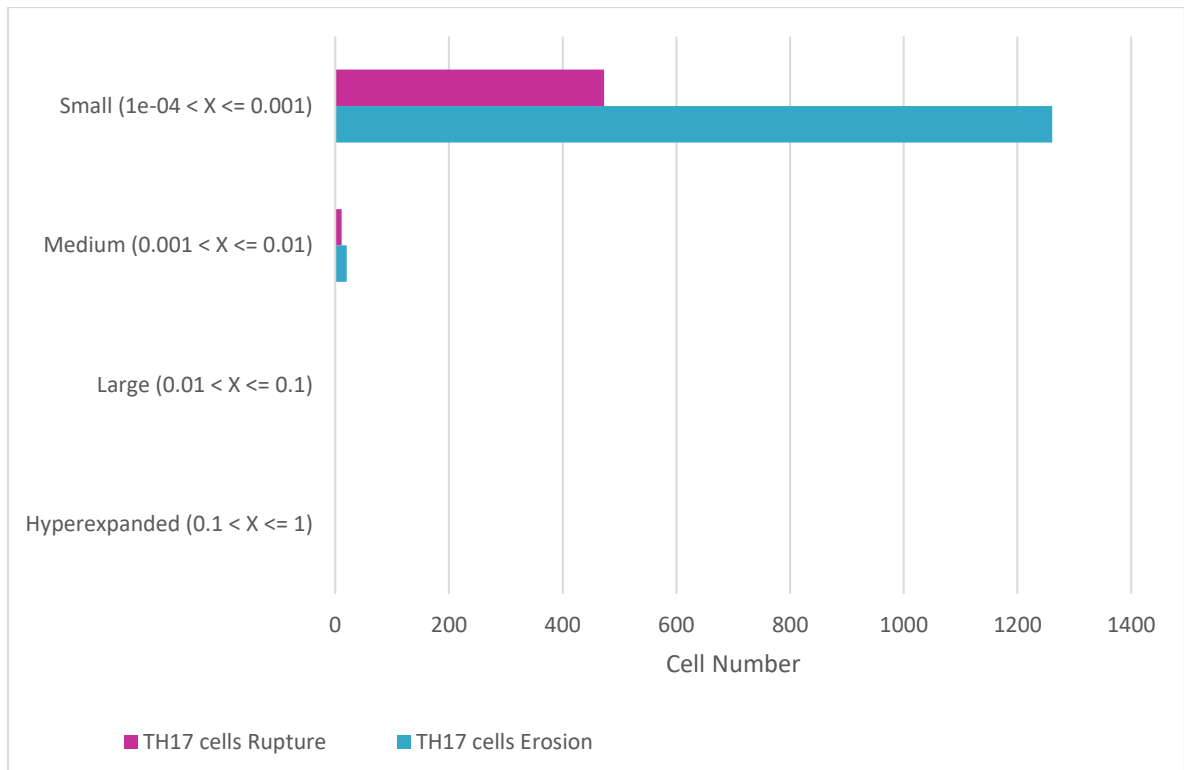


Figure 49: T_{H17} Clonotype Size: Rupture vs Erosion

As seen in **Figure 49** above, the T_{H17} clonotype sizes of both rupture and erosion subgroups are mostly small or within the range of 0-0.01% of the total repertoire. The erosional T_{H17} cells, however, are approximately twice the cell number than the ruptured T_{H17} cells. Below, **Figure 50** presents the distribution of cell number per bin and per T-cell subgroup of rupture and erosional cells.

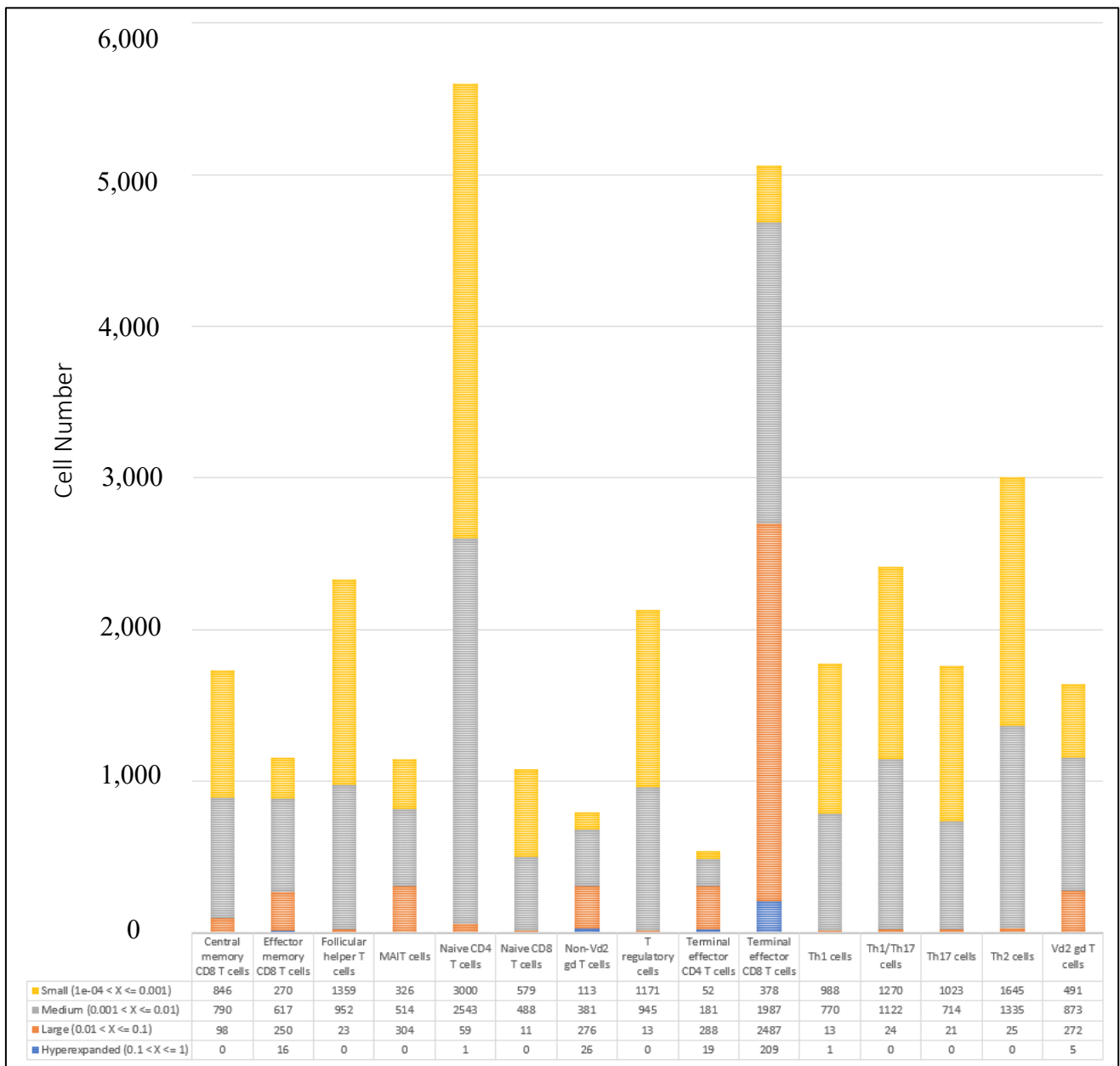


Figure 50: T Cell Clonotype by Expansion Level: Rupture vs. Erosion (n = 32,164)

In **Figure 50** above, the information on which T-cell subsets contain which binning quantities of clonal expansion is presented. In **Figures 51** below, the DE genes and TotalSeq-C antibodies are presented with the Wilcoxon rank sum test and Log2FC thresholds of 0.25. The DE analysis was organized as to compare against T-cell subtypes and demand the grouping information of the patient subgroups. In the **Figure Section 48b**, the 286 cells that are found to be hyperexpanded pertain to only ruptured plaque cells. Only two patients present hyperexpanded clonality in the entire cohort. These are rupture patients P.3360 (n = 55) and P.3361 (n = 231).

As seen in **Figure 48**, 209 of these cells are CD8⁺T_{TE} cells whereby 31 cells pertain to P.3360 (7.29% clonality) and 153 cells to P.3361 (11.54% clonality). Both patients have nearly even numbers

of $\gamma\delta T$ (non- V $\delta 2^+$) cells whereby P.3360 has 18 or a 4.2% clonality and P.3361 19, or a clonality of 1.432% clonality.

10.2 Groupwise DE Analysis

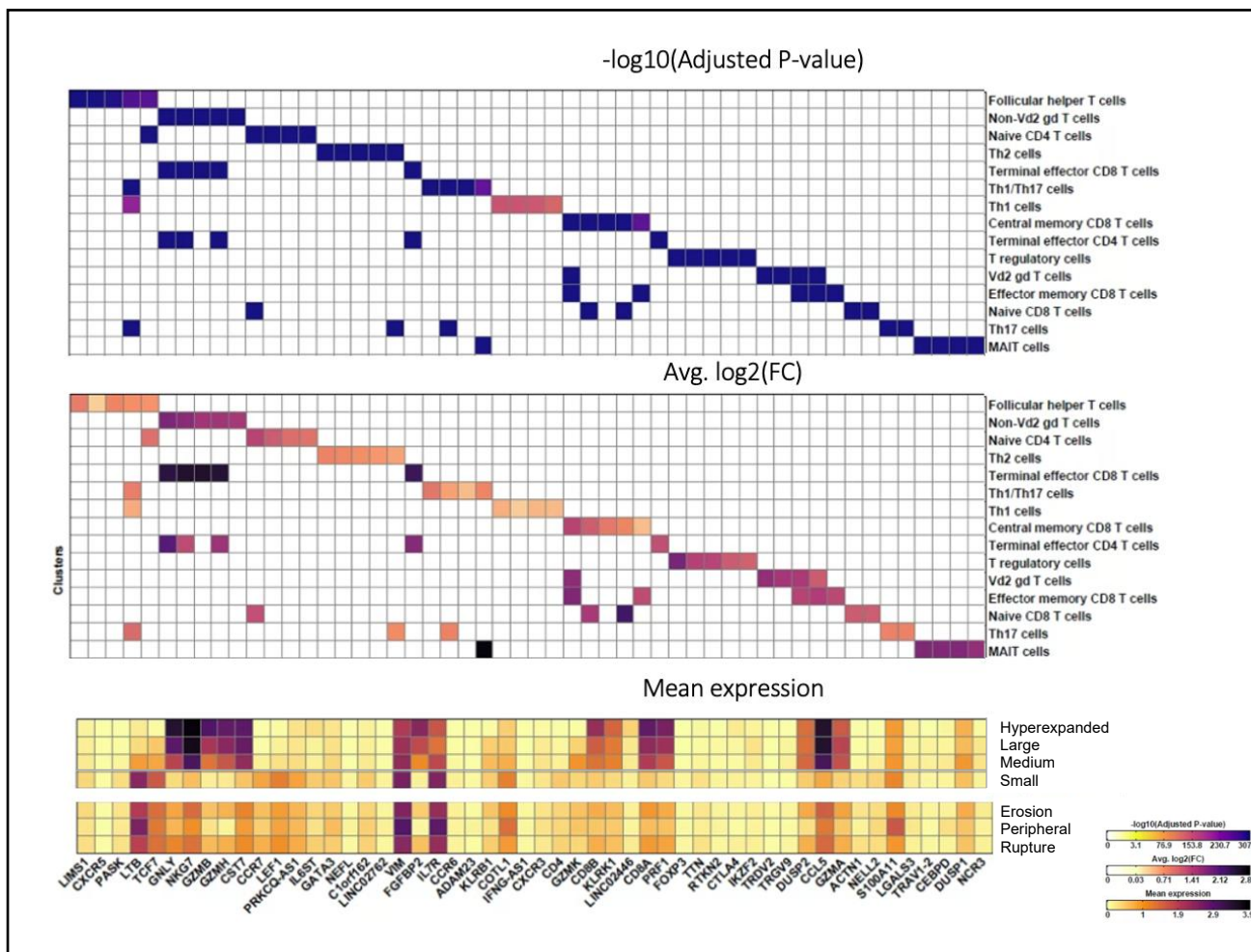


Figure 51: T-Cell DE Analysis from RNA Expression with Clonal Expansion Information

Figure 51 above presents the T-cell DE analysis of RNA expression with clonal expansion information embedded in another mean expression graph. The fibroblast growth factor binding protein family 2 (*FGFBP2*) gene appears to have a high mean expression in hyperexpanded cells as opposed to small and steadily decreases this mean expression level as the clonal bin size gets smaller. This cohort only contains ruptured hyperexpanded cells, as shown earlier in **Figure 48**.

10.2 Rarefaction Diversity Analysis

As seen in **Figure 52** below, the diversity of each patient TCR was compared via rarefaction analysis. An estimated diversity was calculated using the Chao1 diversity index, in which estimates the number of rare or unobserved clonotypes that are likely to be present but perhaps missed in the samples process ¹²⁰. The conducted rarefaction analysis appeared to result in fewer levels of estimated diversity or unique clonotypes in erosional patients as opposed to rupture and ccs or control patients.

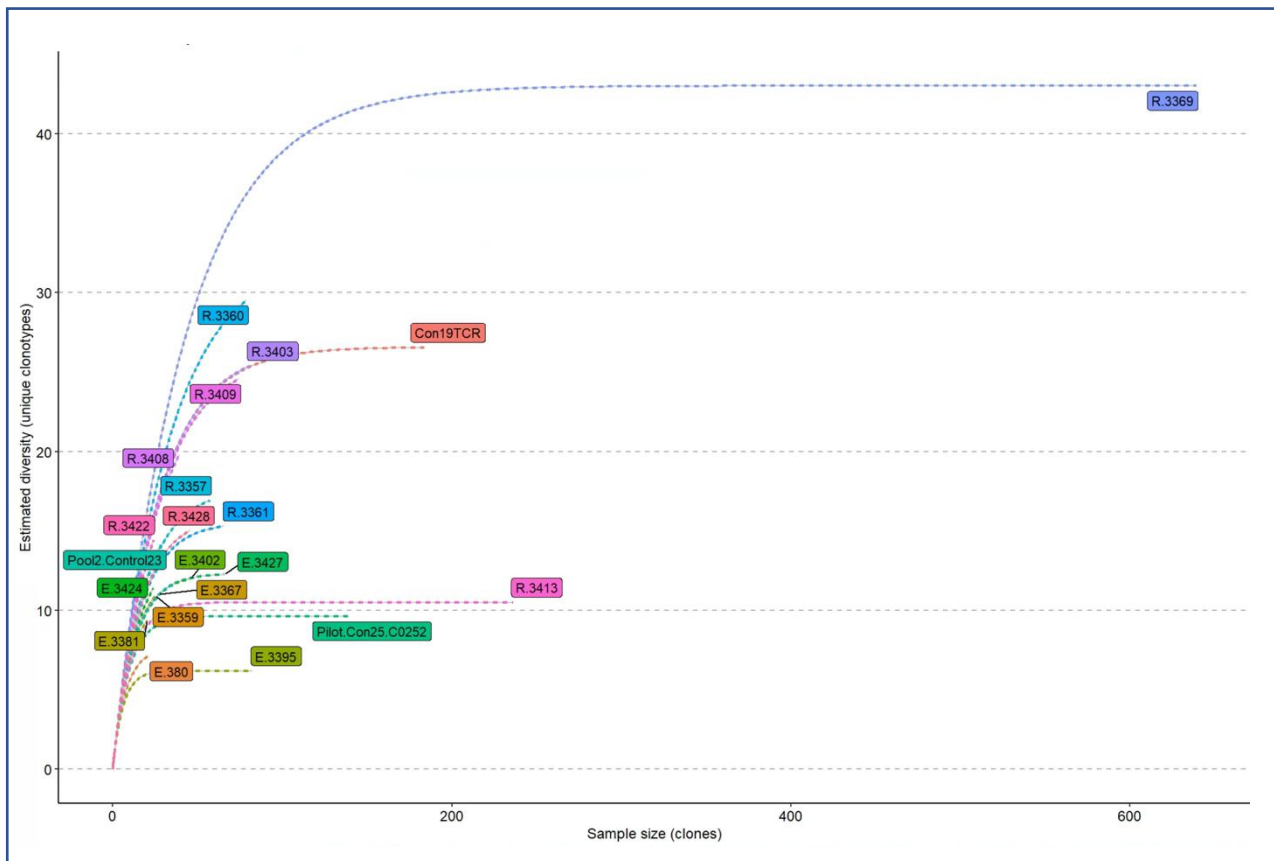


Figure 52: Rarefaction Analysis via *Immunarch* (n = 22)

10.3 Public Clonotype Analysis

Figure 53 below portrays the number of clonotypes that overlap when comparing the full TCR repertoire patient per patient using a mosaic heatmap. The 'NA' blocks of the mosaic indicate where a patient is in line to be compared to themselves and therefore the analysis is not applicable. Four patients appear with more than 800 clonotypes publicly shared with another patient, and all these patients are of the erosional subtyping (E.3359, E.380, E.3381, and E.3424). These four erosion patients contain both male and female samples as well as both STEMI and NSTEMI subtyping as shown in **Table 5**. Five patients show a public overlap greater than 500 and less than 800 clonotypes with another patient (E.3359, E.380, R.3428, R.3403, and E.3367). E.3359 and E.380 already showed a value

of 1,082 clonotypes overlapped when compared against each other, and now patient R.3428 also shows also a high clonal overlap with these same patients.

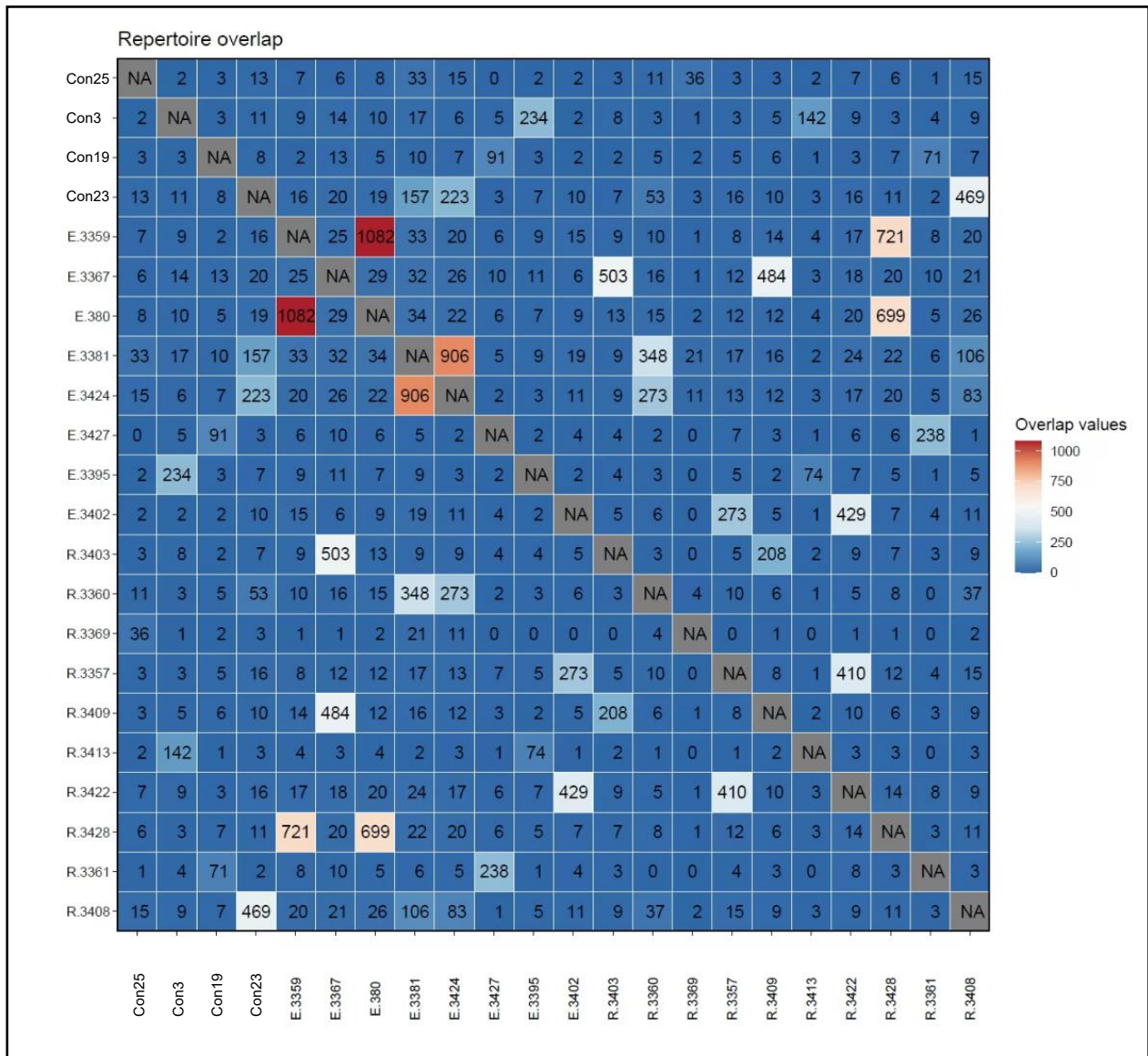


Figure 53: Overlapping Public Clonotypes via Mosaic (n = 22)

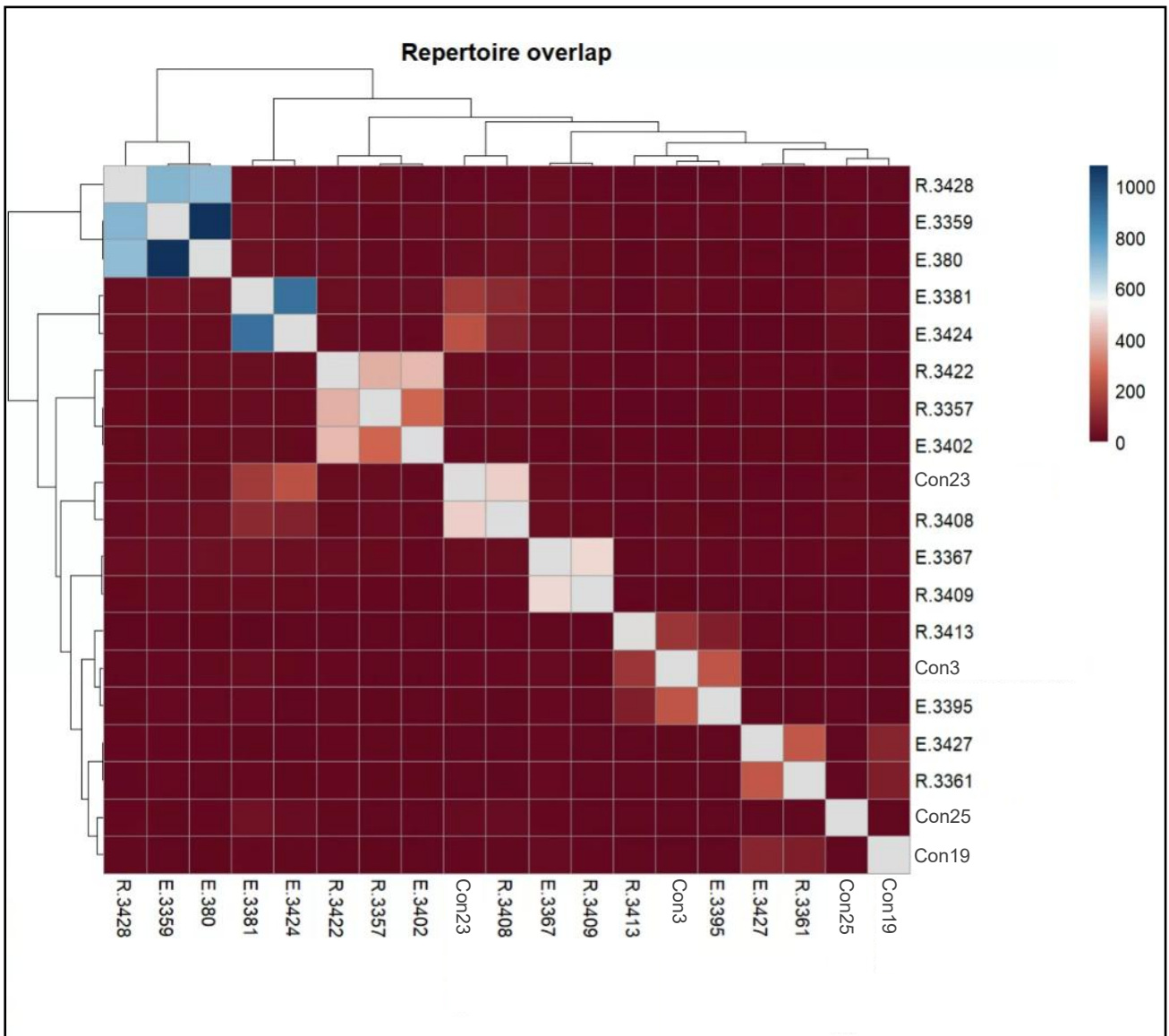


Figure 54: Overlapping Public Clonotypes via Hierarchical Heatmap (n = 22)

Above in **Figure 54**, the overlapping public clonotype information from **Figure 53** is constructed into a hierarchical heatmap. As observed previously, the patients E.3359 and E.380 are deemed very similar with the scale matching a repertoire overlap approaching 1000; however, now the hierarchical grouping has grouped patient R.3428 together with E.3359 and E.380. In a secondary grouping next to the previously mentioned group, patients E.3381 and E.3424 are found together. In a lower range of overlap, as depicted to the right by a smaller square, patients E.3381 and E.3424 also find overlap among control patient 23 (Con23) and patient R.3408.

10.4 Clustering Based on Repertoire Overlap

Using the Jaccard coefficient, in which the similarity is calculated between two finite sample sets, the TCR repertoires of each patient may be investigated and compared via each patient¹²¹. These coefficients may then be compiled using the *Immunarch* R package to form a t-distributed stochastic neighbor embedding (TSNE) map, which is similar in use to a UMAP¹²². As seen in **Figure 55** below, the patient TCR repertoires formed separated clusters depending on their Jaccard coefficient and pairwise affinity to each other. As seen in a dotted blue line, erosion patients E.380, E.3402, E.3395, and E.3423 clustered as a unique erosional-only shared global clonotype cluster.

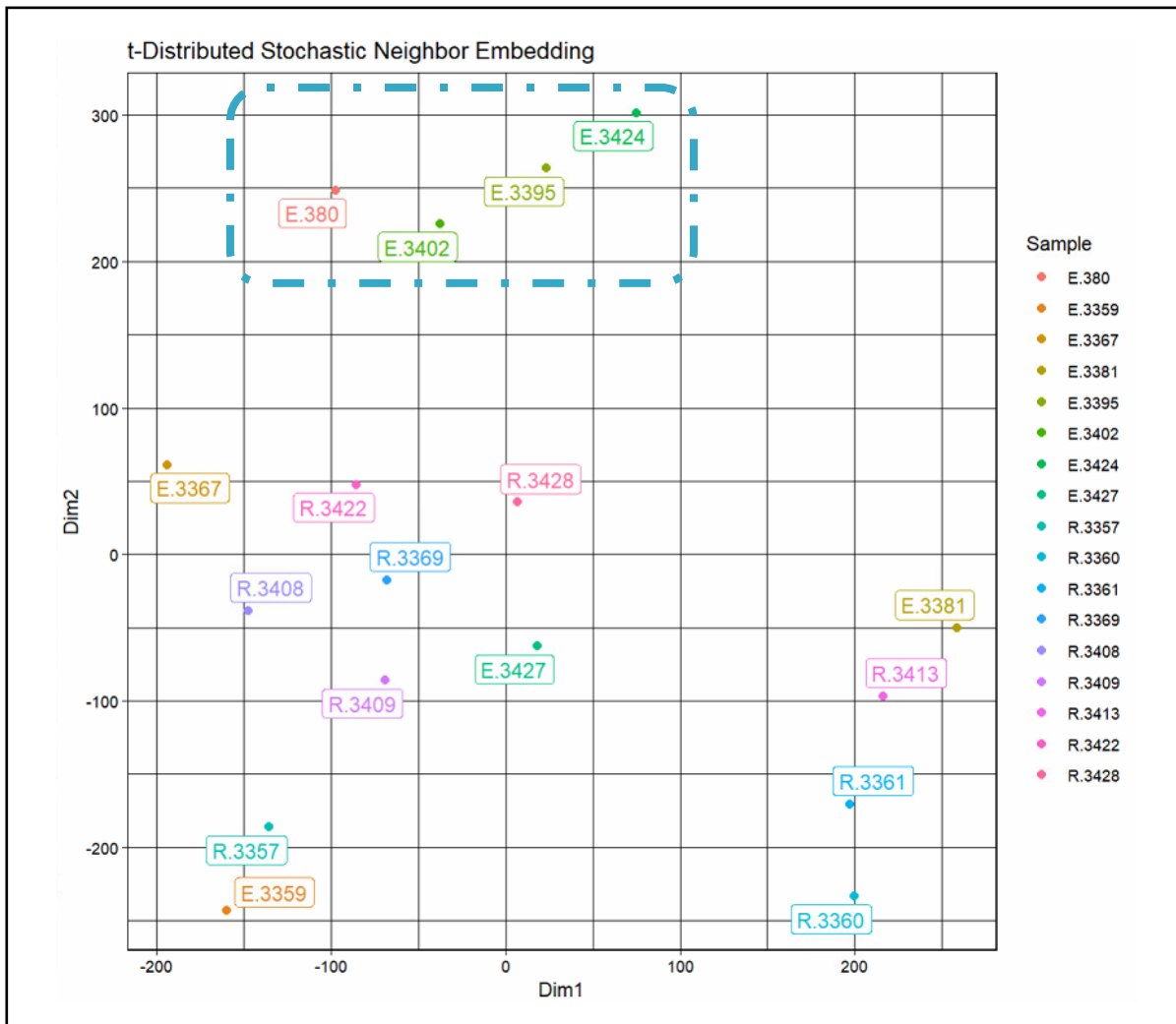


Figure 55: Natural Clustering TCR Repertoires using TSNE

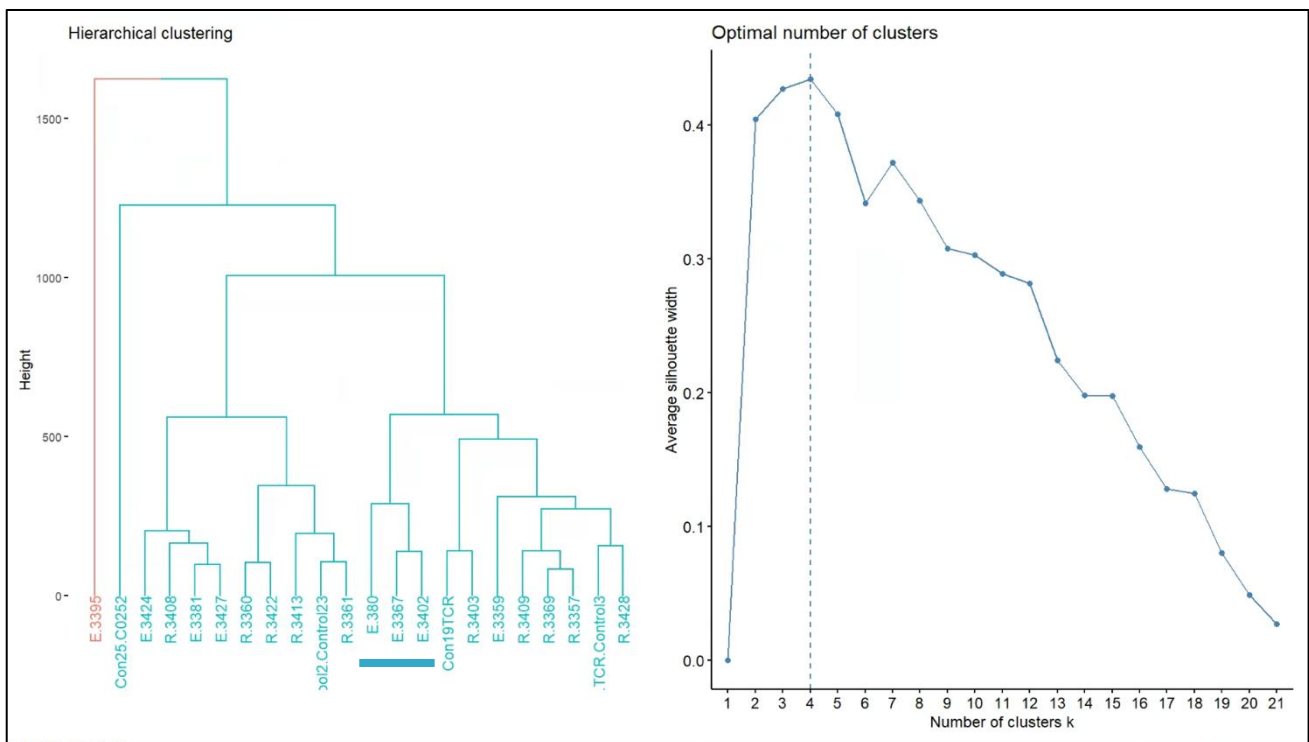


Figure 56: Hierarchical Clustering of Patients based on TCR Repertoire Affinities

In **Figure 56**, a hierarchical clustering of patients based on TCR repertoire affinities may be seen, as well as the prediction of optimal clusters via k-means. Interestingly, patient E.3395, in which contributed many T-cells (4,020), as seen in **Figure 41**. In addition, the optimal number of clusters via k-means for the patient cohort was four; however no four patients appear to k-cluster based on the patient subtype. As depicted by the thick blue line, patients E.380, E.3367, and E.3402 cluster together. As shown in **Table 9** below, 30 clonotypes for the erosional subgroup are shared globally amongst more than two patients. In contrast, only 10 clonotypes for the ruptured subgroup are shared globally amongst more than two patients. In addition, 6 clonotypes are shared among both rupture and erosion patients as a kind of ACS clonotype. Shared clonotypes were taken matched by CDR3 region of the TCR as well as one chain (α or β). Only erosional clonotypes had a diversity region (DV5).

Table 9: CDR3 Sequences of Public Clonotypes Shared by More than Two Patients

Rupture CDR3 (n = 10)	α & β V	Patients	Erosion CDR3 (n = 30)	α & β V/D	Patients
CAVRDSNYQLIW	TRAV1-2	7	CAVLDSNYQLIW	TRAV1-2	6
CAVMDSNYQLIW	TRAV1-2	6	CAVMDSNYQLIW	TRAV1-2	6
CAALDSNYQLIW	TRAV1-2	4	CAVRDSNYQLIW	TRAV1-2	6
CASSVDGNNYGYTF	TRBV10-2	3	CAAMDSNYQLIW	TRAV1-2	5
CAVKDSNYQLIW	TRAV1-2	3	CAVNQAGTALIF	TRAV12-2	5
CAVLDSNYQLIW	TRAV1-2	3	CAVSDSNYQLIW	TRAV1-2	5
CAVNQAGTALIF	TRAV12-2	3	CAVTDSNYQLIW	TRAV1-2	5
CAVRDGDYKLSF	TRAV1-2	3	CAASAAGNTPLVF	TRAV29/DV5	4
CAVSDSNYQLIW	TRAV1-2	3	CAVKDSNYQLIW	TRAV1-2	4
CVVSDRGSTLGRLYF	TRAV10	3	CAALDSNYQLIW	TRAV1-2	3
			CAASDRGSTLGRLYF	TRAV29/DV5	3
			CAASETSYDKVIF	TRAV13-1	3
			CAATDSNYQLIW	TRAV1-2	3
			CAENAGGTSYGKLTf	TRAV13-2	3
			CAENQAGTALIF	TRAV13-2	3
Both CDR3 (n = 6)			CAENTGGFKTIF	TRAV13-2	3
CAVLDSNYQLIW	TRAV1-2	10	CAGQLGSGGSNYKLTF	TRAV35	3
CAVMDSNYQLIW	TRAV1-2	12	CASSLLGTDtQYF	TRBV5-6	3
CAVRDSNYQLIW	TRAV1-2	9	CATVPMDSNYQLIW	TRAV17	3
CAAMDSNYQLIW	TRAV1-2	7	CAVEDSNYQLIW	TRAV1-2	3
CAVNQAGTALIF	TRAV12-2	8	CAVIDSNYQLIW	TRAV1-2	3
CAVSDSNYQLIW	TRAV1-2	8	CAVMDSNYQLIW	TRAV1-2	3
			CAVNTGNQFYF	TRAV12-2	3
			CAVRDGDYKLSF	TRAV1-2	3
			CAVRGGSYIPTF	TRAV12-2	3
			CAVSANTGNQFYF	TRAV8-4	3
			CAVSGYSTLTF	TRAV12-2	3
			CAVVDSNYQLIW	TRAV1-2	3
			CIVRVNSGGSNYKLTF	TRAV26-1	3
			CVVSDRGSTLGRLYF	TRAV10	3

DISCUSSION

Since its first description back in 1786, 237 years have passed investigating the roles and mechanisms of what *angina pectoris* is. As technological advancements such as ECG and OCT progress the understanding and treatment of coronary artery diseases, further resolutions into the scientific mechanisms divergences of said mechanisms are required to improve patient outcomes. The global burden of ACS carries significant implications for public health, quality of life, and socioeconomic costs. In 2017, ACS accounted for an estimated 9.5 million global deaths, comprising 16% of all yearly fatalities¹³. The total economic burden of ACS is \$150 billion in the United States annually with a direct medical cost estimated at \$75 billion¹⁴. Yet, an epidemiological transition for low- and middle-income countries as they continue to grow economically and undergo lifestyle changes warrants concern, especially for populations not typically associated with coronary artery disease such as younger adults and women.

The exact molecular and cellular events triggering endothelial disruption and subsequent plaque erosion remain subjects of ongoing research. Therefore, it is clear that the next step in investigation is to further the resolution of immune archetypes of these patients in hopes of finding new outlooks for translational research.

Chapter 11. Discussing Mechanisms of Plaque Rupture & Plaque Erosion

11.1 T-Cell Enrichment

Via the construction of an integrated CITE-seq atlas of 22 patients, the immune cell frequencies of these patients were able to be contrasted against 31 unique cluster annotations as anchored by the *Azimuth* software. The immune cells with significant enrichment, when comparing between plaque erosion and rupture, were T-cells. The T-cells that statistically differed between the erosional and ruptured subgroups were CD8⁺ T_{EM}, CD4⁺ T_{CM}, CD4⁺ T_{EM}, $\gamma\delta$ T, and Tregs (p-values: 0.020678, 0.033409, 0.007, 0.006, 0.037443, respectively).

Aside from T-cells, when conducting a group-wise differential expression analysis of the CiteSeq-C antibody panel, the CD45RA antibody was significantly differentially expressed on rupture cells as opposed to erosional cells ($p < 0.001$). CD45RA, otherwise known as protein tyrosine phosphatase receptor type C (PTPRC), was found upregulated in ruptured proliferating natural killer cells as opposed to erosion. As CD45RA is typically associated with naïve or less-differentiated immune cells, this might depict a more rapid and nonspecific response.

To focus further on T-cells, sub-clustering and anchoring to the Monaco et al. T-cell specific reference library allowed for a higher 15-cluster T-cell resolution. Interestingly, naïve CD4⁺ T-cells were enriched in rupture as opposed to erosional CD4⁺ T-cells ($p = 0.0412$). The significant prevalence of CD4⁺ naïve cells in plaque rupture patients suggests an earlier or more initial immune response, likely triggered by newly exposed plaque components during the rupture event. Interestingly, patients with chronic coronary syndrome exhibited the highest levels of CD4⁺ naïve T-cells, as seen in **Figure 39**, implying prolonged immune surveillance with persistent immune challenges that recruits more naïve cells into production. For the case of plaque rupture, notably, elevated creatine kinase levels ($p = 0.043$) in plaque rupture patients indicate more significant cardiac muscle damage.

However, it is the enrichment of CD4⁺ terminal effector T cells in plaque rupture that truly underscores the acute nature of this event compared to potentially more chronic processes in plaque

erosion. CD4⁺ terminal effector T cells, mature and relatively short-lived, likely contribute to the acute phase of the immune response following plaque rupture. Our analysis also revealed an intriguing finding: although CD4⁺ T_{TE} cells exhibited enrichment, CD8⁺ T_{TE} cells did not. Instead, the only hyperexpanded clones (1-10% of the entire repertoire) were identified in CD8⁺ terminal effector T cells, a remarkable observation in the context of plaque rupture.

The presence of hyperexpanded CD8⁺ terminal effector clonotypes would signify a potent and focused cytotoxic T-cell response. These clonotypes, arising from the proliferation of T-cells with specificity for antigens, likely denote a localized immune effort aimed at clearing infected or damaged cells within the ruptured plaque. Similarly, the hyperexpansion of $\gamma\delta$ T cells in the context of plaque rupture highlights their unique antigen recognition capabilities and responsiveness to signals associated with tissue damage⁴⁵. Their presence suggests a distinct immune response to the acute injury caused by plaque rupture, potentially contributing to inflammation and tissue repair processes. In the case of hyperexpanded T-cells, however, only two rupture patients were found to have hyperexpanded cells. Therefore, this data could also reflect a confounding immune response such as by viral infection.

T_{H17} cells, a subset of CD4⁺ T cells, are known for their hallmark production of interleukin-17 (IL-17) and play a pivotal role in the immune system's response to various challenges. In 2005, T_{H17} cells were identified as a novel subset away from T_{H1} and T_{H2} subsets¹²³. Later, T_{H17} cells were found to play a critical role in host defense against pathogens¹²⁴. While T_{H1} cells are primarily involved in role defense against intracellular pathogens, such as viruses and intracellular bacteria, T_{H17} cells are more associated with host defense against extracellular pathogens, such as fungi and certain bacteria¹²⁴. They aid in maintaining mucosal immunity and contribute to immune responses at barrier surfaces like the gut and skin¹²⁴. In contrast, T_{H2} cells promote B-cell activation and are involved in allergic responses and anti-parasitic immune reactions¹²⁵.

In the context of autoimmune disease, T_{H17} cells have garnered significant attention in the context of autoimmune diseases due to their known contributions to excessive inflammation and tissue damage are well-documented¹²⁶. In rheumatoid arthritis, T_{H17} cells have been shown to amplify the inflammatory cascade, leading to joint damage and disease progression¹²⁷. In addition, in multiple sclerosis, these cells are believed to drive neuroinflammation and demyelination, contributing to the clinical manifestations of the disease¹²⁸. In psoriasis, T_{H17} cell activation and the resultant IL-17 production are key contributors to the development of skin lesions and inflammation¹²⁹.

Beyond autoimmunity, T_{H17} cells are integral in defending against extracellular pathogens and maintaining mucosal immunity. However, when these cells malfunction, they can contribute to chronic infections and inflammatory bowel diseases. Paradoxically, T_{H17} cells have demonstrated the potential to promote anti-tumor immunity by recruiting immune cells to tumor microenvironments. Nevertheless, the pro-inflammatory functions of T_{H17} cells are also associated with chronic inflammation, a hallmark of cancer progression¹³⁰.

Remarkably, the current investigation reveals a notable enrichment of T_{H17} cells in erosional ACS when compared to patients with chronic coronary syndrome and those with ruptured plaque-associated ACS ($p = 0.019$ and $p = 0.008$, respectively). While T_{H17} cells are traditionally recognized for their pro-inflammatory characteristics, it is intriguing to observe that patients with ruptured plaques show an enrichment of CD4⁺ naïve and CD4⁺ terminal effector (T_{TE}) cells. CD4⁺ naïve T-cells represent a subset that has not yet encountered their specific antigen, while CD4⁺ T_{TE} cells are mature, with relatively short lifespans, typically generated during the acute phase of an immune response.

Curiously, depending on the annotation library employed, Tregs were positively enriched in the erosional cohort using Azimuth analysis, although not significantly enriched using the Monaco database¹¹⁰. This presents a puzzle worth exploring. One possible explanation lies in the plasticity of

T_{H17} cells and their ability to convert into Tregs. Given that the Monaco reference includes both T_{H17} cells and Tregs in its annotations while *Azimuth* lacks a specific annotation for T_{H17} cells, it is conceivable that the *Azimuth* database assigned T_{H17} cells as Tregs for the best possible fit. This could imply that the T_{H17} cells within the erosional plaque context exhibit characteristics resembling Tregs, as interpreted by the *Azimuth* prediction software.

It is crucial to emphasize that Treg-to-T_{H17} cell plasticity has been strongly implicated in autoimmune diseases, where this phenomenon could exacerbate inflammation and contribute to tissue damage¹³¹. Furthermore, the enrichment of T_{H1}-T_{H17} cells in erosional plaques compared to patients with chronic coronary syndrome is noteworthy ($p = 0.0392$, 95% CI 0.155 – 0.165). When assessing the clonal expansion levels of these T_{H17} cells, an intriguing finding emerges: the majority of these cells fall within the category of small expansion rates, ranging from 0 to 0.01%.

However, what is particularly striking is that erosional T_{H17} cells exhibit approximately double the number of clonotypes compared to those in ruptured plaques (**Figure 48**). Despite these intriguing findings, our rarefaction analysis for diversity revealed that erosional patients' T-cells exhibited reduced diversity, characterized by fewer unique clonotypes compared to those in ruptured plaques (**Figure 51**). This unique immune landscape in erosional ACS, marked by the enrichment of T_{H17} cells and distinct T-cell dynamics, underscores the complex interplay of immune responses in atherosclerotic plaques.

11.2 Cell Adhesion in Erosional Plaque

Interestingly, the upregulation of the cell surface protein Integrin $\alpha 6$, encoded by the *ITGA6* gene, was observed in erosional T cells relative to those in ruptured plaques and control samples as seen in **Figure 43**. Integrin $\alpha 6$ combines to form a heterodimeric receptor called $\alpha 6\beta 1$ integrin (or CD49f/CD29), as it of particular importance for cell adhesion to laminin-rich structures such as blood vessels. This upregulation of Integrin $\alpha 6$ was particularly pronounced in T_{H17} and T_{H2} cells, indicating a potential association between this surface protein, cell adhesion to laminin-rich structures, and specific T-cell subsets.

Furthermore, when DE markers of erosional T_{H17} cells as compared to rupture we put through GO term analysis, GO terms for cell junction ($p = 1.050e^{-6}$), anchoring junction, cell-substrate junction ($p = 3.597e^{-13}$) and focal adhesion ($2.128e^{-13}$) were found to be significantly enriched in erosional T_{H17} cells as opposed to rupture T_{H17} cells. These findings suggest a molecular signature marked by enhanced cell adhesion and interactions with the extracellular matrix, potentially altering cell-cell contacts within T_{H17} cells in plaque erosion.

Of particular significance is the enrichment of genes related to focal adhesion, indicating that T_{H17} cells in plaque erosion may possess an increased capacity to interact with the arterial wall's extracellular matrix components. This enhanced adhesion may facilitate their recruitment to the site of inflammation, chronic inflammation, and tissue remodeling within the coronary artery. Moreover, these T_{H17} cells may efficiently migrate through arterial wall layers, activating intracellular signaling pathways and sensing mechanical cues through mechanotransduction, influencing their behavior and perpetuating the inflammatory response. These findings suggest an augmented capacity for adhesion, interactions with the vascular endothelium, and engagement with the extracellular matrix (ECM) in plaque erosion T_{H17} cells. These molecular characteristics align with established pathophysiological mechanisms of plaque erosion, specifically the detachment of endothelial cells from the arterial wall.

This enhanced adhesion may also facilitate the recruitment of immune cells to the site of plaque erosion, contributing to the chronic inflammatory environment characteristic of this condition. Additionally, it implies a potential role for these immune cells in the detachment of endothelial cells

from the arterial wall, a hallmark of plaque erosion-associated endothelial dysfunction. The involvement of Integrin $\alpha 6$ in cell migration and tissue remodeling suggests that immune cells may actively participate in modifying the extracellular matrix within erosional plaques, thereby contributing to tissue remodeling processes observed in this context. This theory is furthermore supported by the known role of certain MMPs and endothelial structural destabilization via the ECM ⁶⁷.

11.3 TCR Signal Amplification

Transmembrane immune signaling adaptor or *TYROBP* was found to be significantly upregulated in erosional T_{H17} cells as compared to ruptured T_{H17} cells ($p < 0.001$; $\text{Log2FC} = 3.33$). The gene *TYROBP* encodes for a transmembrane signaling polypeptide which contains an immunoreceptor tyrosine-based activation motif (ITAM). ITAMs are conserved motifs found on certain cell surface receptors, including the TCR complex. Both the α and β chains of TCR contain ITAMs.

This ITAM containing protein can therefore bind to zeta-chain (TCR) associated protein kinase 70kDa (ZAP-70). ZAP-70 is an incredibly important protein tyrosine kinase that plays a critical role in T-cell signaling. After a TCR binds to an antigen, phosphorylated ITAMs serve as a docking site for ZAP-70. Once ZAP-70 is phosphorylated itself, a signaling cascade is initiated and induces the expression of genes responsible for T-cell activation, proliferation, and cytokine production. In **Figure 57** below, the phosphorylation of ZAP-70 is shown as required to initiate TCR signaling ¹³².

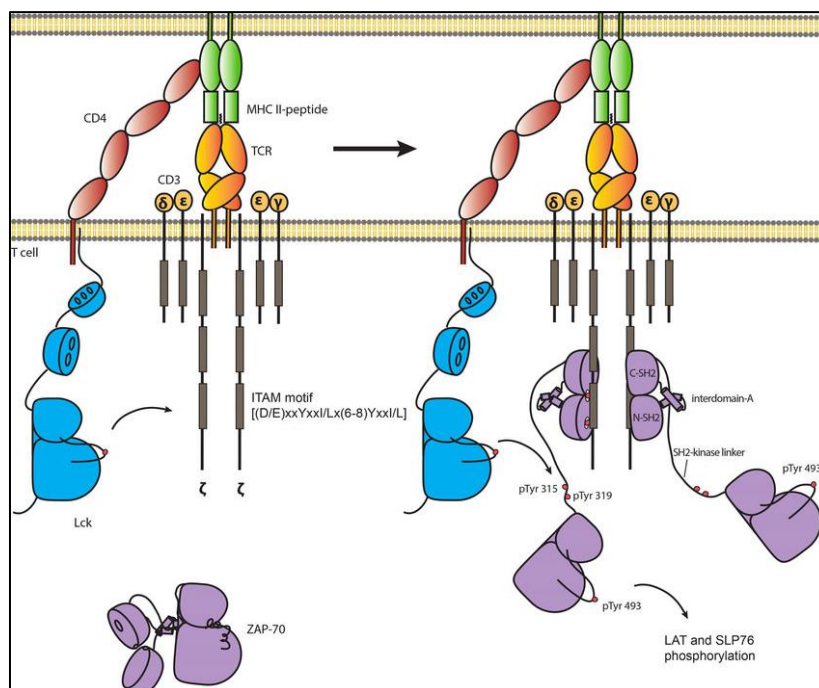


Figure 57: ZAP-70 Phosphorylation ¹³²

11.4 Shared Global Clones and Diversity

The observation that erosional T-cells exhibit a higher prevalence of shared global clones and lower diversity compared to ruptured T-cells unveils distinct immune dynamics within these two subgroups of atherosclerotic plaque pathology. This finding suggests that individuals with erosional plaques may have encountered common antigenic stimuli or triggers that led to the clonal expansion of specific T cell populations. This shared clonality implies a more uniform immune response among patients with plaque erosion, aligning with the notion of autoimmune-like features within atherosclerosis. Conversely, the diversity of T-cells in ruptured plaques indicates a heterogeneous response. However, the presence of hyperexpanded CD8⁺ terminal effector clonotypes underscores the complexity of the immune environment in these patients. This alignment of T-cell diversity with T_{H17} cells and autoimmunity raises intriguing questions about the potential autoimmune aspects of atherosclerosis and the intricate interplay between T-cell populations in driving both inflammation and tissue damage within the plaque microenvironment.

11.5 Therapeutic & Genetic Testing Implications

The enrichment of T_{H17} cells in erosional ACS raises the possibility of developing specific therapies that modulate these immune cells. Given their known role in autoimmune diseases and chronic inflammation, targeting T_{H17} cells could be a promising approach to mitigate the inflammatory processes associated with plaque erosion. Further research is needed to explore the feasibility of such interventions and their potential impact on plaque stability. In addition, the upregulation of integrin $\alpha 6$ in erosional T cells suggests its potential as a biomarker for identifying individuals at risk of erosional plaque-related coronary artery disease. This surface protein's role in cell adhesion and interactions with the extracellular matrix may contribute to the development of novel diagnostic tests or genetic markers to identify patients prone to plaque erosion. Future studies should investigate the clinical utility of Integrin $\alpha 6$ as a predictive marker.

The observed differences in immune cell dynamics between plaque erosion and rupture underscore the importance of tailoring treatment strategies to the specific mechanisms of each condition. As our understanding of these immune responses deepens, there is a growing potential for personalized approaches based on the underlying pathology. Such personalized treatments could enhance outcomes for patients with ACS, addressing the nuanced mechanisms of erosional and ruptured plaque for more effective interventions. Finally, Genetic testing, particularly for variations associated with immune responses, may play a role in assessing an individual's susceptibility to different ACS mechanisms. Understanding the genetic factors that predispose individuals to plaque rupture or erosion could enable risk stratification and early intervention. Collaborative efforts between geneticists and cardiologists could lead to the development of genetic risk assessment tools tailored to different ACS subtypes.

Summary

In this study, advanced sequencing techniques, specifically CITE-seq and VDJ-seq, were employed to construct an integrated atlas encompassing three distinct single-cell resolution modalities—without the need for custom RT primers. The primary objective was to delve into the contrasting features of erosional and ruptured acute coronary syndromes (ACS) through a multi-omics approach.

Through meticulous bioinformatic processing and the amalgamation of multiple single-cell sequencing datasets, this investigation unearthed a notable enrichment of T_{H17} cells in erosional ACS when compared to rupture and chronic coronary syndrome. This discovery, coupled with the observed enrichment of ruptured CD4⁺ T_{TE} cells relative to erosion, hints at the multifaceted roles that T-cells play in both rupture and erosion mechanisms. Furthermore, these findings offer potential insights into the importance of Integrin α 6 and cell adhesion dynamics for T_{H17} cells functions, the role of common antigen exposure in erosional plaque as well as overzealous erosional T_{H17} ITAMs, all of which warrant in-depth exploration regarding their implications in coronary artery disease.

Although substantial work remains to validate ACS-specific biomarkers for preventative medications targeting erosional and rupture plaques in coronary artery disease, the outcomes of this investigation, along with the invaluable resource of a comprehensive atlas, provide valuable clues for the next phase of multi-omics research into acute coronary syndromes.

Limitations

One notable limitation of this study pertains to the cohort sample size, which consisted of 22 individuals and 24 samples subjected to sequencing. While this sample size was sufficient for initial insights, it may not fully capture the complexity and diversity of the broader population affected by acute coronary syndromes. The sequencing process encountered practical challenges, primarily related to sample batching. Initially, an attempt was made to sequence all samples in a single batch; however, this approach proved unviable due to the time-consuming nature of preparing and pooling samples while maintaining cellular vitality. Consequently, batch effects became a significant limitation in the data analysis.

To mitigate the impact of batch effects, extensive bioinformatic efforts were undertaken, including the utilization of *DSB* correction techniques. Despite these efforts, it remains essential to acknowledge that some level of batch effects may persist, potentially influencing the interpretation of results. Additionally, the limitation of sample size hampers the ability to draw robust conclusions, particularly in comparisons between peripheral and coronary samples.

An important future consideration is the lack of human leukocyte antigen-DR (HLA-DR) isotyping of patients, which was not included in the current study. Incorporating this information in the future could enhance our understanding of the specific immune profiles associated with ACS patients while also considering patient genetic diversity.

Another large limitation of this study was the cryopreservation of the samples. As the cells were non-stimulated to avoid any bias in activation phenotypes, the only viable option to continue exploration at higher resolutions was via training from other manually assigned single cell libraries. In addition, cryopreservation is known to affect the readout of PBMCs for single cell sequencing. Unfortunately, as this was a follow-up to a FACS investigation, the patients were no longer under recruitment. However, this approach to not stimulate the PBMCs have thawing comes with its own

trade-offs. While it facilitates comparisons with other researchers' data using methods like *SingleR*, the lack of cell stimulation means that the atlas represents cells in a resting state, free from the potential biases introduced by cell culture and stimulation. This choice also sidesteps any potential biases that might arise due to antigen expression changes or cellular activation following thawing and incubation.

Finally, the selection of a CITE-Seq + VDJ-Seq custom sequencing technique for this study introduced its own set of limitations. Notably, without custom RT primers, this study required several runs of research and development to work around the previously mentioned technological limitations. In addition, as CITE-Seq is a relatively new technique, the lack of robust quality control for the antibody panel limited scientific interpretation.

Outlook

This investigation's findings shed light on significant differences in the expression of key genes in T_{H17} cells between erosional and ruptured plaques. *TYROBP*, a molecule involved in immune cell activation and signaling, showed substantial upregulation in erosional T_{H17} cells. These observed alterations in *TYROBP* levels prompt intriguing questions about functional implications within the context of plaque stability and rupture. The upregulation of *TYROBP* in erosional T_{H17} cells may signify heightened immune activation and signaling pathways. *TYROBP* is associated with various immune functions, including antigen presentation and cytokine production¹¹⁸. Its increased expression in erosional plaque T_{H17} cells may indicate an enhanced capacity for immune responses within these plaques. Exploring the specific pathways and interactions involving *TYROBP* in this context could provide valuable insights into the immune mechanisms underlying plaque erosion.

In addition, Integrin alpha6, encoded by the *ITGA6* gene, has emerged as a potential biomarker of interest, holding the potential to serve as a specific marker or genetic test for identifying individuals at risk of erosional plaque-related coronary artery disease. Further exploration of this marker, its functional implications, and its clinical utility could yield valuable insights for risk assessment and personalized medicine in ACS.

Moreover, the field of T-cell receptor research is poised for continued advancement. Functional studies aimed at deciphering how specific TCRs recognize and respond to antigens represent an exciting avenue. Technologies such as peptide-major histocompatibility complex tetramers, enable the identification and isolation of T-cells with defined antigen specificities. This ability to define antigen specificities, offers a deeper understanding of T-cell responses and their connection to any common antigens¹³³. Structural biology methods, including X-ray crystallography and cryo-electron microscopy, allow for the visualization of TCR-antigen-MHC interactions at the atomic level, providing crucial insights into the molecular basis of antigen recognition¹³³.

As the understanding of the immune system and its role in contrary artery diseases continues to improve, further innovative technologies are needed, such as via new unique ways of single-cell sequencing, to aid in the discovery of novel biomarkers, therapeutic targets, and diagnostic tools. These future endeavors hold the promise of translating research findings into practical applications that improve patient care and outcomes in the realm of acute coronary syndromes.

REFERENCES

1. De Vore, L, et al. "Investigations in Plaque Erosion and Ruptured in Acute Coronary Syndromes via Novel Methods in Multimodal and VDJ Sequencing." *European Heart Journal*, 2022.
2. Kligfield, P. *Heart Disease: A textbook of Cardiovascular Medicine*, 5/E, edited by Eugene Braunwald, W.B. Saunders, Philadelphia (1997)
3. Klatsky, A. L. Alcohol and cardiovascular diseases: A historical overview. *Novartis Foundation Symposium* 2–18 (1998). doi:10.1007/978-94-011-4307-3_1
4. Kushner, F. G. et al. 2009 Focused Updates: ACC/AHA Guidelines for the Management of Patients With ST-Elevation Myocardial Infarction (Updating the 2004 Guideline and 2007 Focused Update) and ACC/AHA/SCAI Guidelines on Percutaneous Coronary Intervention (Updating the 2005 Guideline and 2007 Focused Update). *Journal of the American College of Cardiology* 54, 2205–2241 (2009).
5. Thygesen, K. et al. Fourth Universal Definition of Myocardial Infarction (2018). *Circulation* 138, e618–e651 (2018).
6. Amsterdam, E. A. et al. 2014 AHA/acc guideline for the management of patients with Non-ST-Elevation acute coronary syndromes: A report of the American College of Cardiology/American Heart Association Task Force on Practice Guidelines. *Journal of the American College of Cardiology* 64, e139–e228 (2014).
7. Pleister, Adam & Selemon, Helina & Elton, Shane & Elton, Terry. (2013). Circulating miRNAs: Novel biomarkers of acute coronary syndrome?. *Biomarkers in medicine*. 7. 287-305. 10.2217/bmm.13.8.
8. Sherry, S. The origin of thrombolytic therapy. *Journal of the American College of Cardiology* 14, 1085–1092 (1989).
9. Canfield, J. & Totary-Jain, H. 40 years of percutaneous coronary intervention: History and future directions. *Journal of Personalized Medicine* 8, (2018).
10. Farb, A. et al. Coronary plaque erosion without rupture into a lipid core: A frequent cause of coronary thrombosis in sudden coronary death. *Circulation* 93, 1354–1363 (1996).
11. Jang, I. K. et al. In vivo characterization of coronary atherosclerotic plaque by use of optical coherence tomography. *Circulation* 111, 1551–1555 (2005).
12. Fahed, A. C. & Jang, I. K. Plaque erosion and acute coronary syndromes: phenotype, molecular characteristics and future directions. *Nature Reviews Cardiology* 18, 724–734 (2021).
13. WHO, W. H. O. *Global Health Estimates 2016*. Geneva : World Health Organization 2000–2016 (2018).
14. Kolansky, D. M. Acute coronary syndromes: morbidity, mortality, and pharmacoeconomic burden. *The American journal of managed care* 15, (2009).

15. Vedanthan, R., Seligman, B. & Fuster, V. Global perspective on acute coronary syndrome: A burden on the young and poor. *Circulation Research* 114, 1959–1975 (2014).
16. Murray, C. et al. Global, regional, and national life expectancy, all-cause mortality, and cause-specific mortality for 249 causes of death, 1980–2015: a systematic analysis for the Global Burden of Disease Study 2015. *The Lancet* 388, 1459–1544 (2016).
17. Libby, P., Theroux, P., & Mohler, E. R. (2019). Acute coronary syndromes: Pathogenesis, diagnosis, and risk stratification. In Bonow, R. O., Mann, D. L., Zipes, D. P., & Libby, P. (Eds.), *Braunwald's Heart Disease: A Textbook of Cardiovascular Medicine* (11th ed., pp. 1122-1184). Elsevier.
18. Yusuf, S., Hawken, S., Ôunpuu, S., Dans, T., Avezum, A., Lanas, F., ... & Lisheng, L. (2004). Effect of potentially modifiable risk factors associated with myocardial infarction in 52 countries (the INTERHEART study): Case-control study. *The Lancet*, 364(9438), 937-952.
19. Fuster, V., Kelly, B. B., & Vedanthan, R. (2012). Global cardiovascular health: Urgent need for an intersectoral approach. *Journal of the American College of Cardiology*, 60(20), 2030-2037.
20. Prabhakaran, D., Jeemon, P. & Roy, A. Cardiovascular Diseases in India: Current Epidemiology and Future Directions. *Circulation* 133, 1605–1620 (2016).
21. Chandrasekhar, J., Gill, A. & Mehran, R. Acute myocardial infarction in young women: Current perspectives. *International Journal of Women's Health* 10, 267–284 (2018).
22. Dreyer, R. P. et al. Young Women With Acute Myocardial Infarction: Current Perspectives. *Circulation. Cardiovascular quality and outcomes* 10, (2017).
23. Bentzon, J. F., Otsuka, F., Virmani, R. & Falk, E. Mechanisms of plaque formation and rupture. *Circulation Research* 114, 1852–1866 (2014).
24. Amsterdam, E. A., Wenger, N. K., Brindis, R. G., Casey, D. E., Ganiats, T. G., Holmes, D. R., ... & Creager, M. A. (2014). 2014 AHA/ACC guideline for the management of patients with non-ST-elevation acute coronary syndromes: a report of the American College of Cardiology/American Heart Association Task Force on Practice Guidelines. *Journal of the American College of Cardiology*, 64(24), e139-e228.
25. Jia, H. et al. In vivo diagnosis of plaque erosion and calcified nodule in patients with acute coronary syndrome by intravascular optical coherence tomography. *Journal of the American College of Cardiology* 62, 1748–1758 (2013).
26. Virmani, R., Robinowitz, M., Atkinson, J. B., Forman, M. B., Silver, M. D., McAllister, H. A., & Coronary Artery Surgery Study (CASS) Registry Group. (1986). Acquired coronary artery disease in transplant recipients with normal coronary arteries: Immunologic evidence for the presence of an active immune response. *The American Journal of Medicine*, 81(4), 551-556.
27. Partida, R. A., Libby, P., Crea, F., & Jang, I. K. (2018, June 7). Plaque erosion: A new in vivo diagnosis and a potential major shift in the management of patients with acute coronary syndromes. *European Heart Journal*. Oxford University Press. <https://doi.org/10.1093/eurheartj/ehx786>

28. Luo, X. et al. Plaque Erosion: A Distinctive Pathological Mechanism of Acute Coronary Syndrome. *Frontiers in Cardiovascular Medicine* 8, (2021).
29. Noothi, S. K., Ahmed, M. R. & Agrawal, D. K. Residual risks and evolving atherosclerotic plaques. *Molecular and Cellular Biochemistry* (2023). doi:10.1007/s11010-023-04689-0
30. Libby, P. (2017). Coronary artery injury and the biology of atherosclerosis: Inflammation, thrombosis, and stabilization. *American Journal of Cardiology*, 119(6), 3-7.
31. Arbustini, E., Dal Bello, B., Morbini, P., Burke, A. P., Bocciarelli, M., Specchia, G., Virmani, R. (2018). Plaque erosion is a major substrate for coronary thrombosis in acute myocardial infarction. *Heart*, 104(12), 1231-1239.
32. Yahagi, K., Kolodgie, F. D., Otsuka, F., Finn, A. V., Davis, H. R., Joner, M., Virmani, R. (2019). Pathophysiology of native coronary, vein graft, and in-stent atherosclerosis. *Nature Reviews Cardiology*, 16(2), 79-98.
33. Pasterkamp, G., den Ruijter, H. M., Libby, P., & Tempel, D. (2019). Advances in understanding of plaque erosion. *European Heart Journal*, 40(42), 3423-3431.
34. Kato, A. et al. Physical exertion as a trigger of acute coronary syndrome caused by plaque erosion. *Journal of Thrombosis and Thrombolysis* 49, 377–385 (2020).
35. Khan, K. A., Osheiba, M., Mechery, A. & Khan, S. Q. ST-segment elevation myocardial infarction with plaque erosion, to stent or not to stent: Utility of intracoronary optical coherence tomography (OCT) imaging - A case report. *European Heart Journal - Case Reports* 6, (2022).
36. Kolte, D. et al. Optical Coherence Tomography of Plaque Erosion: JACC Focus Seminar Part 2/3. *Journal of the American College of Cardiology* 78, 1266–1274 (2021).
37. Khan, K. A., Osheiba, M., Mechery, A. & Khan, S. Q. ST-segment elevation myocardial infarction with plaque erosion, to stent or not to stent: Utility of intracoronary optical coherence tomography (OCT) imaging - A case report. *European Heart Journal - Case Reports* 6, (2022).
38. Abubakar M, Javed I, Rasool HF, Raza S, Basavaraju D, Abdullah RM, Ahmed F, Salim SS, Faraz MA, Hassan KM, Hajjaj M. Advancements in Percutaneous Coronary Intervention Techniques: A Comprehensive Literature Review of Mixed Studies and Practice Guidelines. *Cureus*. 2023 Jul 3;15(7):e41311. doi: 10.7759/cureus.41311. PMID: 37539426; PMCID: PMC10395399.
39. Xing, L. et al. EROSION Study (Effective Anti-Thrombotic Therapy Without Stenting: Intravascular Optical Coherence Tomography-Based Management in Plaque Erosion): A 1-Year Follow-Up Report. *Circulation: Cardiovascular Interventions* 10, (2017).
40. Libby, Peter. Inflammation and cardiovascular disease mechanisms. *The American journal of clinical nutrition* vol. 83,2 (2006): 456S-460S. doi:10.1093/ajcn/83.2.456S.
41. Virchow, R. As Based upon Physiological and Pathological Histology: Cellular Pathology. *Nutrition Reviews* 47, 23–25 (1989).
42. Jonasson, L., Holm, J., Skalli, O., Bondjers, G. & Hansson, G. K. Regional accumulations of T cells, macrophages, and smooth muscle cells in the human atherosclerotic plaque. *Arteriosclerosis* 6, 131–138 (1986).

43. Jonasson, L., Holm, J., Skalli, O., Bondjers, G. & Hansson, G. K. Regional accumulations of T cells, macrophages, and smooth muscle cells in the human atherosclerotic plaque. *Arteriosclerosis* 6, 131–138 (1986).
44. Libby, P., Lichtman, A. H. & Hansson, G. K. Immune Effector Mechanisms Implicated in Atherosclerosis: From Mice to Humans. *Immunity* 38, 1092–1104 (2013).
45. Janeway, C., Travers, P. & Walport, M. Generation of lymphocytes in bone marrow and thymus. *Immunobiology* 5, 1–20 (2011).
46. Ansari, F. (2021, September 15). T cell development and maturation - The Virtual Notebook. The Virtual Notebook. <https://www.thevirtualnotebook.com/t-cell-development-and-maturation/>
47. Radtke, F., Fasnacht, N. & MacDonald, H. R. Notch Signaling in the Immune System. *Immunity* 32, 14–27 (2010).
48. Welten, Suzanne P. M., Cornelis J. M. Melief and Ramon Arens. “The distinct role of T cell costimulation in antiviral immunity.” *Current opinion in virology* 3 4 (2013): 475-82 .
49. Arlen, P. M., Mohebtash, M., Madan, R. A. & Gulley, J. L. Promising novel immunotherapies and combinations for prostate cancer. *Future Oncology* 5, 187–196 (2009).
50. Abbas, A. K., Lichtman, A. H., & Pillai, S. (2020). *Cellular and Molecular Immunology*. Elsevier.
51. Basu, R., Hatton, R. D. & Weaver, C. T. The Th17 family: Flexibility follows function. *Immunological Reviews* 252, 89–103 (2013).
52. Paul, W. E. (2010). *Fundamental Immunology*. Lippincott Williams & Wilkins.
53. Dutta, A., Venkataganesh, H. & Love, P. E. New insights into epigenetic regulation of T cell differentiation. *Cells* 10, (2021).
54. Szabo, P. A., & Miron, M. (2017). Effector and memory T cell subsets in the human tumor microenvironment. *Nature Immunology*, 18(10), 1-11
55. Wherry, E. J., & Kurachi, M. (2015). Molecular and cellular insights into T cell exhaustion. *Nature Reviews Immunology*, 15(8), 486-499.
56. Geginat, J., Lanzavecchia, A. & Sallusto, F. Proliferation and differentiation potential of human CD8⁺ memory T-cell subsets in response to antigen or homeostatic cytokines. *Blood* 101, 4260–4266 (2003).
57. Davis, M. M. & Bjorkman, P. J. T-cell antigen receptor genes and T-cell recognition. *Nature* 334, 395–402 (1988).
58. Robins, H. S. et al. Comprehensive assessment of T-cell receptor beta-chain diversity in alphabeta T cells. *Blood* 114, 4099–4107 (2009).
59. Ralph, D. K. & Matsen, F. A. Consistency of VDJ Rearrangement and Substitution Parameters Enables Accurate B Cell Receptor Sequence Annotation. *PLoS Computational Biology* 12, (2016).

60. Chiffelle, J. et al. T-cell repertoire analysis and metrics of diversity and clonality. *Current Opinion in Biotechnology* 65, 284–295 (2020).
61. Borchering, N., Bormann, N. L. & Kraus, G. scRepertoire: An R-based toolkit for single-cell immune receptor analysis. *F1000Research* 9, (2020).
62. Libby, P., Ridker, P. M., & Hansson, G. K. (2002). Progress and challenges in translating the biology of atherosclerosis. *Nature*, 420(6917), 868-874.
63. Gupta, S., Pablo, A. M., & Jiang, X. C. (2016). Apolipoprotein E and Atherosclerosis: From Lipoprotein Metabolism to MicroRNA Control of Inflammation. *Journal of Cardiovascular Development and Disease*, 3(4), 17.
64. Biasucci, L. M. et al. Where Does Inflammation Fit? *Current Cardiology Reports* 19, (2017).
65. Liuzzo, G. et al. Unusual CD4⁺CD28^{null} T Lymphocytes and Recurrence of Acute Coronary Events. *Journal of the American College of Cardiology* 50, 1450–1458 (2007).
66. Leistner, D. M. et al. Differential immunological signature at the culprit site distinguishes acute coronary syndrome with intact from acute coronary syndrome with ruptured fibrous cap: Results from the prospective translational OPTICO-ACS study. *European Heart Journal* 41, 3549–3560 (2020).
67. Taraboletti, G. et al. Shedding of the matrix metalloproteinases MMP-2, MMP-9, and MT1-MMP as membrane vesicle-associated components by endothelial cells. *American Journal of Pathology* 160, 673–680 (2002).
68. Zhou, X., Nicoletti, A., Elhage, R., & Hansson, G. K. (2019). Transfer of CD4⁺ T cells aggravates atherosclerosis in immunodeficient apolipoprotein E knockout mice. *Circulation*, 109(25), 2919-2922.
69. Tabas, I. & Bornfeldt, K. E. Macrophage Phenotype and Function in Different Stages of Atherosclerosis. *Circulation Research* 118, 653–667 (2016).
70. Dai, H., Thomson, A. W. & Rogers, N. M. Dendritic Cells as Sensors, Mediators, and Regulators of Ischemic Injury. *Frontiers in Immunology* 10, (2019).
71. Bot, I. et al. Perivascular mast cells promote atherogenesis and induce plaque destabilization in apolipoprotein E-deficient mice. *Circulation* 115, 2516–2525 (2007).
72. Moraes, L. A. et al. Annexin-A1 enhances breast cancer growth and migration by promoting alternative macrophage polarization in the tumour microenvironment. *Scientific Reports* 7, (2017).
73. Swirski, F. K. & Nahrendorf, M. Cardioimmunology: the immune system in cardiac homeostasis and disease. *Nature Reviews Immunology* 18, 733–744 (2018).
74. Huh, D., Gu, W., & Kamotani, Y. et al. (2005). Reconstituting Organ-Level Lung Functions on a Chip. *Science*, 328(5986), 1662-1668.
75. Li, B. et al. Droplets microfluidics platform—A tool for single cell research. *Frontiers in Bioengineering and Biotechnology* 11, (2023).

76. *Chromium Next GEM Single Cell 5' Reagent Kits v2 (Dual Index) with Feature Barcode technology for CRISPR Screening and Cell Surface Protein*, Document Number CG000511 Rev C, 10X Genomics, (January 6, 2023).
77. *Chromium Next GEM Single Cell 3' v3.1 Reagent & Workflow Updates*, Document Number CG000227 Rev C, 10X Genomics, (2019).
78. Feng, W., Przysinda, A. & Li, G. Multiplexed single cell mRNA sequencing analysis of mouse embryonic cells. *Journal of Visualized Experiments* 2020, (2019).
79. Mende, N., Laurenti, E., Göttgens, B. & Wilson, N. K. in *Methods in Molecular Biology* 2386, 189–201 (Humana Press Inc., 2022).
80. Macosko, E. Z. et al. Highly parallel genome-wide expression profiling of individual cells using nanoliter droplets. *Cell* 161, 1202–1214 (2015).
81. Cao, J. et al. Comprehensive single-cell transcriptional profiling of a multicellular organism. *Science* 357, 661–667 (2017).
82. Cock, P. J. A. et al. Biopython: Freely available Python tools for computational molecular biology and bioinformatics. *Bioinformatics* 25, 1422–1423 (2009).
83. Ewing, B., Hillier, L., Wendl, M. C., & Green, P. (1998). Base-calling of automated sequencer traces using phred. I. Accuracy assessment. *Genome Research*, 8(3), 175-185.
84. Diaz-Papkovich, A., Anderson-Trocmé, L., Ben-Eghan, C. & Gravel, S. UMAP reveals cryptic population structure and phenotype heterogeneity in large genomic cohorts. *PLoS Genetics* 15, (2019).
85. McInnes, L., Healy, J., Saul, N., & Großberger, L. (2018). UMAP: Uniform Manifold Approximation and Projection for Dimension Reduction. arXiv preprint arXiv:1802.03426.
86. Stuart, T., Butler, A., Hoffman, P., Hafemeister, C., Papalexi, E., Mauck, W. M., ... & Satija, R. (2019). Comprehensive integration of single-cell data. *Cell*, 177(7), 1888-1902.e21.
87. McInnes, L, Healy, J, UMAP: Uniform Manifold Approximation and Projection for Dimension Reduction, ArXiv e-prints 1802.03426, 2018.
88. Hafemeister, C., Stephenson, W., Houck-Loomis, B., Chattopadhyay, P. K., Swerdlow, H., ... & Satija, R. (2017). Simultaneous epitope and transcriptome measurement in single cells. *Nature Methods*, 14(9), 865-868.
89. Peterson, V. M., Zhang, K. X., Kumar, N., Wong, J., Li L., Wilson, D. C., ... & Pe'er, D. (2017). Multiplexed quantification of proteins and transcripts in single cells. *Nature Biotechnology*, 35(10), 936-939.
90. Abbas, A. T., El-Kafrawy, S. A., Sohrab, S. S. & Azhar, E. I. A. IgY antibodies for the immunoprophylaxis and therapy of respiratory infections. *Human Vaccines and Immunotherapeutics* 15, 264–275 (2019).
91. Hulet, M. D. & Hogarth, P. M. Molecular Basis of Fc Receptor Function. *Advances in Immunology* 57, 1–56 (1994)

92. Chiffelle, J. et al. T-cell repertoire analysis and metrics of diversity and clonality. *Current Opinion in Biotechnology* 65, 284–295 (2020).
93. Genolet, R. et al. TCR sequencing and cloning methods for repertoire analysis and isolation of tumor-reactive TCRs. *Cell Reports Methods* 3, (2023).
94. Robins, H. S. et al. Comprehensive assessment of T-cell receptor beta-chain diversity in alphabeta T cells. *Blood* 114, 4099–4107 (2009).
95. *Chromium Next GEM Single Cell V(D)J Reagent Kits v1.1 with Feature Barcode technology for Cell Surface Protein*, Document Number CG000208 Rev G, 10X Genomics, (July 12, 2022).
96. Hao, Y. et al. Integrated analysis of multimodal single-cell data. *Cell* 184, 3573–3587.e29 (2021).
97. Adossa, N., Khan, S., Rytönen, K. T. & Elo, L. L. Computational strategies for single-cell multi-omics integration. *Computational and Structural Biotechnology Journal* 19, 2588–2596 (2021).
98. Aran, D. et al. Reference-based analysis of lung single-cell sequencing reveals a transitional profibrotic macrophage. *Nature Immunology* 20, 163–172 (2019).
99. Böyum, A. Isolation of mononuclear cells and granulocytes from human blood. Isolation of mononuclear cells by one centrifugation, and of granulocytes by combining centrifugation and sedimentation at 1 g. *Scandinavian Journal of Clinical and Laboratory Investigation, Supplement 97*, 77–89 (1968).
100. *TotalSeqTM-C Human Universal Cocktail, V1.0*. Catalog Number 399905 Rev 3, BioLegend, (January 19, 2022).
101. *bcl2fastq2 Conversion Software v2.20 Software Guide*. Document Number 15051736 Rev 3, Illumina (February, 2019).
102. Zheng, Grace X.Y., Terry, Jessica M., [...] Bielas, Jason H. (2017). Massively parallel digital transcriptional profiling of single cells. *Nature Communications*. 8: 1–12, doi:10.1038/ncomms14049.
103. Xin, H. et al. GMM-Demux: sample demultiplexing, multiplet detection, experiment planning, and novel cell-type verification in single cell sequencing. *Genome Biology* 21, (2020).
104. *CITE-seq & Cell Hashing protocol*. New York Genome Center Technology Innovation Lab. Version 2018-02-12.
105. Mulè, M. P., Martins, A. J. & Tsang, J. S. Normalizing and denoising protein expression data from droplet-based single cell profiling. *Nature Communications* 13, (2022).
106. Borcherding, N., Bormann, N. L. & Kraus, G. scRepertoire: An R-based toolkit for single-cell immune receptor analysis. *F1000Research* 9, (2020).
107. Blair, A. P. et al. Cell Layers: Uncovering clustering structure in unsupervised single-cell transcriptomic analysis. *Bioinformatics Advances* 2, (2022).
108. Aran, D. et al. Reference-based analysis of lung single-cell sequencing reveals a transitional profibrotic macrophage. *Nature Immunology* 20, 163–172 (2019).

109. McCarthy, D. J., Campbell, K. R., Lun, A. T. L. & Wills, Q. F. Scater: Pre-processing, quality control, normalization and visualization of single-cell RNA-seq data in R. *Bioinformatics* 33, 1179–1186 (2017).
110. Monaco, G. et al. RNA-Seq Signatures Normalized by mRNA Abundance Allow Absolute Deconvolution of Human Immune Cell Types. *Cell Reports* 26, 1627-1640.e7 (2019).
111. Aran, D. et al. Reference-based analysis of lung single-cell sequencing reveals a transitional profibrotic macrophage. *Nature Immunology* 20, 163–172 (2019).
112. Amezquita, R. A. et al. Orchestrating single-cell analysis with Bioconductor. *Nature Methods* 17, 137–145 (2020).
113. Kim, T. K. T test as a parametric statistic. *Korean Journal of Anesthesiology* 68, 540–546 (2015).
114. Sawyer, A. J., Garand, M., Chaussabel, D. & Feng, C. G. Transcriptomic Profiling Identifies Neutrophil-Specific Upregulation of Cystatin F as a Marker of Acute Inflammation in Humans. *Frontiers in Immunology* 12, (2021).
115. Zhang, W. et al. Integrin $\alpha 6$ -Targeted Molecular Imaging of Central Nervous System Leukemia in Mice. *Frontiers in Bioengineering and Biotechnology* 10, (2022).
116. Raudvere, U. et al. G:Profiler: A web server for functional enrichment analysis and conversions of gene lists (2019 update). *Nucleic Acids Research* 47, W191–W198 (2019).
117. Zheng, W. et al. Inhibition of Cathepsin D (CTSD) enhances radiosensitivity of glioblastoma cells by attenuating autophagy. *Molecular Carcinogenesis* 59, 651–660 (2020).
118. Paloneva, J. et al. Mutations in two genes encoding different subunits of a receptor signaling complex result in an identical disease phenotype. *American Journal of Human Genetics* 71, 656–662 (2002).
119. Wen, T. et al. NKG7 Is a T-cell-Intrinsic Therapeutic Target for Improving Antitumor Cytotoxicity and Cancer Immunotherapy. *Cancer Immunology Research* 10, 162–181 (2022).
120. Wills, E. S. et al. Fecal microbial composition of ulcerative colitis and Crohn’s disease patients in remission and subsequent exacerbation. *PLoS ONE* 9, (2014).
121. Rahman, Z., Hussain, A., Shah, H. & Arshad, M. Urdu News Clustering Using K-Mean Algorithm On The Basis Of Jaccard Coefficient And Dice Coefficient Similarity. *Advances in Distributed Computing and Artificial Intelligence Journal* 10, 381–399 (2021).
122. Tang, J., Liu, J., Zhang, M. & Mei, Q. Visualizing large-scale and high-dimensional data. in 25th International World Wide Web Conference, WWW 2016 287–297 (International World Wide Web Conferences Steering Committee, 2016). doi:10.1145/2872427.2883041.
123. Harrington, L. E. et al. Interleukin 17-producing CD4⁺ effector T cells develop via a lineage distinct from the T helper type 1 and 2 lineages. *Nature Immunology* 6, 1123–1132 (2005).
124. Stockinger, B., Veldhoen, M. & Martin, B. Th17 T cells: Linking innate and adaptive immunity. *Seminars in Immunology* 19, 353–361 (2007).

125. Neurath, M. F. et al. The transcription factor T-bet regulates mucosal T cell activation in experimental colitis and Crohn's disease. *Journal of Experimental Medicine* 195, 1129–1143 (2002).
126. Hirota, K. et al. Preferential recruitment of CCR6-expressing Th17 cells to inflamed joints via CCL20 in rheumatoid arthritis and its animal model. *Journal of Experimental Medicine* 204, 2803–2812 (2007).
127. Yang, P. et al. Th17 cell pathogenicity and plasticity in rheumatoid arthritis. *Journal of Leukocyte Biology* 106, 1233–1240 (2019).
128. Lee, Y. K., Menezes, J. S., Umesaki, Y. & Mazmanian, S. K. Proinflammatory T-cell responses to gut microbiota promote experimental autoimmune encephalomyelitis. *Proceedings of the National Academy of Sciences of the United States of America* 108, 4615–4622 (2011).
129. Li, B. et al. The role of Th17 cells in psoriasis. *Immunologic Research* 68, 296–309 (2020).
130. Murugaiyan, G. et al. IL-27 Is a Key Regulator of IL-10 and IL-17 Production by Human CD4+ T Cells. *The Journal of Immunology* 183, 2435–2443 (2009).
131. Komatsu, N. et al. Pathogenic conversion of Foxp3 + T cells into TH17 cells in autoimmune arthritis. *Nature Medicine* 20, 62–68 (2014).
132. Yan, Q. et al. Structural Basis for Activation of ZAP-70 by Phosphorylation of the SH2-Kinase Linker. *Molecular and Cellular Biology* 33, 2188–2201 (2013).
133. Pastore, G. et al. Optimized Protocol for the Detection of Multifunctional Epitope-Specific CD4+ T Cells Combining MHC-II Tetramer and Intracellular Cytokine Staining Technologies. *Frontiers in Immunology* 10, (2019).

MSc. MPH Lauren De Vore

Doctoral Candidate AöR Experimental Cardiology

University Hospital of Cologne (AöR)
Department III of Internal Medicine/Experimental Cardiology
LFI, Floor 4, Room 105, Kerpener Str. 62
D-50937 Cologne, Germany

[REDACTED]@univ-koeln.de



LinkedIn: <https://www.linkedin.com/in/lauren-de-vore/>

ORCID: 0000-0002-5958-0519

UNIVERSITY EDUCATION

- Aug 2016 – European Joint Masters Degree Erasmus Mundus
- July 2017 – Master of Public Health – University of Sheffield, United Kingdom
- July 2018 – Master of Science in Advanced Biostatistics & Epidemiology – EHESP, France
- Aug 2013 – Studies of Biochemistry & Molecular Cell Biology –
- June 2016 – University of Linfield, McMinnville Oregon, USA
- Sep 2009 – Skyview Highschool, Vancouver Washington, USA
- June 2013 – Advanced Program in Science, Technology, Engineering, and Mathematics

POSITIONS

- Sep 2018 – Clinical Applications Development Manager – Sysmex Europe
- March 2020 – Hematology Research & Development in Hamburg, Germany
- Feb 2018 – Visiting research internship at the Conservatory of Engineering & Technologies
- July 2018 – (Conservatoire national des arts et métiers) Cnam Paris, France
- Aug 2017 – MSc. student at the French School of Public Health (EHESP) in collaboration
- July 2018 – with the Pasteur Institute & The University of Sheffield, United Kingdom
Topic: ‘Modeling The Transmission of Hepatitis C Virus in an Egyptian Hospital: A Network Based approach with Egocentric Data’
Supervisors: Profs. Laura TEMIME, Cnam; Jean-Baptiste COMBE, EHESP
- Aug 2016 – MPH student at University of Sheffield, School of Health & Related Research
- July 2017 – Sheffield, United Kingdom
- Aug 2013 – BSc. student with minor in mathematics at University of Linfield
- Jun 2016 – Topic: ‘The Effect of Rapamycin on Mitochondrial Electron Transport Chain Activity and Superoxide Production’
Supervisor: Prof. Dr. Megan Bestwick Smith
- Aug 2012 – Engineering Student internship – The Boeing Company, Portland Oregon, USA
- July 2014 – Supervisor: Darwin Utter

AWARDS

July 2018 Award for Best Poster at EHESP Conference
June 2017 Erasmus Mundus+ Travel Grant
Oct 2016 Erasmus Mundus Study Support
Feb 2015 Mathematics Competition Award COMAP MCM
April 2013 University of Linfield Subject Exam Award: \$20,000
Aug 2013 University of Linfield Scholarship: \$54,000
April 2012 AAUW Woman in Engineering Award

OTHER SCIENTIFIC ACTIVITIES AND HONORS

Jan 2019 Sysmex Internal: Osaka Japan. Medical Device Patented Solution
Sept 2018 – Study Coordinator & Consultant for Research and Development in Hematology
March 2020 Project Focuses: Flow Cytometry Gating Algorithms for Detection of Malaria, Sepsis, and Hematological Malignancies [Sponsored by Sysmex].

LANGUAGES

English: Native
Spanish: Advanced; 8 Years + Study Exchange at University of Granada, Spain
French: Advanced; 2 years + Study Exchange in Rennes & Paris, France
German: Intermediate; Placement Test B1

RELATED PUBLICATIONS

Nettersheim, Felix S.*; **De Vore, Lauren***; Winkels, Holger. 2020. "Vaccination in Atherosclerosis" *Cells* 9, no. 12: 2560.

Dennis Mehrkens*, Felix Sebastian Nettersheim*, Felix Ballmann, **Lauren De Vore**,....., Stephan Baldus, Martin Mollenhauer⁺, Holger Winkels⁺. Nov. 2022 "Inhibition of myeloperoxidase prevents thoracic aortic aneurysm formation in Marfan mice" Preprint. DOI: 10.1101/2022.11.24.517172

Deklaration

Ich versichere, dass ich die von mir vorgelegte Dissertation selbstständig angefertigt, die benutzten Quellen und Hilfsmittel vollständig angegeben und die Stellen der Arbeit – einschließlich Tabellen, Karten und Abbildungen –, die anderen –, die anderen Werken im Wortlaut oder dem Sinn nach entnommen sind, in jedem Einzelfall als Entlehnung kenntlich gemacht habe; dass diese Dissertation noch keiner anderen Fakultät oder Universität zur Prüfung vorgelegen hat; dass sie – abgesehen von unten angegebenen Teilpublikationen – noch nicht veröffentlicht worden ist sowie, dass ich eine solche Veröffentlichung vor Abschluss des Promotionsverfahrens nicht vornehmen werde. Die Bestimmungen dieser Promotionsordnung sind mir bekannt. Die von mir vorgelegte Dissertation ist von Prof. Dr. Holger Winkels betreut worden.

Ich versichere, dass ich alle Angaben wahrheitsgemäß nach bestem Wissen und Gewissen gemacht habe und verpflichte mich, jedmögliche, die obigen Angaben betreffenden Veränderungen, dem Promotionsausschuss unverzüglich mitzuteilen.

03.02.2026

Lauren De Vore